Title
Electrochemical Modeling of a Lithium-Metal Anode

Author
Ferrese, Anthony John

Publication Date
2013

Peer reviewed|Thesis/dissertation

Electrochemical Modeling of a Lithium-Metal Anode

By

Anthony John Ferrese

A dissertation submitted in partial satisfaction of the

requirements for the degree of

Doctor of Philosophy

in

Chemical Engineering

in the

Graduate Division

of the

University of California, Berkeley

Committee in charge:

Professor John Newman, Chair
Professor Nitash Balsara
Professor Jeffrey Long

Fall 2013

Electrochemical Modeling of a Lithium-Metal Anode

Abstract

Electrochemical Modeling of a Lithium-Metal Anode

by

Anthony John Ferrese

Doctor of Philosophy in Chemical Engineering

University of California, Berkeley

Professor John Newman, Chair

The use of a lithium-metal anode in both current and future battery technologies, including lithium-sulfur and lithium-air batteries, is of great interest due to its high energy density and specific energy. Significant effort has been devoted to understanding the cathode in these technologies and toward mitigating dendrite formation, the largest failure mechanism for lithium-metal batteries. This research addresses the problems that could occur even if dendrite propagation is controlled, namely large-scale movement of the lithium at the lithium-metal anode, resulting in a shape change of the lithium/separator interface.

In the first part of Chapter 1, a two-dimensional electrochemical model is created which forms the basis for the latter half of Chapter 1, Chapter 2, and Chapter 3. In Chapter 1, modeling was done using COMSOL Multiphysics, which uses a finite-element approach. This model incorporates electrode tabbing where, during discharge, the current is drawn from the top of the positive tab and inserted into the bottom of the negative tab. Also modeled is a moving boundary at the negative electrode, a CoO_2 intercalation electrode as the cathode, and a lithium-metal negative electrode. The positive electrode is modeled using porous electrode theory, the separator as a liquid electrolyte with a binary salt, and the total volume changes are assumed to be zero. Finally, the negative electrode in this model is stoichiometrically twice the thickness required, to avoid the need for a separate negative current collector.

In the second part of Chapter 1, the model was cycled at various rates, and shows that, even without dendrites, there is significant large-scale movement of lithium both during each half cycle and after a full cycle of a discharge followed by a charge. Specifically, more lithium is depleted near the negative tab while discharging the cell, yet after a full cycle of a discharge

followed by a charge, there is a net migration of lithium towards the negative tab. The model shows that this migration is caused by three separate phenomena. First, the geometry strongly affects the current density distribution, which directly correlates to the asymmetric depletion of lithium during the discharge phase. The second driving force is the open-circuit-potential function, the slope of which not only affects the magnitude of the movement, but also is the largest nonlinearity that contributes to the movement of lithium after a full cycle. The third, and smallest, contributor to the movement of lithium is the concentration gradient in the liquid electrolyte. When the OCP is flat and the concentration gradients are reduced by increasing the diffusivity, the lithium will return to its starting position after a full cycle.

Chapter 2 builds on the work developed in Chapter 1 through modeling the movement over extended cycling. The model was cycled at various rates, depths of discharge, and lengths of the rest over multiple cycles. From this, we saw that, with a large excess of lithium at the negative electrode, the movement of the lithium reaches a quasi-steady state where the movement during each subsequent cycle remains at the same magnitude. The rate at which the movement of the lithium reaches that steady state depends on the slope of the open-circuit-potential function, the rate of discharge and charge, the depth of discharge, and the length of time that the cell is allowed to rest both after the discharge and charge phase.

First, the slope of the open-circuit-potential function strongly affects both the magnitude of the movement of lithium seen during cycling and the rate at which a steady state is reached. A more steeply sloped open-circuit-potential function causes less movement of lithium during cycling, and a steady state is reached more quickly than with a flatter open-circuit-potential function.

Next, the assumption that there is a large excess of lithium in the negative electrode is relaxed, and the utilization of the negative electrode is increased to 80 percent. This is achieved by reducing the thickness of the negative electrode from 50 to 15 µm with the result that pinching of the negative electrode is seen and is another nonlinearity that leads to a progression of the movement of lithium over multiple cycles.

With a 50 µm thick negative electrode, the effect of the discharge and charge rate is discussed. Here we see that increasing the C-rate both increases the magnitude of the movement of lithium during cycling and delays the quasi-steady state seen previously. We then explore the effect that the depth of discharge has on the movement of lithium during cycling, and the effects of the rest periods. Finally, we compare the magnitude of the effect of the C-rate with that of the rest periods and find that the lithium is more uniform if the cell was charged quickly and allowed to rest for longer and is less uniform if the cell is charged slowly with a limited rest period following charging.

Chapter 3 builds on the model developed in Chapter 1 by relaxing the assumption that the separator, while inhibiting dendrites, also allowed the lithium to move unhindered. Therefore, in this chapter, a dendrite-inhibiting polymer separator which has a shear modulus

twice that of lithium is included in the model. Such a separator resists the movement of lithium seen in Chapters 1 and 2 though the generation of stresses in the cell. As can be imagined, as the lithium moves, the separator is either compressed or stretched. This translates into stresses in the separator and lithium that affect the negative electrode through two mechanisms: altering the thermodynamics of the negative electrode and deforming the negative electrode mechanically. Both of these mechanisms are treated in this chapter.

First, the effect of the stress on the thermodynamics is developed. From this, we see that it takes very high pressures to modify the kinetics enough to have an appreciable effect on the movement of lithium. Under these pressures, the assumption that the lithium is rigid is invalid, thus the elastic deformation of lithium is included. This relaxes the stresses in the negative electrode through the elastic compression of the lithium; however, the stresses in the negative electrode are still significantly larger than the yield strength of lithium, meaning that plastic deformation of the negative electrode must be included.

With the inclusion of elastic and plastic deformation of the negative electrode the model shows that a dendrite-inhibiting polymer separator significantly resists the lithium movement seen in Chapters 1 and 2. In addition, we find that the plastic deformation plays a much larger role in the flattening of the lithium than either the pressure-modified reaction kinetics or elastic deformation. Furthermore, the flattening of the negative electrode causes only very slight differences in the local state of charge in the positive electrode. Thus, we can safely say that including a dendrite-inhibiting separator benefits a lithium-metal battery through forcing the negative electrode to be more uniform without causing negative effects in the positive electrode such as larger swings in the local state of charge.

In Chapter 4, a second method to inhibit dendrite growth is explored through the use of a ceramic that is conductive to lithium ions. While ceramics tend to be very stiff, they are also very brittle and exhibit little or no plastic deformation and fail catastrophically when their yield point is reached. This lack of plastic deformation combined with their high elastic moduli, means that ceramics can operate safely in a very narrow window of strains making them especially susceptible to fracture due to small deformations. Therefore, the stress profile due to bending of a ceramic layer is calculated for two different bending programs and two different geometries.

First, as a base case, the stress profile for a block ceramic is calculated for constant radius bending. This stress profile is then compared to a constant radius bending of a laminated polymer-ceramic layer. It is found that the stress reduction due to the addition of a polymer layer only reduces the maximum stress in the ceramic layer by 9 percent. Because of this, a second, periodic geometry, with a polymer section followed by a ceramic section, is introduced. Due to the unique nature of constant radius bending, the stress profile in this periodic geometry is the same as if it were a solid ceramic. Therefore, a new bending program of a cantilevered beam with a point force at the end is used to compare the periodic geometry to a

block ceramic. The resulting reduction in stress due to the addition of the polymer section is found to be significant, between about 50 and 99 percent depending on the ratio of Young's moduli.

Electrochemical Modeling of a Lithium-Metal Anode

Table of Contents

Chapter 1

Modeling Lithium Movement in a Lithium-Metal Battery

1.1 Introduction

Electrochemical batteries have been used as convenient and relatively safe portable energy-storage devices for many years; and, with the development of rechargeable-battery technology, batteries have become an everyday dependence. With the progression of technology, the demand on rechargeable portable energy has increased to a point where, in certain applications, energy density is the limiting factor. More recently, the push toward widespread use of rechargeable batteries for powering vehicles along with other high-energy-demand applications has gained in popularity. Thus, there has been a large increase in the need for improved energy density in rechargeable batteries.[1] For example, while nickel-metal hydride batteries are an acceptable solution for hybrid-electric vehicles (HEVs), the move toward fully electric vehicles such as plug-in hybrids (PHEVs) and eventually electric vehicles (EVs) will require higher-energy-density batteries. Several new battery technologies have been proposed; however, a long-time favorite has been lithium-metal batteries due to their high theoretical energy density.[1-3] By replacing the standard graphite electrode with a solid lithium electrode, the size and weight of the battery are significantly reduced.[1]

Although the benefits of lithium-metal batteries are clear, there are several failure mechanisms that occur during cycling of the batteries. The most critical of these mechanisms and the most researched is the control of the electrode/electrolyte interface, primarily dendrite growth at the lithium surface during charging, which has been shown to cause shorting.[4-6] The regime of stability in which dendrite propagation is repressed, found through modeling dendrite growth, is shown to occur when the shear modulus of the separator is greater than that of lithium metal (for more detail on this subject, please refer to Chapter 3).[5] There are currently two main methodologies that are being researched to inhibit dendrite growth. The first, is to create a polymer separator with acceptable ionic conductivity that has a shear modulus greater than that of lithium (Chapter 3),[1, 7-9] and the second is to protect the anode with a ceramic that is conductive to lithium ions (Chapter 4).[10, 11] However, even if dendrites can be prevented, it is likely that gradual redistribution will occur due to a rearrangement of the lithium over large length scales, on the order of centimeters. For example, an increase in the

thickness of the lithium metal near the negative tab is predicted in the model described in this chapter.

This chapter, and the rest of this thesis for that matter, operates under the assumption that dendrite formation can be prevented through the use of a polymer separator or ceramic protective layer and looks instead into the possibility that anodic lithium redistribution could occur. Due to the difficulty in cycling lithium-metal batteries and the extensive focus on solving the dendrite problem, very little has been published on large-scale redistribution in batteries. Redistribution due to the mechanisms described in this paper has not been studied before. However, redistribution due to significantly different mechanisms has been observed in other chemistries, such as zinc secondary electrodes.[12, 13]

In this chapter, we develop the equations necessary for modeling a lithium-metal battery in two dimensions and determining the movement of lithium along the negative electrode/separator interface (Section 1.2). Then, in Section 1.3, we discuss the movement of lithium seen during the first cycle and the main drivers for this phenomenon. In Subsection 1.3a, we discuss how the geometry of the cell plays an important role in determining the distribution of charge throughout the cell. Then, in Subsection 1.3b, we learn how the open-circuit-potential function, specifically the slope of this function, is the largest non linearity contributing to the movement of lithium seen along the negative electrode/separator interface. Finally, in Subsection 1.3c, the role that the concentration gradients in the electrolyte have on the movement of lithium is discussed.

The equations and the model developed in this chapter form the basis for which the modeling in the subsequent chapters is built. In this chapter, only one cycle of the cell is looked at. In Chapter 2, we look at the lithium movement over multiple cycles and determine the driving forces leading to the further movement of lithium seen after the first cycle. We also treat how driving forces, such as the slope of the open-circuit-potential function, the depth of discharge to which the cell is cycled, the rate at which the cell is cycled, and the length of the rest periods after the discharge and charge phases work together to cause the movement of lithium to reach a steady state.

Chapter 3 further builds upon the model developed in this chapter by including a rigid, dendrite-inhibiting polymer separator into the model, thereby resisting the movement seen in this chapter and in Chapter 2 and causing stresses to build up in the negative electrode. In Chapter 3, we develop an understanding of continuum mechanics including both elastic and plastic deformation and build a model whereby both of these effects are included in the lithium-metal negative electrode. As shall be seen, the build-up of stresses in the negative electrode, as caused by the resistance of the separator to the movement of the underlying lithium, causes mechanical deformation of the lithium, leading to a more uniform negative electrode.

Finally, in Chapter 4, we look into the use of ceramics used to stabilize a lithium-metal negative electrode. In this chapter, we calculate the stresses in the ceramic from bending due to either surface roughness of the lithium, the growth of a dendrite, or bending of the cell for packaging purposes. Throughout Chapter 4, we look at the stress profiles for three different ceramics, each with a different elastic modulus. We then determine the reduction in stress due to changing the geometry of the ceramic in two different ways: ceramics laminated with elastic polymers, and a repeating geometry of a ceramic segment followed by a polymer segment.

1.2 Methods

In order to capture the behavior of interest, electrode tabbing is included (Figure 1.1) where, during discharge, the current is drawn from the top of the positive tab and inserted into the bottom of the negative tab. A moving boundary is also included along with an intercalation electrode as the cathode. Here, the *y* dimension of the model is through the thickness of the cell sandwich, which can be seen to be 200 µm thick, and the *x* dimension is taken to be along the length of the unwound cell sandwich and is 50 cm long. Tabs leading to the external leads of the cell are found at opposite corners of the cell. The positive current collector is aluminum, and the positive and negative tabs are copper. The positive electrode is modeled as a typical CoO_2 porous intercalation electrode found in the literature.[14-19] Here (Figure 1.1), the positive electrode active material particles have been drawn out of proportion to aid in the visualization of the model geometry. The separator is modeled as a liquid electrolyte, and the negative electrode as lithium metal. The negative electrode in this model is twice the thickness necessary in order to make unnecessary a separate negative current collector. All graphs presented later, unless specifically noted, are along the interface between the separator and the negative electrode (the line with points h_1 and h_2 lying on it in Figure 1.1) with the origin occurring at the left side of the cell, at the negative tab. This constitutes a through-plane cross-section of, what could be considered, a typical 18650 cell construction.

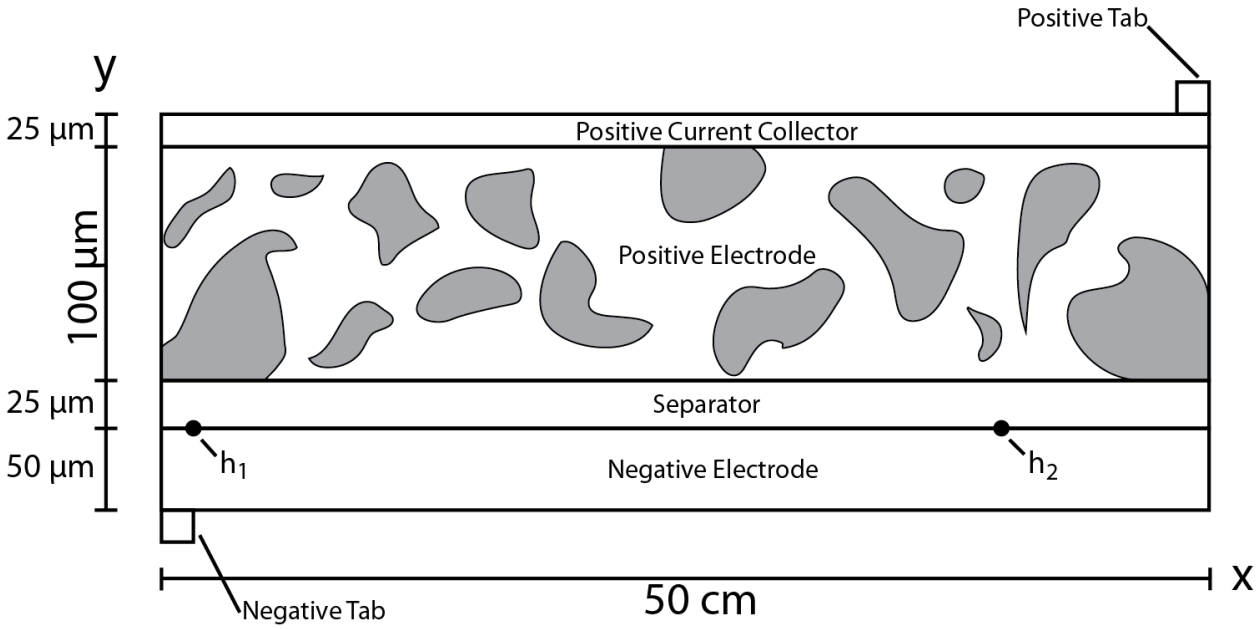

Figure 1.1. Two-dimensional model geometry of a lithium-metal battery, consisting of a lithium-metal negative current collector, a lithium-metal negative electrode, a liquid-electrolyte separator, composite cathode, and aluminum positive current collector.

In this work, modeling was done using COMSOL Multiphysics, which uses a finite-element approach. The model geometry, shown in Figure 1.1, attempts to recreate a standard battery configuration. The negative electrode is modeled as a lithium-metal layer with a varying, finite thickness, and the positive electrode consists of porous $LiCoO_2$. Film formation at the lithium/separator interface and volume changes of the positive electrode and of the overall cell were not considered. The separator is a liquid electrolyte which is assumed to fill any gaps when the lithium shrinks during discharge and moves into excess head space as the thickness of the lithium anode thickens during charge. In other words, the separator is able to expand and contract freely with the movement of the negative electrode, thereby keeping the total volume of the cell sandwich constant. The liquid electrolyte allows for the free movement of the lithium negative electrode and results in the worst-case scenario of lithium migration during cycling. If, for example, a polymer separator that has mechanical properties such that dendrite propagation is mitigated (as seen in the work by Monroe and Newman[5]) were used in place of the liquid electrolyte (as will be done in Chapter 3), the results of the shape change will be altered significantly. In fact, as can be seen in Chapter 3, the dendrite-inhibiting polymer separator significantly represses the movement of the lithium by providing a force opposite to the migration.

The cell was modeled as a two-dimensional coupled to a pseudo three-dimensional model. The two-dimensional model has the *x* and *y* dimensions, labeled in Figure 1.1, constituting the length along the unwound cell and the thickness through the cell sandwich,

respectively. The pseudo three-dimensional model (not shown), takes the *x* and *y* dimensions from the positive electrode of the two-dimensional model. The pseudo third dimension is the *r*-dimension and constitutes the radial position in the active-material particles in the positive electrode. Transport in the separator is modeled with concentrated solution theory with the assumption that it is a binary electrolyte. Thus, the transference number of the lithium ion, the electrical conductivity, and the diffusion coefficient of the lithium salt characterize transport in the separator and are held as constants.

All equations were based on the papers by Doyle et al. and Fuller et al.[14-18] and Newman and Thomas-Alyea.[19] Modification includes expanding the equations for use in a two-dimensional model and adding in a moving boundary at the interface between the negative electrode and the separator that moves stoichiometrically with the amount of current passed. The moving boundary is incorporated using a deformed mesh, and the movement is calculated by using Faraday's law and the density of lithium to convert the local current density into the velocity of the moving boundary.

1.2a Governing Equations

Beginning with the liquid-electrolyte separator, a material balance on the salt is given by,

$$\frac{\partial c_2}{\partial t} = \nabla \cdot (D_2 \nabla c_2). \qquad 1.1$$

Here we assume that the solvent concentration is not a function of the electrolyte concentration[15] and that the transference number is constant.[17] The potential in the liquid phase is governed by an extended Ohm's law,[14]

$$\boldsymbol{i}_2 = -\kappa_2 \nabla \phi_2 + \frac{2\kappa_2 \mathrm{RT}}{\mathrm{F}} (1 - t_+) \left(1 + \frac{\partial \ln f_{\pm}}{\partial \ln c_2}\right) \nabla \ln c_2 \,, \qquad 1.2$$

where we assume that the conductivity and transference number are constant. Currently the activity coefficient $f_{\pm}$ is assumed to be constant, but, if data are available, the variation can be included here.

It should be noted here that the convection terms, although perhaps relevant due to the moving boundary and liquid electrolyte, have been left out of the previous equations. This is due to the small effect that the concentration gradients have on the movement of the lithium and for the sake of simplicity. For a more detailed explanation please refer to Subsection 1.3c.

At the interface between the separator and the lithium anode, a charge-transfer reaction occurs following Butler-Volmer kinetics.[15] Since the separator is assumed to be a liquid electrolyte, the reaction takes the form

$$\mathrm{Li} \leftrightarrow \mathrm{Li}^{+} + \mathrm{e}^{-} \tag{1.3}$$

and the general form of the kinetic expression is taken to be

$$i_{loc} = i_0 \left\{ \exp\left[\frac{\alpha_a \mathrm{F}}{\mathrm{RT}} \eta_s\right] - \exp\left[\frac{-\alpha_c \mathrm{F}}{\mathrm{RT}} \eta_s\right] \right\}, \tag{1.4}$$

where η_s is the local value of the surface overpotential:

$$\eta_s = \phi_1 - \phi_2 - \mathrm{U}_1. \tag{1.5}$$

Here U_1 is the theoretical open-circuit potential, and i_0 is the exchange current density, which is taken from Albertus et al.,[20] where it is assumed to be

$$i_0 = K c_2^{0.5}. \tag{1.6}$$

Here K is the reaction rate constant and c_2 is the local concentration of salt in the separator. The boundary conditions for these equations include the flux of lithium ions at the lithium/separator interface equaling the net transfer of current at that interface. The flux and concentration of each species as well as the potential in solution are taken to be continuous between the separator and the positive electrode.

The positive electrode consists of an inert conducting material, the liquid electrolyte phase, and the solid active-material insertion particles. These phases are treated as superimposed continua, and the material balance in the liquid phase is

$$\varepsilon_2 \frac{\partial c_2}{\partial t} = \nabla \cdot (\varepsilon_2 D_2 \nabla c_2) + a \frac{i_{loc}(1 - t_+)}{\mathrm{F}}, \tag{1.7}$$

where ε_2 is the volume fraction of the electrolyte in the positive electrode and a is the specific surface area or surface area of the active material per volume of the cathode. The pore-wall flux (j_n) is related to local current density and to the divergence of the current in the electrolyte phase through

$$a j_n = \frac{a i_{\mathrm{loc}}}{\mathrm{F}} = \frac{\nabla \cdot \boldsymbol{i}_2}{\mathrm{F}}. \tag{1.8}$$

The current flowing in the electrolyte is governed by Equation 1.2 with the addition that there is a pore wall flux in this domain as described by Equation 1.8. Here the conductivity and diffusivity are effective values through the Bruggeman Equation[21]

$$\kappa_{\mathrm{eff}} = \kappa \varepsilon^{1.5} \text{ and } D_{\mathrm{eff}} = D \varepsilon^{0.5}. \tag{1.9}$$

Although the diffusivity, conductivity, and transference number are known functions of concentration, they are currently held as constants. The boundary condition in the solution

phase of the positive electrode is such that the fluxes of the species are zero at the positive current collector/positive electrode boundary.

Due to the large surface area of the positive electrode, the kinetics fall in the linear regime; therefore the kinetic expression in the positive electrode is simplified to linear kinetics where

$$i_{\mathrm{loc}} = i_0 \mathrm{F} \frac{\eta_s}{\mathrm{RT}}. \tag{1.10}$$

Equation 1.5 defines the surface overpotential, η_s, where the open-circuit potential U_1 is a function of the surface concentration of lithium in the solid c_1, which is calculated in Equation 1.13. The reaction in the positive electrode is

$$LiCoO_2 \leftrightarrow Li_{1-x}CoO_2 + xLi^+ + xe^-, \tag{1.11}$$

where x varies between 0 and 0.5. The exchange current density is given by

$$i_0 = \mathrm{F}(k_a)^{\alpha_c}(k_c)^{\alpha_a}(c_{1\max} - c_1)^{\alpha_c}(c_1)^{\alpha_a}(c_2)^{\alpha_a}, \tag{1.12}$$

where $(c_{1\max} - c_1)$ is the concentration of unoccupied sites in the insertion material.

The active material in the cathode is assumed to be made up of spherical particles of a constant radius R_p with diffusion being in the r-direction only, and the transport of lithium in the solid phase is governed by

$$\frac{\partial c_1}{\partial t} = \frac{1}{r^2}\frac{\partial}{\partial r}\left(D_1 r^2 \frac{\partial c_1}{\partial r}\right), \tag{1.13}$$

where c_1 represents the concentration of lithium in the solid particle. A separate three-dimensional model is used to solve Equation 1.13, where the x and y dimensions are those taken from the positive electrode in the two-dimensional model and the third dimension is the r-dimension which is out of the solid active-material particles. The boundary condition at the surface of the particles ($r=R_p$) is

$$j_n = -D_1 \frac{\partial c_1}{\partial r}, \tag{1.14}$$

where the pore-wall flux is calculated in the cathode of the two-dimensional model. Equation 1.13 is then solved numerically in the three-dimensional active-material model, and the solution at the boundary $r=R_p$ is used in the two-dimensional model to solve for the exchange current density seen in Equation 1.12. Due to spherical symmetry, the second boundary condition for the three-dimensional model is

$$\frac{\partial c_1}{\partial r} = 0 \text{ at } r = 0. \tag{1.15}$$

The potential in the solid phase, which includes the current collectors as well as the negative and positive electrodes, is governed by Ohm's law

$$\boldsymbol{i}_1 = -\kappa_{\text{eff}} \nabla \phi_1, \tag{1.16}$$

and the current in the two phases is conserved through the equation:

$$\nabla \cdot (\boldsymbol{i}_1 + \boldsymbol{i}_2) = 0. \tag{1.17}$$

Thus the current flows through either the liquid electrolyte or the solid phase. The boundary conditions are such that the potential in the solid phase, ϕ_1, is arbitrarily set to zero along the bottom of the negative tab, and a uniform current in the solid phase, $\boldsymbol{i}_1$ is set along the top of the positive tab.

To restate, diffusion in the electrolyte is governed by Equation 1.1 for the separator and Equation 1.7 for the positive electrode. The potential in the liquid phase of the separator and the positive electrode is governed by Equation 1.2. The potential in the solid phase is governed by Ohm's law. The reaction kinetics in the positive electrode is linear and are Butler-Volmer (Equation 1.4) at the negative electrode/separator interface (Equation 1.10). Finally, Equation 1.13 governs the solid-phase diffusion of the lithium in the positive electrode.

The problem is now completely specified and is solved numerically at every time step and position.

1.3 Results and Discussion

Transport properties used in the model are listed below in Table 1.1. The total volume as well as the porosities of the cell are assumed to be constant throughout the cycling of the battery. This means that, during discharge, the separator is assumed to fill in the void left by the lithium removed, and, on charging, the separator shrinks, allowing for the growth of the lithium plate. Thus, as the negative electrode shrinks on discharge, the separator expands keeping the total volume of the cell constant. In other words, the distance between the current collectors remains constant.

Table 1.1. Transport properties used in this model. (a) signifies data is not available for these parameters. (b) signifies the value that is given as an initial condition.

System Specific			Adjustable		
Parameter	Value	Ref.	Parameter	Value	
D_1	5×10^{-13} m^2/s	25	T	298 K	
D_2	7.5×10^{-11} m^2/s	26	R_p	4 µm	
$\kappa_{\mathrm{cathode}}$	3.7 S/m	18	c_{10}	26,000 mol/m^3	(b)
κ_{soln}	1.3 S/m	26	c_{20}	2000 mol/m^3	(b)
κ_{CCa}	1.0776×10^{7} S/m	-	ε_2	0.3	
κ_{CCc}	3.546×10^{7} S/m	-			
α_1, α_2	0.5	(a)			
t_+	0.363	17			
K	6.1×10^{-6} mol$^{0.5}$/m$^{0.5}$-s	20			

The lithium-metal battery was cycled galvanostatically at four different rates beginning with a discharge, followed by a rest period of 1000 seconds, and completed by a charge at the same rate and duration as the discharge. A rest period of 1000 seconds was chosen because it was a convenient number larger than the time constant in the *x* direction for diffusion of the electrolyte through the cathode and separator. To be sure that the rest period is not affecting the simulation results, the model was also cycled with a rest period of 20,000 seconds after discharge with similar results (less than a 5% difference). All rate calculations are based on the positive electrode. The four charge rates are a 0.1-C rate, corresponding to a 10 hour discharge rate, a 0.2-C rate, corresponding to a 5 hour discharge rate, a 0.5-C rate, corresponding to a 2 hour discharge rate, and a 1-C rate. All cycles were run to a time corresponding with a 50 percent depth of discharge based on the positive electrode, meaning that the cell cycles between $Li_{0.5}CoO_2$ and $Li_{0.75}CoO_2$. The average lithium removed during discharge was 9.98 µm, which is approximately 1/5 the total amount of lithium available. The current needed for a given C rate was calculated from the theoretical current needed to achieve a 1 hour discharge rate at the positive electrode. The time of the discharge was calculated based on the theoretical time required to fill 50 percent of the available capacity in the positive electrode. The maximum concentration of lithium in the positive electrode (c_{1max}) was assumed to be one lithium atom per CoO_2 molecule with a starting concentration of 26,000 mol/m^3 or roughly 50 percent of the maximum concentration.

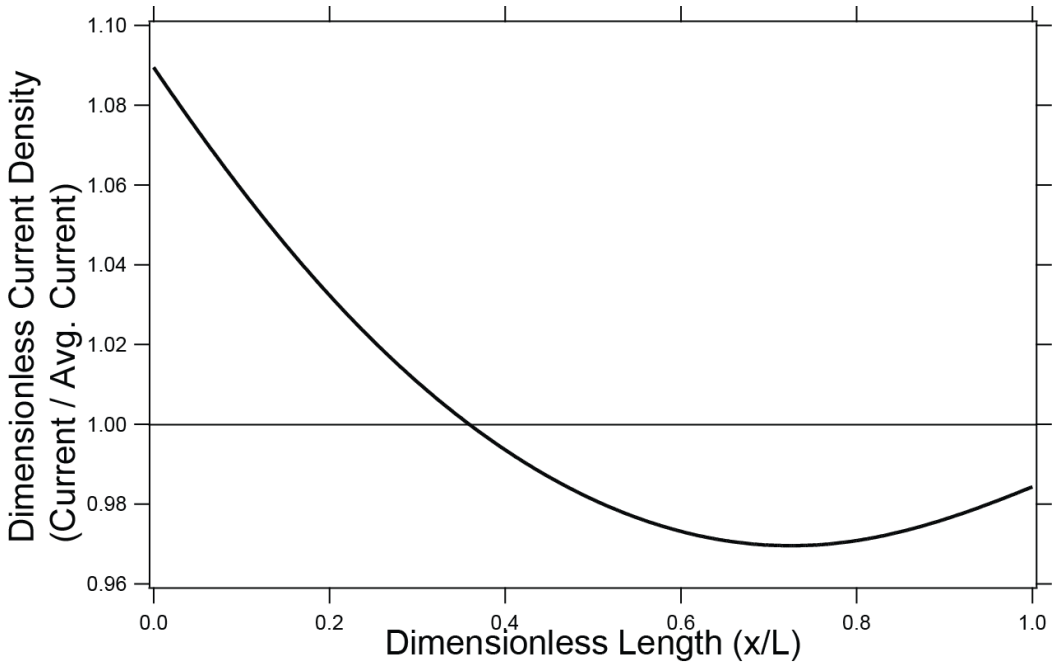

Figure 1.2. Dimensionless current density along the negative electrode/separator interface at the beginning of discharge at a C/5 rate.

Figure 1.2 shows the initial dimensionless current density for the 0.2-C rate along the negative electrode/separator interface. The dimensionless current density was calculated by dividing the local current density by the average current density. Here the asymmetric current distribution can be clearly seen with the minimum current occurring at about 0.74 in the *x* direction and achieving about 97 percent of the average current. The tendency for the current to pass through the left side of the battery is due to the fact that the resistance of the negative electrode is roughly four times higher than that of the positive current collector. Thus, the current would rather travel along the positive current collector, which is less resistive, leading to a left-biased current density.

1.3a Cell Geometry

In this model, the geometry of the cell strongly affects the current density and nonuniformity of the lithium negative electrode during cycling of the cell. The magnitude of the asymmetry of the current density seen in Figure 1.2 is a direct result of the large length-to-thickness ratio. For the purpose of this discussion, the physical dimensions of the cell and the conductivities were kept constant, and the effective length-to-thickness ratio was changed through the addition of tabs to the standard geometry of Figure 1.1. Each tab along the positive electrode passed the same current such that the total current remained the same throughout the addition of tabs. It should be noted that the same effect could be achieved by either

changing the physical dimensions of the cell geometry or by changing the conductivities of the positive current collector or negative electrode. For example, by changing the conductivity of the negative electrode (by adding a current collector) to have the same conductivity as that of the positive current collector, one can achieve similar results to that of the system with two tabs along both the top of the positive electrode and the bottom of the negative electrode. Similarly, by making the positive current collector more resistive than the negative, one can achieve the mirror image of the 1-tab line in Figure 1.3, meaning that cycling would remove the lithium more towards the right side of the cell where x/L=1.

For this section, the model was discharged once at a C/5 rate for 2.5 hours for each of the tab geometries described, and the results of the change in the height of the lithium relative to its starting location are plotted in Figure 1.3.

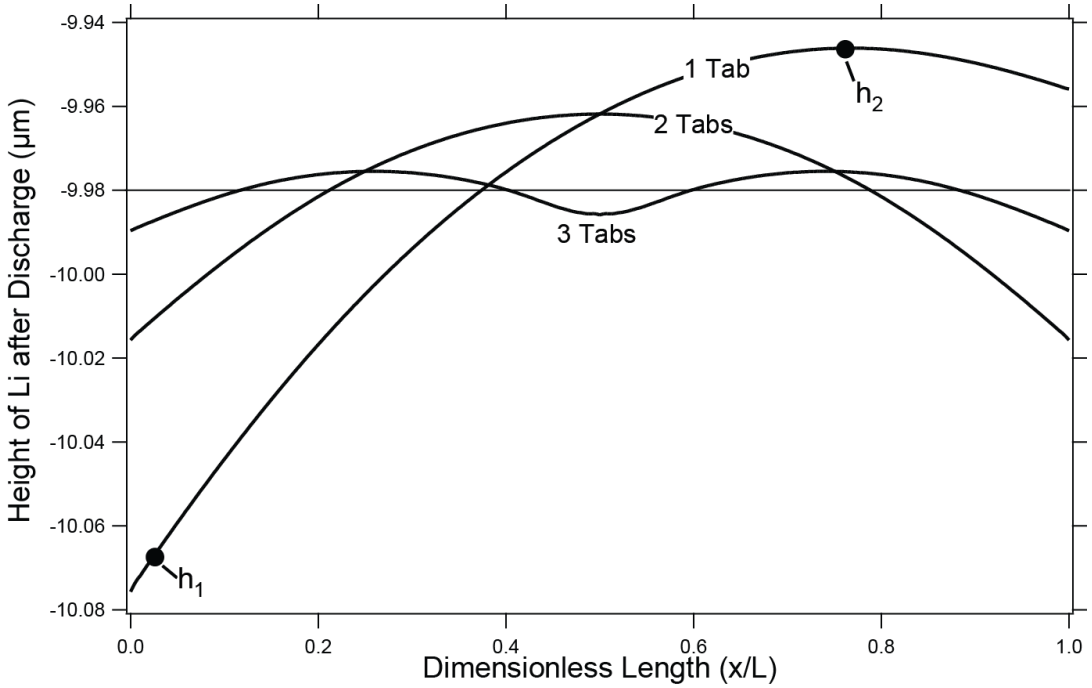

Figure 1.3. Height of the lithium negative electrode relative to its starting location with varying tab geometries after a discharge at a C/5 rate for 2.5 hours.

Here, three different tab geometries were used. The first was the standard configuration seen in Figure 1.1, where the positive and negative tabs are placed at opposite corners of the cell. The results of this arrangement can be seen in both Figures 1.3 and 1.4, where there is an asymmetric bias of the change in the height of the negative electrode interface toward the negative-electrode tab. One more tab was then added to both of the remaining corners of the cell, making the tab configuration symmetric and leaving the cell with two tabs on each electrode, one at each corner. A uniform current was applied at each of the two positive tabs such that each passed half of the total current. The result of this symmetric

tab placement was as expected, forcing the current distribution and consumption of lithium change to be symmetric as well. Next, one tab was placed half way between the two tabs along both the top and the bottom of the cell leaving the cell with three tabs evenly spaced at each electrode. Again, a uniform current was applied at each of the three positive tabs such that each passed one third of the total current. As expected, increasing the number of tabs forces the current density to become more uniform. This means that the degree of shape change diminishes with the end result being that if one had a continuous tab along both the positive and negative electrodes, the reaction rate would be completely uniform, and there would be no movement of lithium along the *x* axis at all.

Again, the same result can be achieved for the three-tab system by taking the two-tab geometry and halving the length of the cell. Similarly, as you diminish the length of the cell down to zero, you achieve a one-dimensional model that assumes a uniform reaction rate which would remove the movement of lithium in the *x* dimension.

As is shown in Figure 1.3, the geometry of the cell model has a large effect on the movement of lithium over the half cycle. However, without any nonlinearities, the lithium, although migrating during the half cycle, will return to its original starting position. To explain this further, on discharge, the current distribution is biased toward the left side of the cell, such as in Figure 1.2. This means that more lithium is consumed on the left side of the cell and less on the right leading to a nonuniform lithium distribution as seen in the 1-tab line in Figure 1.3. If the geometry were the only factor contributing to the current distribution, the we would expect that, during the charge phase, the current density would be equal and opposite to the discharge phase resulting in a bias toward the right side of the cell. This would result in the lithium being deposited at a faster rate on the right side of the cell, during charge, meaning that after a full cycle of a discharge followed by a charge, the lithium would have exactly returned to its starting position.

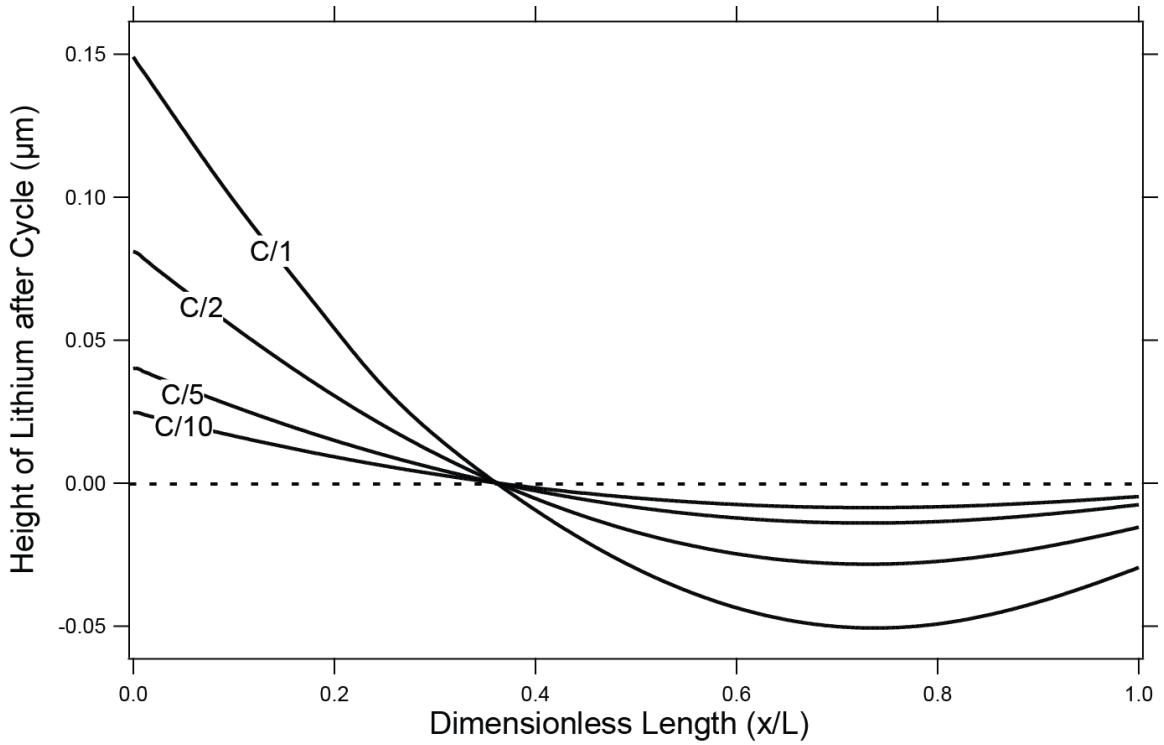

Figure 1.4. Height of the lithium negative electrode along the lithium/separator interface relative to its starting position after a discharge and charge cycle at various C-rates to a 50% depth of discharge.

If we look at Figure 1.4, however, we can see that this is not the case. Figure 1.4 shows significant movement of the lithium metal after a full cycle consisting of a discharge phase, a rest period of 1000 seconds, then a charge phase. The cell was cycled at various rates to a 50% depth of discharge calculated based on the positive electrode. After the full cycle of a discharge, rest, and charge phase, the net overall state of charge is the same as before the cycle began. The profiles seen in Figure 1.4 were taken immediately following the completion of the charging. All cycles were conducted galvanostatically.

From Figure 1.4, it is apparent that nonlinearities in the equations discussed in Section 1.2 are contributing to a build-up of lithium on the left side of the negative electrode, toward the negative tab. As is discussed in the next sections of this chapter, the two main nonlinearities contributing to this shape change are the open-circuit potential function in the positive electrode (Section 1.3b) and the concentration gradients of the salt in the liquid phase (Section 1.3c).

It should be noted here that the thinning of the negative electrode, on discharge, could be considered another nonlinearity. For example, as the cell is discharged, more lithium is removed on the left side of the cell than the right making the lithium thinner on the left side of the cell. Since the negative tab is also on the left side of the cell, in an extreme case, one could imagine pinching to occur where the lithium at that point becomes thin enough to change the

resistivity of the negative electrode considerably. In this model however, a maximum of 10 µm of lithium is removed out of a total thickness of 50 µm. Furthermore, it is not the change in the average thickness of the lithium, but rather the difference between the local thicknesses of the lithium that contributes to the nonlinearities of the system. As seen in Figure 1.3 the height of the lithium, after discharge, ranges from about -10.08 µm to -9.95 µm making the maximum change in thickness of the lithium about 0.13 µm. Therefore, while the changing conductivity of the negative electrode due to changes in the local thickness of the lithium is accounted for in the model through the incorporation of a moving boundary, this nonlinearity is small enough to be considered negligible. This phenomenon, however, is negligible due to the large excess of lithium at the negative electrode and this assumption the effects of a high utilization of the negative electrode is detailed in Subsection 2.2b in Chapter 2.

1.3b Open-Circuit-Potential Function

In this model there are two main nonlinearities that contribute to the accumulation of lithium on the left side of the negative electrode seen in Figure 1.4, the largest being the open-circuit-potential function or OCP. In order to describe how the OCP function affects the shape change, four different OCP functions (seen in Figure 1.5a) are modeled. These include the standard, experimentally measured OCP function for CoO_2 (Experimental OCP),[22] a sloped linear OCP function (Sloped OCP), a sloped linear OCP with a hyperbolic tangent function (Drop OCP), and a flat OCP function. Instead of plotting the final change in the height of the lithium after a full cycle (as seen in Figure 1.4), two points (h_1 and h_2) were used. These measure the height of the lithium relative to its starting position along the negative electrode/separator interface (seen in Figure 1.1). The difference between these points (h_1-h_2) is plotted in Figure 1.5b versus time for a full cycle at a C/5 rate with a 1000-second rest between the discharge and charge phases and a 2000-second rest after the full cycle. The points were chosen at 1 cm and 37.5 cm on the *x*-axis in order to achieve the maximum height difference between the two points while still minimizing errors that can occur at the edges of the model.

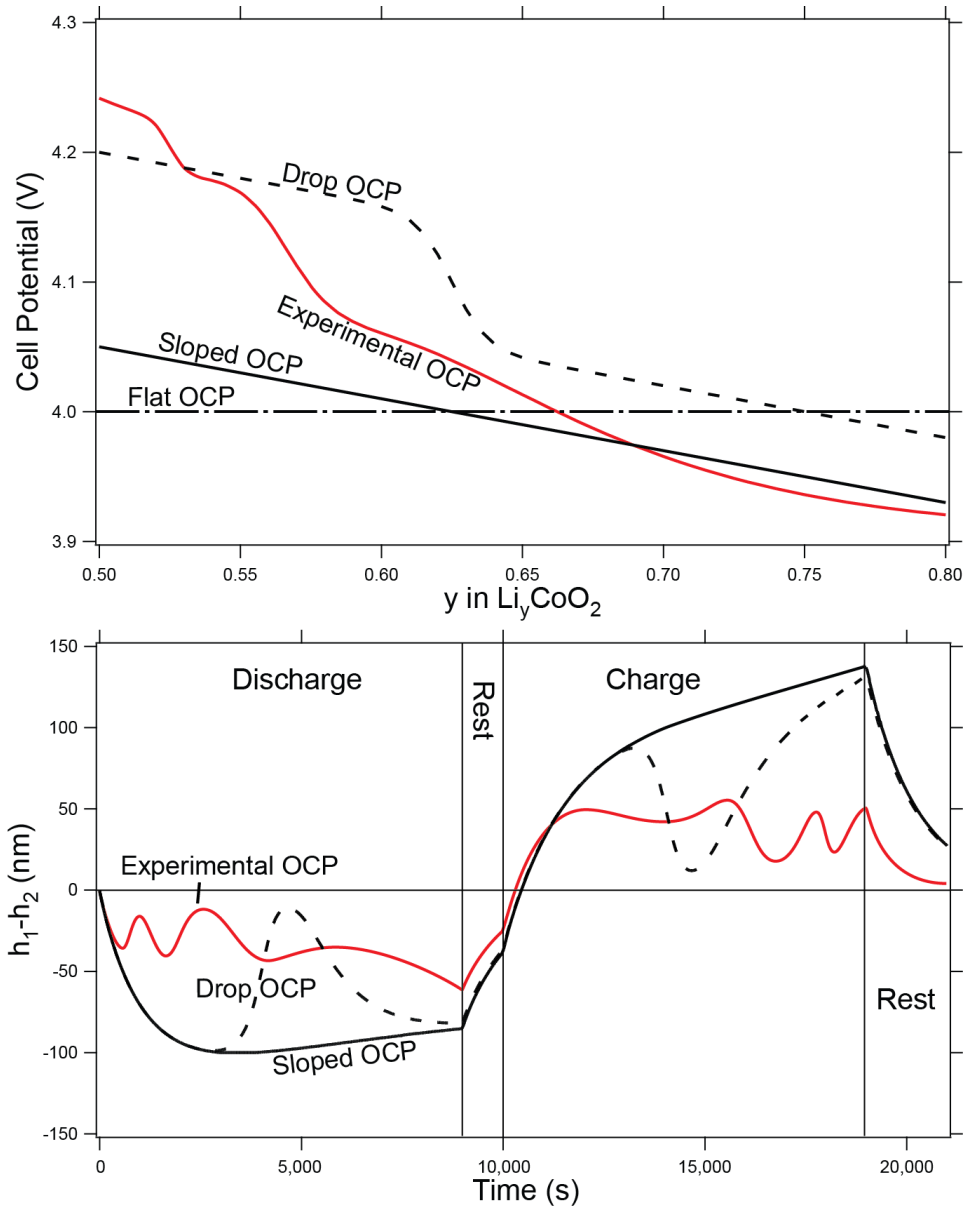

Figure 1.5. a) Open-circuit potential functions versus state of charge (y) and b) the corresponding difference in height between two points, h_1 and h_2 (seen in both Figure 1.1 and 1.3), versus time. The movement for the Flat OCP line is seen in Figures 1.7 and 1.8.

When plotting the difference in heights (h_1-h_2) versus time (Figure 1.5b), several interesting results can be seen. The plot of the experimental OCP for CoO_2 (Experimental OCP in Figure 1.5b) shows local minima and maxima during both the charge and discharge phases. This means that, starting from time zero, h_1 starts to dip below h_2 making the shape nonuniform and concave, similar to the 1-tab line in Figure 1.3. However, as we continue forward in time, we reach a local minimum, and the line starts to return toward zero, meaning that the shape of the

interface between the separator and negative electrode is starting to flatten out. The plot then goes through several local maxima and minima before reaching the global minimum right at the cutoff for the discharge portion of the cycle.

These local minima and maxima are due to changes in the slope of the OCP. To explain this further, during discharge for example, the lithium is consumed faster on the left side of the cell than the right. The opposite must be true for the positive electrode, where more lithium is being inserted into the active material on the left side of the positive electrode than on the right. This means that the local SOC in the positive electrode is higher on the left than on the right leading to a potential gradient within the positive electrode. As discharge continues, the average SOC in the positive electrode increases and the electrode passes through a section where the OCP is steeper. This steeper OCP section equates to a larger potential gradient for the same concentration gradient, which leads to the concentration gradient of the lithium in the active material in the positive electrode flattening because of the greater driving force. One of the ways that this is achieved is by increasing the reaction rate across the area of the positive electrode where the SOC is lower and decreasing the reaction rate where the SOC is higher. This has the effect of flattening the concentration gradients of the lithium in the solid phase of the positive electrode and flattening the lithium interface at the negative electrode. This phenomenon can especially be seen when comparing Sloped OCP and Drop OCP lines in Figure 1.5b (please note that the Drop OCP line has the same slope as the Sloped OCP line with the addition of a hyperbolic tangent).

When studying the Sloped OCP line in both Figure 1.5a and b, we can see that, when the slope of the OCP remains constant, the local minima and maxima are removed. However, a comparison of Sloped OCP and Drop OCP lines in Figure 1.5b shows that, as the SOC goes through the dip due to the hyperbolic tangent, the Drop OCP line departs from the Sloped OCP line. As the SOC passes completely through the hyperbolic tangent portion of the OCP, the Drop OCP line starts to return to its original path (Sloped OCP), as though the drop had never occurred. This theory has also been developed in the literature.[16, 18, 23]

The second effect that the OCP has on shape change in this model is that as we increase the slope of the OCP function, the shape change decreases. Again, this is caused by differences in the SOC or the concentration of lithium in the solid phase, which is governed by the OCP. For a given difference in potential between two points, there is a larger concentration gradient of lithium in the solid phase with a flatter OCP than with a steeper OCP function. That is, there is a greater driving force to decrease the concentration gradients in the solid phase with a steeper OCP than a flatter one. This can be seen when comparing the Experimental OCP line with the Sloped OCP line in Figure 1.5b.

The third interesting phenomenon in Figures 1.5a and b is that, during rest, the difference between h_1 and h_2 starts to return to zero, meaning that the shape of the lithium is flattening out when no external current is being passed. This flattening out of the negative

electrode during rest is, again, an effect of the OCP, which enhances the equilibration of lithium concentrations in the solid phase of the positive electrode. For example: after a discharge at a C/5 rate, more lithium at the negative electrode has been removed near the negative tab than near the edge closest to the positive tab (seen in the 1-tab line in Figure 1.3). This means that the concentration of lithium in the solid phase of the positive electrode is higher on the left side of the cell and lower on the right (seen in Figure 1.6 below). Because of the sloped OCP, there is a potential gradient due to the concentration gradient that drives the lithium in the positive electrode to equilibrate. Because of the length scales of the positive electrode (100 µm thick vs. 50 cm long), it is much easier for the lithium to cross through the separator and interact with the negative electrode than to diffuse through the positive electrode in the *x* direction. This can be seen qualitatively in Figure 1.6 where the lithium in the "Region of Higher Concentration" reacts into the electrolyte and passes through the separator depositing on the left side of the negative electrode. Concurrently, the exact same amount of lithium reacts into the electrolyte on the right side of the negative electrode and passes through the separator, intercalating into the right side of the positive electrode. This equilibrates the positive electrode while flattening the negative electrode.

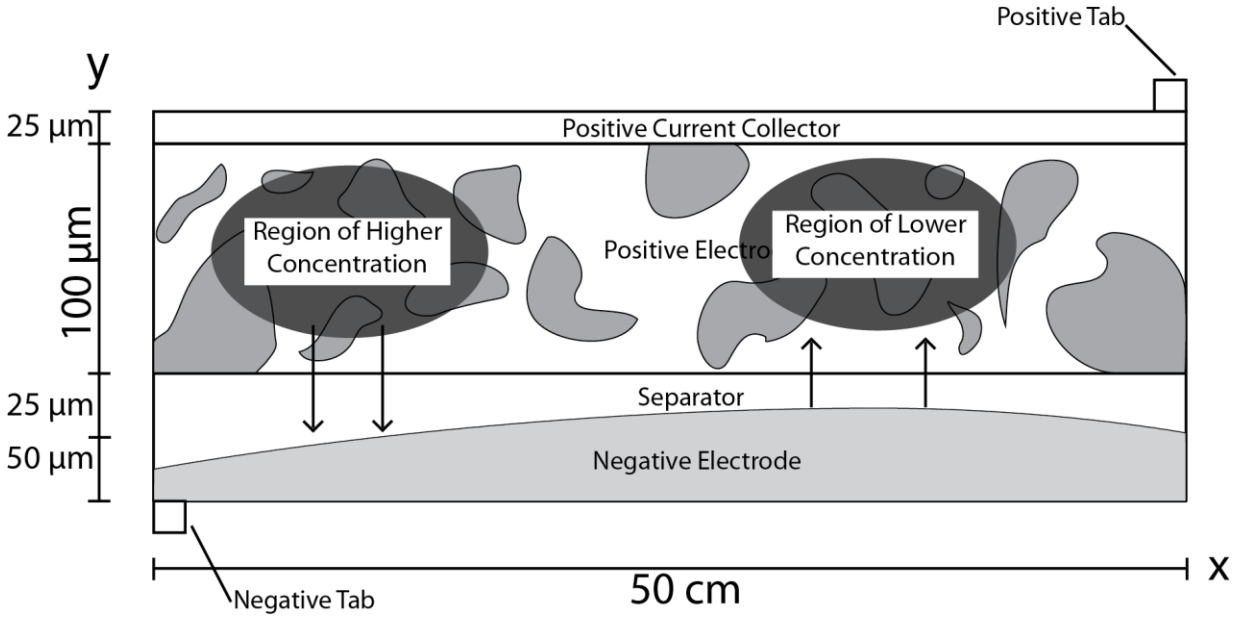

Figure 1.6. Cartoon of the shape of the lithium negative electrode and corresponding concentration of lithium in the active material of the positive electrode right after discharge. The arrows represent the direction of the flux of lithium due to the equilibration of the concentration gradients in the positive electrode during the rest phase directly following the discharge phase.

More quantitatively, this phenomenon can be seen in Figure 1.7 where the local current density along the surface of the negative electrode is measured at various times during an extended rest phase after a discharge half cycle at a C/5 rate to a 50% DOD. The zero-second line in Figure 1.7 corresponds to the current density immediately after discharge. As is expected, no net current is being passed during this rest phase, shown by the fact that the integral of the local current density is zero. However, there is still a local, nonzero current density during the rest period. To explain this phenomenon more completely, the lithium in the higher-concentration region of the positive electrode (the left side of the cell) crosses through the separator and deposits on the left side of the negative electrode causing the negative current density in that region. At the same time, the lithium on the right side of the negative electrode reacts into the solvent, diffuses through the separator and intercalates into the right lower-concentration region of the positive electrode causing the positive current density in that region. This creates a current-neutral process that both equilibrates the positive electrode and flattens the negative electrode. Of course, as can be seen in the Flat OCP line in Figure 1.8, if the OCP is flat, then there is no potential driving force to equilibrate the positive electrode, and the negative electrode will not flatten.

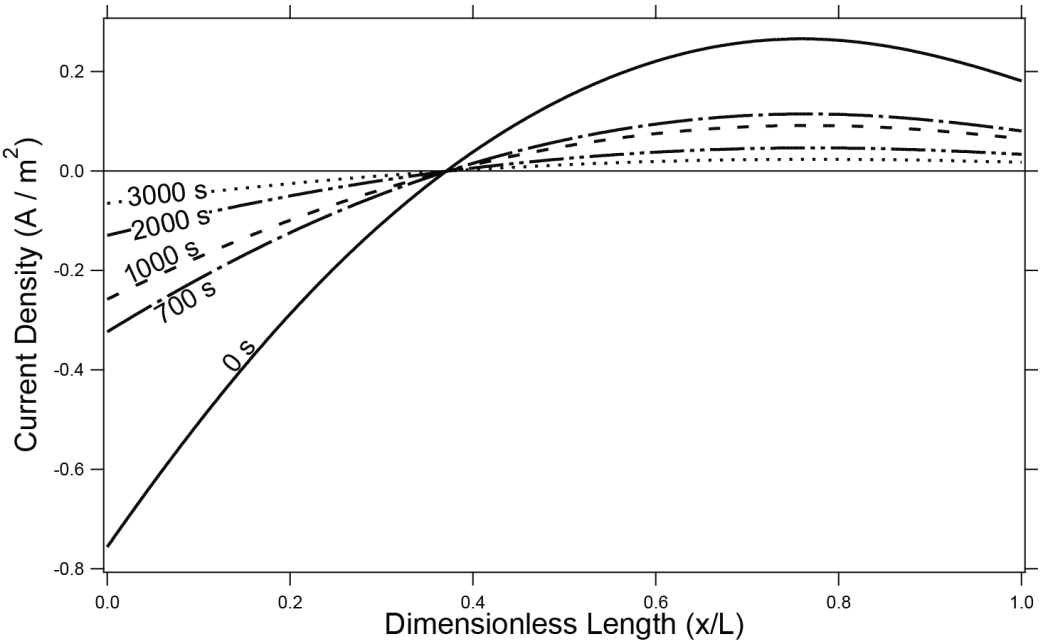

Figure 1.7. Local current density at the surface of the negative electrode following a discharge at a rate of C/5 for 2.5 hours. Zero seconds, corresponds to the start of the rest phase after discharge.

1.3c Diffusivity

The Flat OCP line in Figure 1.8 shows several additional interesting features. Along with the absence of any flattening of the negative electrode during the rest phases, the movement of the lithium during the half cycles is much more extreme. This follows from the trend that, as the slope of the OCP flattens, the extent of the shape change increases. With a flat OCP, the driving force for equilibrating the concentration gradients in the solid phase of the positive electrode is completely absent. This means that the positive electrode will act as if it were a very thin electrode with all of the lithium intercalating into and out of the very edge of the positive electrode nearest the separator and biased towards the negative tab. This leads to the state of charge at the edge of the positive electrode nearest the negative tab increasing up to around 2.5, which is clearly not physical. This result is simply because the limitation in the model for the extent of the SOC at any point in the positive electrode is based on the OCP and, with the OCP being held constant, that limitation is no longer present, leading to very large swings in the SOC.

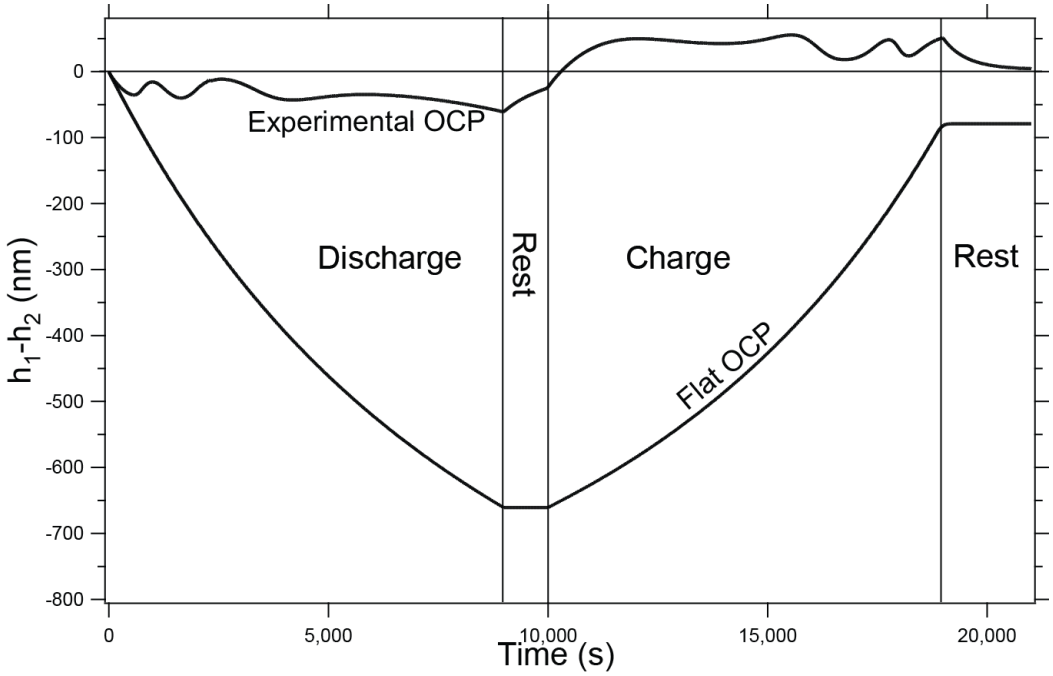

Figure 1.8. The difference in height between points h_1 and h_2 (seen in both Figure 1.1 and 1.3) versus time for two different OCP functions, Flat OCP and Experimental OCP, seen in Figure 1.5a.

The third phenomenon that can be seen in the Flat OCP line in Figure 1.8 is that even though the OCP is held constant, the shape of the lithium after a full cycle still doesn't return to zero, meaning that there still is a net shift of the lithium after cycling. This is due to the

concentration gradients in the liquid phase, and the effects of the concentration gradients can be seen clearly in Figure 1.9 below. Figure 1.9 again shows the movement of the lithium (h_1-h_2) at the negative electrode over time for two different OCP functions: the experimental OCP function for CoO_2 (Experimental OCP line in Figure 1.5a) and the flat OCP (Flat OCP line in Figure 1.5a). The solid lines represent the simulation being run under 'normal' conditions and are the same as those seen in Figure 1.5b for the Experimental OCP line and Figure 1.8 for the Flat OCP line. The dashed lines are for simulations run under the same conditions but with the diffusivity of the salt in the liquid electrolyte raised by 3 orders of magnitude. This makes the concentration gradients very flat and, as can be seen in the Flat OCP High Diffusivity line in Figure 1.9, without the nonlinearity of the concentration gradients or the OCP, the shape of the lithium returns back to zero after a full cycle. It should be mentioned again, however, that the significant movement seen during the half cycles is due to the geometry. It is also interesting to note that while the concentration gradients play a role when the OCP is flat (seen in the Flat OCP and Flat OCP High Diffusivity lines in Figure 1.9), when one compares the solid and dashed lines for the Experimental OCP case, no significant difference is seen in the movement. This shows us that the effect of concentration gradients on the shape change is much smaller than the effect that the OCP has.

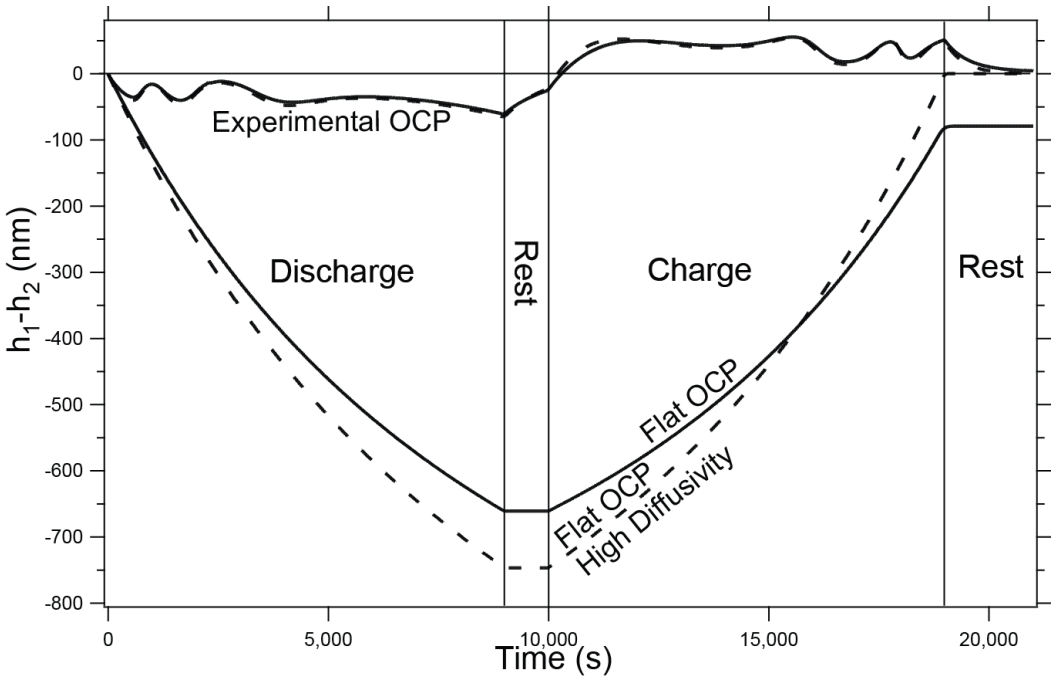

Figure 1.9. Comparison of the shape change (h_1 and h_2) over time when the diffusivity in the liquid phase is normal (solid lines) and is increased by three orders of magnitude (dashed lines) for two OCP functions, Flat OCP and Experimental OCP, seen in Figure 1.5a.

Along a similar line, the movement of the lithium with a liquid electrolyte will induce convection in the electrolyte. This convection can be considered, perhaps crudely, to be an enhancement of the diffusivity, which has been found to have a very limited effect on the movement of the lithium during cycling. Therefore, the convective term in the flux equation has been neglected for the sake of simplicity. The exclusion of the convection term in a liquid electrolyte system was also found to have a negligible effect on the concentration profiles in the work by Pollard et al.[24] Again, as can be seen when comparing the high-diffusivity Experimental OCP (dashed) and normal-diffusivity Experimental OCP (solid) lines in Figure 1.9, there is a small difference (a maximum of about 6%) in the movement of the lithium due to the increased diffusivity. This can be considered to be the maximum error incurred by the absence of convection terms and was deemed to be an acceptable level of error.

1.4 Conclusions

In this chapter, a two-dimensional model has been presented that is able to capture the movement of lithium during cycling. This model incorporates electrode tabbing, a moving boundary at the negative electrode, a CoO_2 intercalation electrode as the cathode, and a lithium-metal negative electrode. The positive electrode is modeled using porous electrode theory, the separator as a liquid electrolyte with a binary salt, and the total volume changes are assumed to be zero. Finally, the negative electrode in this model is twice the thickness required by stoichiometry in order to avoid the need for a separate negative current collector.

The model has been cycled at various rates, and it is seen that, even without dendrites, significant large-scale movement of lithium occurs both during each half cycle and after a full cycle of a discharge followed by a charge. More specifically, the lithium is depleted more near the negative tab, yet after a full cycle, there is a net migration of the lithium towards the negative tab. This migration was found to be caused by three separate phenomena. First, as was described in Section 1.3a, the geometry strongly affects the current density distribution which directly correlates to the asymmetric depletion of lithium during the discharge phase. The second driving force, discussed in Section 1.3b, is the open-circuit-potential function, the slope of which not only affects the magnitude of the movement, but also is the largest nonlinearity that contributes to the movement of lithium after a full cycle. The third and smallest contributor to the movement of the lithium is the concentration gradients in the liquid electrolyte which was detailed in Section 1.3c. We have seen that when the OCP is flat and the concentration gradients are reduced through increasing the diffusivity, the lithium will return to its starting position after a full cycle.

Throughout this chapter, only one cycle was modeled. This situation is very unlikely to come about in a real application, where repeated cycling is a given. Thus, Chapter 2 will take the same model, as described in this chapter, and look at the movement of lithium after several

cycles. Through this analysis, we shall see that there are several factors contributing to the continued movement of lithium after multiple cycles: the open-circuit-potential function, the depth of discharge, the rate of discharge and charge, and the length of the rest periods. In Chapter 2, we shall also see how these driving forces work together to cause the movement of lithium to reach a steady state.

The major assumption in this chapter was that the separator, while inhibiting dendrites, also allowed the lithium to move unhindered. However, in order to inhibit dendrites either a stiff polymer separator or a ceramic protective layer is needed. In Chapter 3 we see how the incorporation of a stiff polymer separator affects the movement of the lithium seen both in this chapter and in Chapter 2. Then, in Chapter 4, we look into the use of a ceramic to inhibit dendrites and calculate the stresses in a ceramic protective layer due to bending.

List of Symbols

a	Specific interfacial area	[m^2/m^3]
c_{1max}	Maximum concentration in solid	[mol/m^3]
c_i	Concentration of salt	[mol/m^3]
D_i	Diffusion coefficient of salt	[m^2/s]
F	Faraday's constant, 96,485	[C/eq]
$f_{\pm}$	Activity coefficient	[-]
i_0	Exchange current density	[A/m^2]
$\boldsymbol{i}_i$	Current density	[A/m^2]
i_{loc}	Reaction rate	[A/m^2]
j_n	Pore wall flux of lithium ions	[mol/m^3-s]
K	Exchange current density rate constant	[$mol^{0.5}/m^{0.5}$·s]
k_a	Anodic reaction rate constant	[m^3/s]
k_c	Cathodic reaction rate constant	[m^3/s]
κ_{eff}	Effective conductivity defined by Equation 1.16	[m^3/s]
κ_i	Conductivity	[S/m]
R	Universal gas constant, 8.314	[J/mol-K]
R_p	Radius of cathode material	[m]
T	Temperature	[K]
t_+	Transference number of Li^+	[-]
U_1	Open-circuit potential	[V]
α	Transfer coefficients	[-]
ε	Porosity of electrode	[-]
η_s	Overpotential	[V]
ϕ_i	Electric potential	[V]

Subscripts

0	initial value
1	solid phase
2	solution phase
CCa	current collector at the anode
CCc	current collector at the cathode

Chapter 2

Modeling Lithium Movement over Multiple Cycles in a Lithium-Metal Battery

2.1 Introduction

In Chapter 1, a two-dimensional model was presented that is able to capture the movement of lithium during cycling. The model was cycled at various rates, and we saw that, even without dendrites, significant large-scale movement of lithium occurred both during each half cycle and after a full cycle of a discharge followed by a charge. More specifically, we saw that, on discharge, the lithium was depleted more near the negative tab, yet after a full cycle, there was a net migration of the lithium towards the negative tab. This migration was found to be caused by three separate phenomena detailed in Section 1.3. First, as was described in Subsection 1.3a, the cell geometry strongly affects the current density distribution, which directly correlates to the asymmetric depletion of lithium during the discharge phase. The second driving force, discussed in Subsection 1.3b, is the open-circuit-potential function, the slope of which not only affects the magnitude of the movement, but also is the largest nonlinearity that contributes to the movement of lithium after a full cycle. The third and smallest contributor to the movement of the lithium is the concentration gradients in the liquid electrolyte which was detailed in Subsection 1.3c. We saw that when the OCP is flat and the concentration gradients are reduced by increasing the diffusivity, the lithium will return to its starting position after a full cycle.

Throughout Chapter 1, only one cycle of a discharge followed by a rest period and then a charge was modeled. This situation is very unlikely to come about in a real application, where repeated cycling is likely. Thus, this chapter will take the same model, as described in Section 1.2, and look at the movement of lithium after several cycles.

To give an overview of the model developed in Section 1.2: the model incorporates electrode tabbing, a moving boundary at the negative electrode, a CoO_2 intercalation electrode as the cathode, and a lithium-metal negative electrode. The positive electrode is modeled using porous electrode theory, the separator as a liquid electrolyte with a binary salt, and the total volume changes are assumed to be zero. Finally, the negative electrode in this model is twice the thickness required by stoichiometry in order to avoid the need for a separate negative

current collector. All equations for the model are detailed in Subsection 1.2a and are based on the papers by Doyle et al. and Fuller et al.[1-5] and Newman and Thomas-Alyea.[6] As such, the reader is referred to Subsection 1.2a in Chapter 1 for a more complete description of the equations.

In this work, modeling was done using COMSOL Multiphysics, which uses a finite-element approach. The model geometry, shown in Figure 2.1, attempts to recreate a standard battery configuration. In order to capture the behavior of interest, electrode tabbing is included where, during discharge, the current is drawn from the top of the positive tab and inserted into the bottom of the negative tab. Here, the *y* dimension of the model is through the thickness of the cell sandwich, which can be seen to be 200 µm thick, and the *x* dimension is taken to be along the length of the unwound cell sandwich and is 50 cm long. The negative electrode is modeled as a lithium-metal layer with a varying, finite thickness, and the positive electrode consists of porous $LiCoO_2$. Film formation at the lithium/separator interface and volume changes of the positive electrode and of the overall cell were not considered. The separator is a liquid electrolyte which is assumed to fill any gaps when the lithium shrinks during discharge and moves into excess head space as the thickness of the lithium anode thickens during charge. In other words, the separator is able to expand and contract freely with the movement of the negative electrode, thereby keeping the total volume of the cell sandwich constant. The liquid electrolyte allows for the free movement of the lithium negative electrode and results in the worst-case scenario of lithium migration during cycling. This constitutes a through-plane cross-section of, what could be considered, a typical 18650 cell construction.

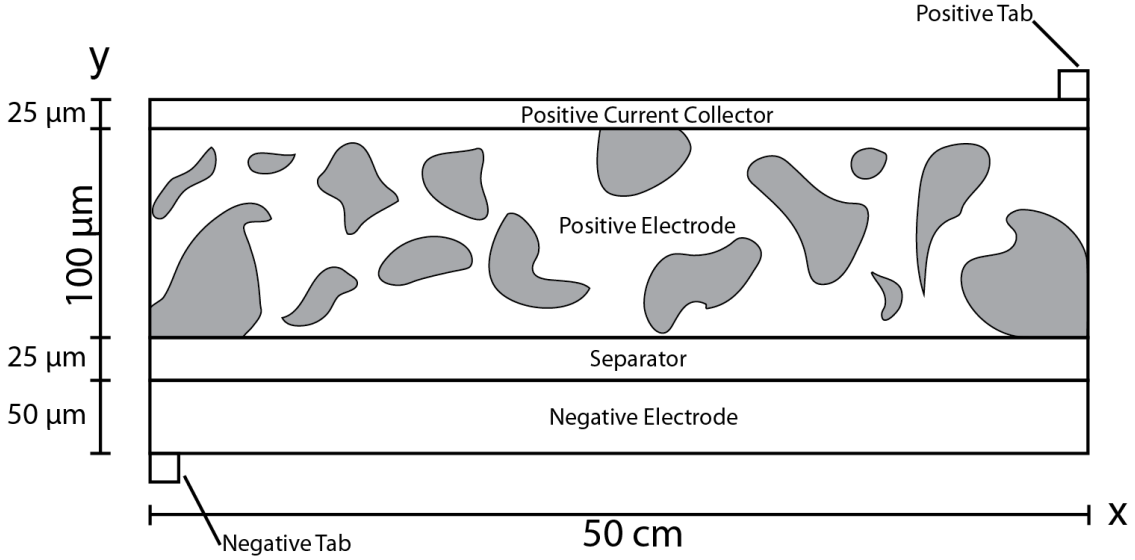

Figure 2.1. Two-dimensional model geometry of a lithium-metal battery, consisting of a lithium-metal negative electrode, a liquid-electrolyte separator, composite cathode, and aluminum positive current collector. The negative electrode in this model is twice the thickness necessary in order to make unnecessary a separate negative current collector

2.2 Results and Discussion

Since, in this chapter, we look at the movement of lithium over time for extended cycling, we shall adopt a new method for characterizing the movement of lithium in the *x*-direction along the separator/negative electrode interface. As opposed to describing the movement of lithium with the difference in heights (h_1-h_2) of the lithium at the negative electrode (as described in Subsection 1.3b and seen in Figure 1.5b in Chapter 1), the characterization in this chapter takes a somewhat more physical significance. Here, the magnitude of the shape change is characterized by converting the integral of the height of the lithium relative to its average height to a number of coulombs of lithium. We see this a bit clearer in Figure 2.2 where the height of the lithium negative electrode along the lithium/separator interface is plotted relative to its average position during the discharge phase at a C/5 rate.

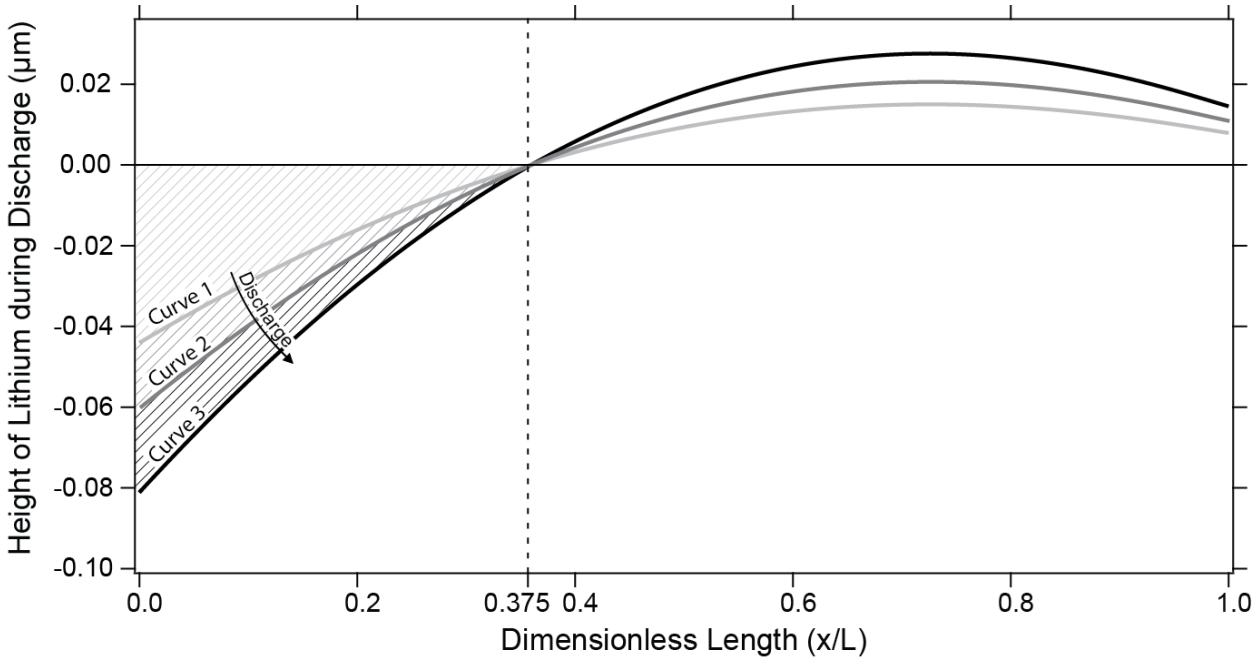

Figure 2.2 Height of the lithium negative electrode along the lithium/separator interface relative to its average position as the cell is discharged at a C/5 rate. Curve 1 is the height of lithium after 200 seconds of discharge, Curve 2 after 400 seconds of discharge, and Curve 3 after 600 seconds of discharge.

As we can see in Figure 2.2 as well as from Figure 1.5b in Chapter 1, as the cell is discharged, the lithium is removed more at the left side of the negative electrode than at the right side. This creates a nonuniform distribution in the height or thickness of the lithium. If we take the average height of the lithium as zero, then, as the lithium is removed, the 'zero line'

moves with it, causing the second derivative of the curve to increase while the integral of the curve remains at zero. This can be seen if we look at the progression of the discharge in Figure 2.2. 'Curve 1' occurs after 200 seconds of the discharge phase. As the cell is discharged further, the height of the lithium relative to its average height reaches 'Curve 2' and then 'Curve 3.' We can see that the integral of each line remains at zero; however, as we discharge the cell from 'Curve 1' to 'Curve 3,' the area on the left side of the curve (the hatched area) increases. If we define the average height of the lithium to be zero, each parabola crosses the x-axis at the same point. We can use this knowledge to our advantage by defining the negative portion of the curve as the left side $(0 \leq \mathrm{x/L} \leq 0.375)$ and the positive portion of the curve as the right side $(0.375 < \mathrm{x/L} \leq 1)$. By taking the integral of the curve from $\mathrm{x/L} = 0$ to $\mathrm{x/L} = 0.375$, we can calculate the area which, through the use of the molar density of lithium and Faraday's constant, can be transformed into the number of coulombs of lithium that have passed from the right side of the negative electrode $(\mathrm{x/L} > 0.375)$ to the left side $(\mathrm{x/L} \leq 0.375)$. This can also be thought of as the number of coulombs that have passed across the dashed vertical line at $\mathrm{x/L} = 0.375$ shown in Figure 2.2.

Since we arbitrarily chose to use the integral of the left side of the curve, as the cell discharges the hatched area becomes more negative as well as the number of coulombs of lithium that have passed to the left. This can be seen in Figure 2.3b, where the lines become negative as the cell is discharged in the left side of the plot.

2.2a The Slope of the Open-Circuit-Potential Function

As was determined in Chapter 1, the slope of the open-circuit-potential (OCP) function is the largest nonlinearity contributing to the movement of lithium along the negative electrode/separator interface. Thus, in order to determine the effect that the slope of the open-circuit-potential function has on the movement of the lithium after multiple cycles, we use a linear approximation to the open-circuit-potential function.

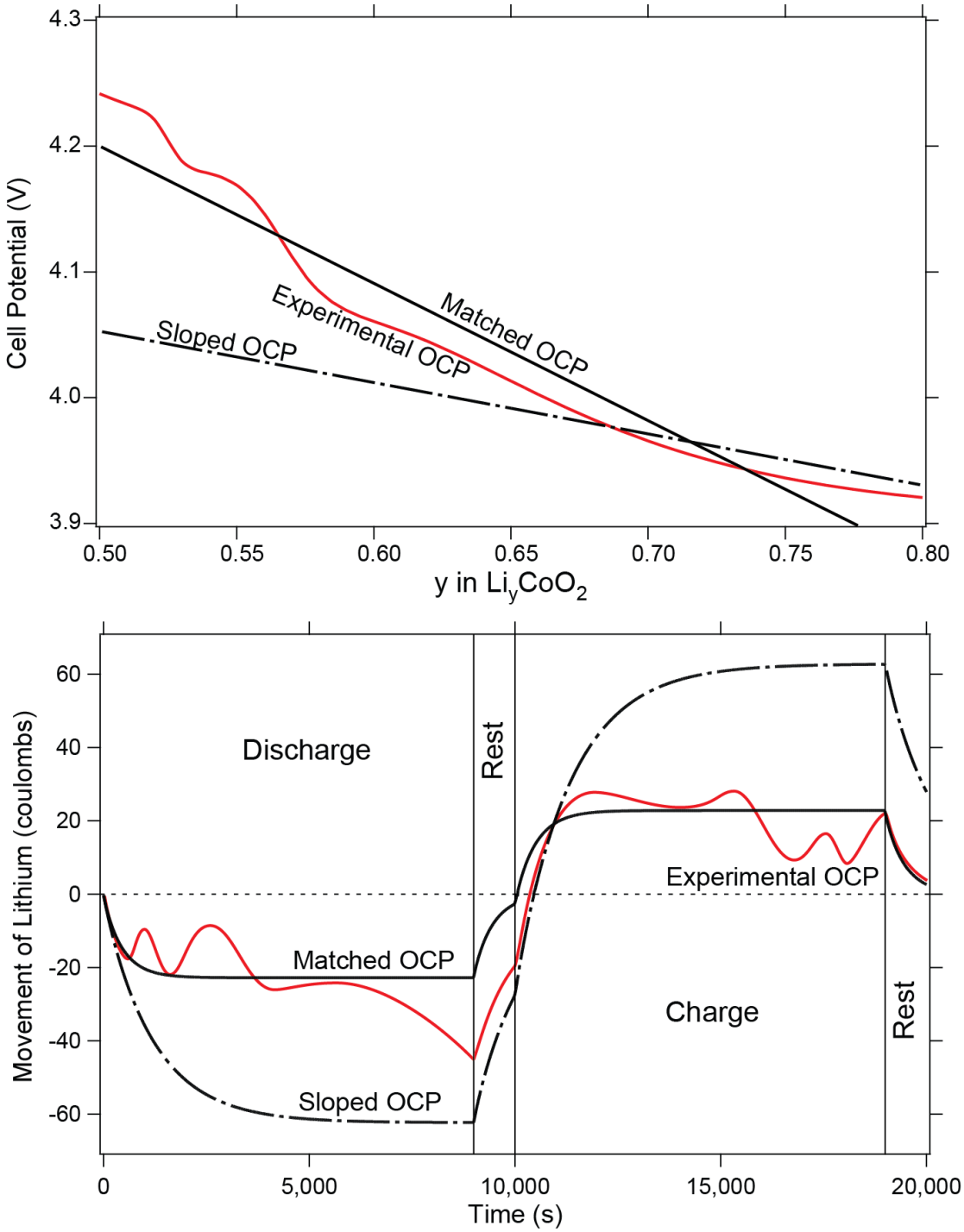

Figure 2.3. a) Open-circuit potential functions versus state of charge (y) and b) the corresponding movement of lithium (measured in coulombs of lithium passed from the right side of the negative electrode $(x/L > 0.375)$ to the left side $(x/L \leq 0.375)$) during one cycle at a rate of C/5 to a 50% depth of discharge. A concave down plot, as seen in Figure 2.2, translates to a negative number in Figure 2.3b.

From Figure 2.3a, we see two different linear open-circuit-potential functions compared to the open-circuit-potential function measured experimentally for a Li_yCoO_2 positive electrode versus lithium. The slope of the 'Matched OCP' line was taken to match the average slope of the experimental OCP. This is seen when comparing the 'Matched OCP' and 'Experimental OCP' lines in Figure 2.3b, where the movement of lithium is somewhat similar. The ‘Sloped OCP’ line was chosen because it is significantly flatter than either the experimental or the 'Matched OCP' line, and thus, provides a good contrast for comparison with the ‘Matched OCP’ line.

Through Figure 2.3b, we find that both the 'Matched OCP' and 'Sloped OCP' lines reach a quasi-steady state where they nearly flatten out. To explain this further: during discharge, for example, the lithium is removed faster from the left side of the cell than the right, causing a nonuniform lithium distribution. During the beginning of the discharge, the quickly becoming less uniform and the slope of the lines in Figure 2.3b are steep. As the discharge progresses, the slope of the lines in Figure 2.3b lessen, signifying that the removal of lithium is becoming more uniform. Finally, after enough time, both the 'Matched OCP' and the 'Sloped OCP' lines become nearly flat signifying that the lithium at the negative electrode is being removed uniformly from the negative electrode, causing the shape of the lithium at the negative-electrode/separator interface to remain the same as discharge continues. This quasi-steady state is caused by the potential difference in the positive electrode due to differing states of charge (SOC) and the changes in the ohmic drop in the separator canceling the tendency for a nonuniform current distribution from the effect of geometry.

To put it another way, as was described in Chapter 1, the geometry of the cell (due to tabbing and differing resistances of the positive current collector and negative electrode) causes a nonuniform current distribution (seen in Figure 1.2). As the battery discharges, the nonuniform current density causes the SOC in the positive electrode to vary. This means that there is also a variation of the potential in the positive electrode that depends on the slope of the OCP. Furthermore, the nonuniform current density at the negative electrode will cause the lithium to become thinner on the left side of the cell than the right (seen in Figures 1.3 and 2.2) leading to an increase in the distance between the separator and the negative on the left side of the cell relative to the right. This variation in the thickness of the separator causes the ohmic drop in the separator to be larger on the left than the right. Both the variation in the potential in the positive electrode and, to a smaller extent, the variation of the ohmic drop in the liquid phase of the separator work in tandem to force the current distribution to become more uniform and, as can be seen in Figure 2.3b, leads to a quasi-steady state in the distribution of lithium along the negative-electrode/separator interface during both discharge and charge.

To be clear, this quasi-steady state is due to there being a considerable excess of lithium at the negative electrode. This excess allows for the resistance of the negative electrode to remain somewhat constant throughout the discharge. Furthermore, because there is a significant amount of excess lithium, the difference in thickness between the thinnest and

thickest portion of the negative electrode is quite small compared to the overall thickness of the electrode. If, for example, the cell were somehow able to discharge enough so that a significant amount of lithium at the negative electrode was removed, the movement (seen in Figure 2.3b) would start to decrease again due to the resistance of the negative electrode increasing. This assumption of considerable excess lithium is discussed in much more detail in Subsection 2.2b.

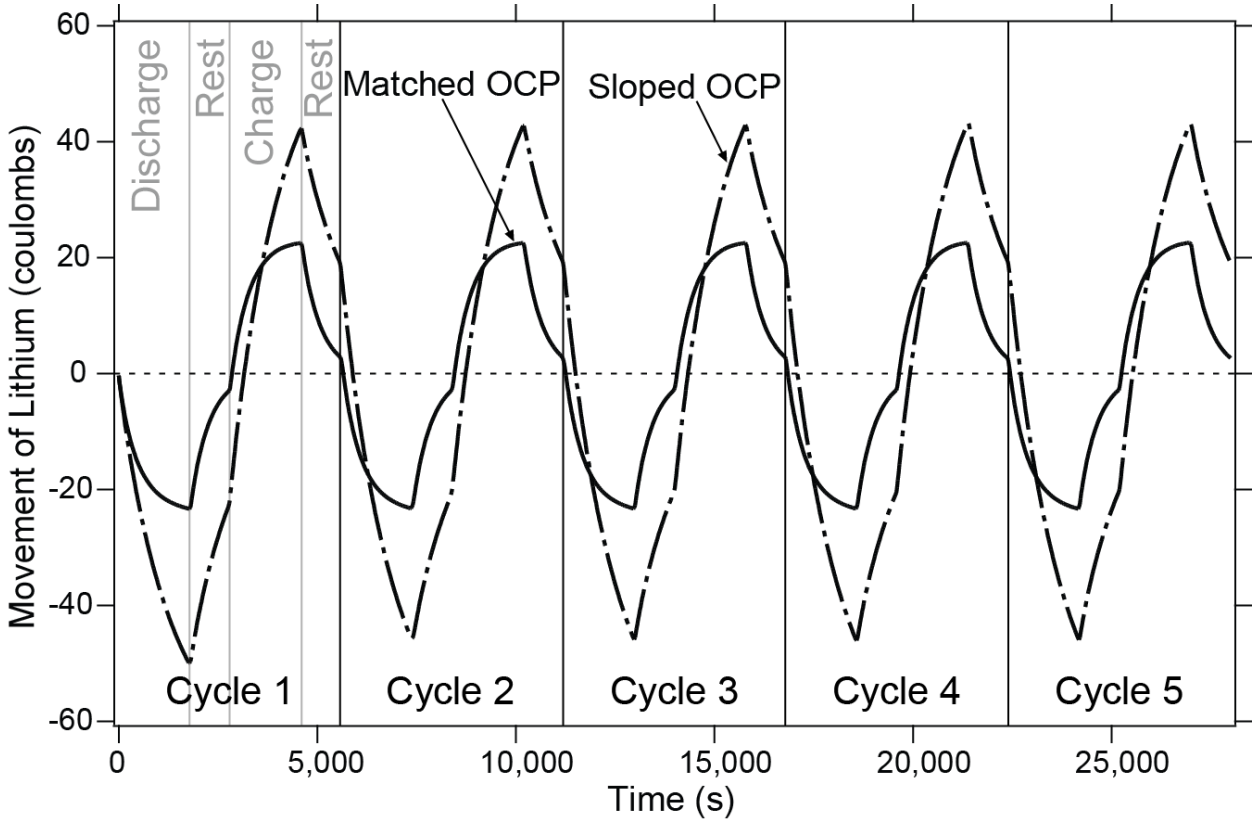

Figure 2.4. Movement of lithium along the lithium/separator interface during five cycles with two different linear OCP slopes at a rate of C/5 to a 10% depth of discharge based on the positive electrode.

From Figure 2.4, we can see that the magnitude of shape change for the lithium in both the 'Sloped OCP' and 'Matched OCP' cases have reached a quasi-steady state where the movement after one cycle is nearly the same as after five. Immediately following charging, for the 'Matched OCP' line, about 22.5 coulombs of lithium in the negative electrode have moved from the right side of the cell to the left, and, after five cycles, that number remains almost exactly the same. This is nearly the steady state (at 22.85 coulombs) that was reached in Figure 2.3b. When looking at the 'Matched OCP' line in Figure 2.4, we can see that the movement immediately following charging reaches 42.3 coulombs after the first charge and 43.2 coulombs after the fifth. This is a modest increase especially when compared to the movement seen in

the first cycle and, as will be shown in the following Subsections, is due to pinching (Subsection 2.2b), the limited depth of discharge (Subsection 2.2d), and rest periods (Subsection 2.2e). That is to say that, cycling to a higher depth of discharge or allowing for longer rest periods will cause the movement of lithium seen immediately after charging to remain the same after the fifth cycle as after the first.

2.2b Pinching or High Depths of Discharge for the Negative Electrode

In the previous section we saw that after five cycles at a C/5 rate to a 10 percent depth of discharge based on the positive electrode, there was no noticeable increase in the movement for the 'Matched OCP' case and only a slight increase in the movement for the 'Sloped OCP' case. We also saw, in Figure 2.3b, that the movement of the lithium reaches a quasi steady state where, after a certain point, discharging the cell does not appreciably increase the movement of lithium. These simulations were run with a large amount of excess lithium such that the conductivity of the negative electrode did not change appreciably. For example, in Figure 2.4, the cell was cycled to a 10 percent depth of discharge based on the positive electrode which translates to only a 4 percent depth of discharge based on the negative electrode. To put it another way, during cycling only 4 percent of the lithium was utilized.

In this Subsection, we explore the effect of cycling to a high depth of discharge based on the negative electrode. This can be achieved in two ways, by increasing the capacity of the positive electrode or decreasing the thickness of the negative electrode. Here, we have chosen to decrease the thickness of the negative electrode so that the positive electrode can be kept the same as in the other Subsections to allow for an easier comparison. By decreasing the thickness of the negative electrode, we have also increased the resistivity of the negative electrode thereby increasing the bias of the current distribution toward the left side of the cell. Thus, we expect a much more nonuniform current distribution and a much larger shape change to occur with a thinner negative electrode.

Because of the higher utilization of the negative electrode, the resistance of the negative electrode changes substantially during cycling where it increases as the cell is discharged. In addition, the nonuniform thickness due to the nonuniform current density will exacerbate the situation, possibly leading to a situation where the lithium at the negative tab is very thin or nonexistant and leads to a cell failure.

In the figures below, the thickness of the lithium at the negative electrode is decreased from 50 to 15 µm, and the cell was cycled over 60 percent of the capacity of the positive electrode corresponding to about an 80 percent depth of discharge for the negative electrode. As can be seen in Figure 2.5 below, while the negative electrode started out at 15 µm thick, after the first discharge at a C/5 rate (based on the positive electrode), about 12 µm of lithium

was stripped from the negative electrode leaving an average of 3 µm of lithium remaining. However, because of the nonuniform current distribution, the thickness at the negative tab or x/L=0 has diminished to about 2.4 µm for the 'Matched OCP' case and to about 1.5 µm for the 'Sloped OCP' case.

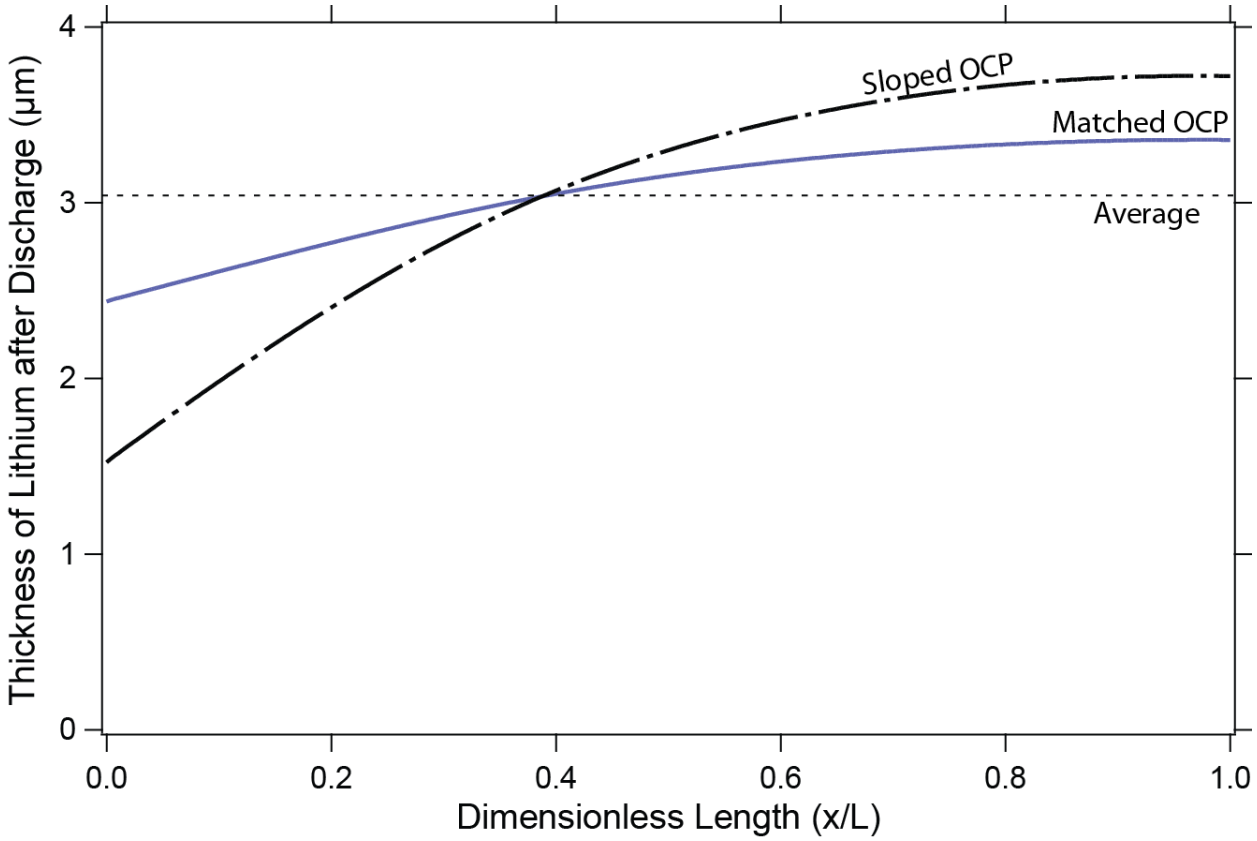

Figure 2.5. Thickness of the lithium negative electrode along the lithium/separator interface after the first discharge at a rate of C/5 to an 80% depth of discharge based on the negative electrode. The initial thickness of the negative electrode was 15 µm.

In order to compare the movement of lithium seen with a high depth of discharge for the negative electrode to the movement seen in the previous Subsection, we convert the movement of lithium at the end of discharge into the number of coulombs of lithium passed across the $\mathrm{x/L} = 0.375$ line seen in Figure 2.2. In Figure 2.6 below, we see the movement of lithium at the negative electrode measured in coulombs at the end of discharge for several different cases. In Figure 2.6, the movement seen after one discharge (Cycle Number 1) for the 'Sloped OCP' and 'Matched OCP' correspond to the thickness profiles with the same names seen in Figure 2.5. After 5 cycles we can see that for the 'Matched OCP' case, the movement after discharge has increased modestly from -445 coulombs to -449 coulombs. This corresponds to a modest thinning of the left point of the negative electrode from 2.44 µm to 2.425 µm.

When comparing this to the 'Sloped OCP' case, we see that, similar to Figures 2.3b and 2.4, as the slope of the OCP decreases, the movement increases. Furthermore, the 'Sloped OCP' case sees more movement after cycling than the 'Matched OCP' case, increasing from -1031 coulombs after the first discharge to -1048 coulombs after the fifth. This corresponds to thinning of the left point of the negative electrode from 1.525 μm to 1.49 μm. The 'Low Depth of Discharge' case corresponds to the movement of the lithium after discharge for the 'Matched OCP' case in Figure 2.4. In this simulation the negative electrode is initially 50 μm thick and only 4 percent of the lithium is used during cycling. From this comparison we can see that the amount of lithium movement is much lower, and the movement of lithium after 5 cycles is the same as after 1.

The final case seen in Figure 2.6 is the 'Matched OCP C/2 Rate' case where the simulation was run under the same conditions as the 'Matched OCP' case (80 percent lithium utilization) but at a higher, C/2 rate based on the positive electrode. From this case we can see that increasing the C-rate of cycling both increases the movement seen as well as exacerbates the increase in movement seen after multiple cycles. The effect of the C-rate on the movement of lithium is discussed in more detail in Subsection 2.2c.

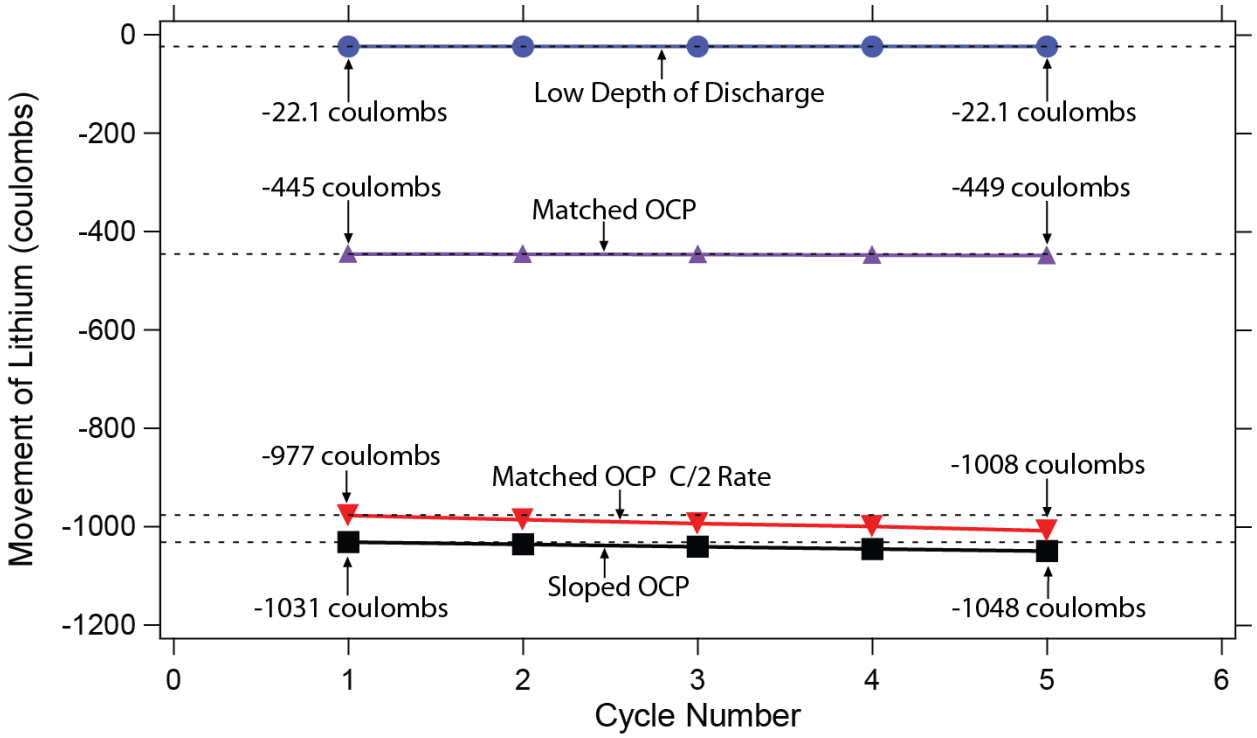

Figure 2.6. Movement of lithium at the negative electrode after discharging as measured in coulombs of lithium passed from the right side of the negative electrode $(x/L > 0.375)$ to the left side $(x/L \leq 0.375)$. The 'Matched OCP', 'Sloped OCP', and 'Matched OCP C/2 Rate' simulations were run to an 80% depth of discharge, and the 'Low Depth of Discharge' line was run to a 4% depth of discharge based on the negative electrode and is the movement seen after discharge in Figure 2.4. The dashed horizontal lines are for reference.

In Figure 2.6, the increase in movement over cycling was calculated for the first 5 cycles. It is of interest, however, to determine the progression of this movement over extended cycling. Thus, the 'Sloped OCP' case in Figure 2.6 was extended to 50 cycles, the results of which can be seen in Figure 2.7 below. Rather than plot the movement of lithium along the negative electrode in coulombs passed across the x/L=0.375 plane, in Figure 2.7 we instead plot the minimum thickness of the negative electrode (which remains at x/L=0) after discharging for cycles 1 through 50. From this, we can see the progression of the thinning of the left side of the negative electrode. If this thinning were allowed to progress unchecked, it would result in a pinching off of the negative electrode from the negative tab when the thickness seen in Figure 2.7 reaches zero.

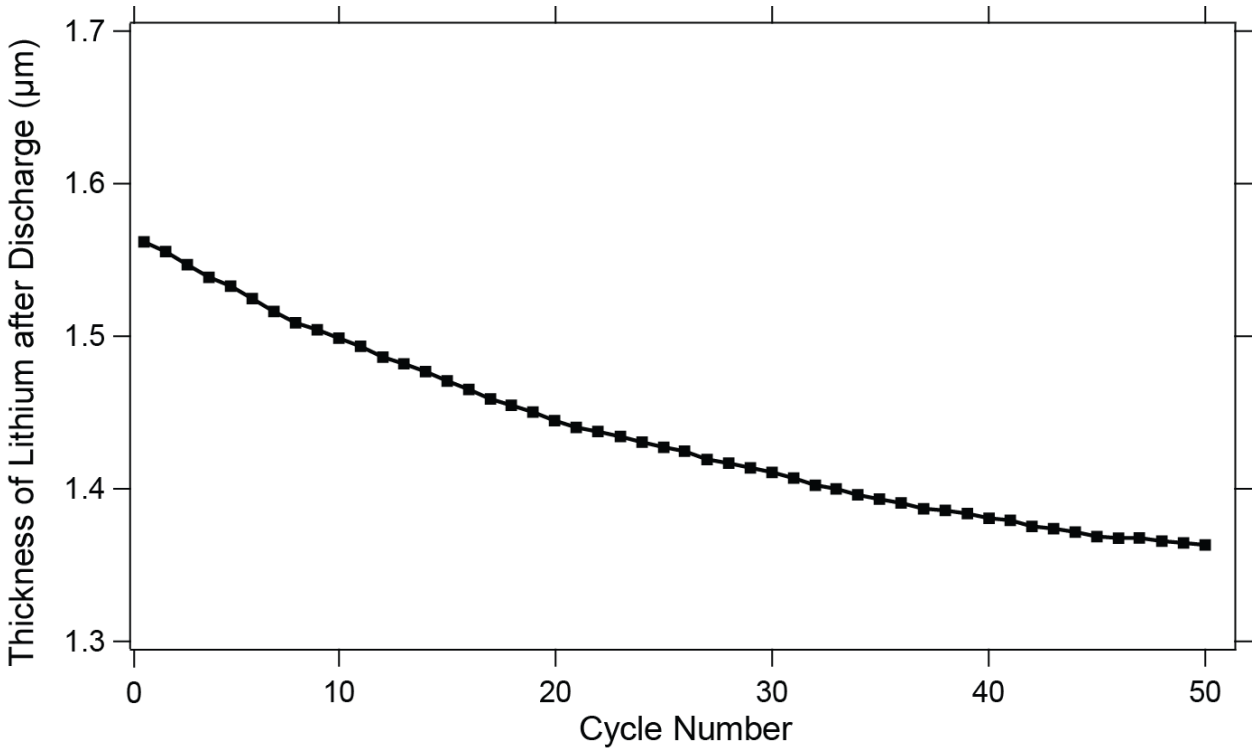

Figure 2.7. Minimum thickness of the lithium negative electrode after discharge at a rate of C/5 with the Sloped OCP function to an 80% depth of discharge based on the negative electrode. The initial thickness of the negative electrode was 15 µm.

From Figure 2.7 we can see that the thickness of the lithium at the left side of the negative electrode diminishes as cycling continues as was expected from Figure 2.6. However, it is readily apparent that after extended cycling the thinning of the negative electrode slows down. To put it another way, the thickness of the left side of the negative electrode, after the discharge during cycle 1, is 1.562 µm. After discharging during cycle 2, the thickness is 1.555 µm which is a decrease of 0.093 µm or 5.95 percent. If we now progress to cycles 49 and 50, the thickness of the lithium after discharge is 1.364 µm and 1.362 µm respectively, which is a decrease of only 0.002 µm or 0.15 percent. As we can see from this example, the thinning off the electrode slows down substantially after only 50 cycles.

In order to project the thinning of the negative electrode out to thousands of cycles we plot the data seen in Figure 2.7 against the log of the Cycle Number and fit it to a quadratic function with good agreement. The accuracy of the fit is tested by only using the first 25 cycles and projecting the fit out to cycle 50 (the red line in Figure 2.8). As can be seen in Figure 2.8, the fit used shows good agreement to the thickness of the lithium, and, through this fit, we find that the thickness of the lithium at the negative tab will reach zero after about 40,000 cycles. However, as was seen in Figure 2.6, increasing the C-rate during cycling and increasing the depth of discharge of the negative electrode will exacerbate the thinning of the left side of the

negative electrode and decrease the number of cycles required to cause the thickness of the lithium to reach zero.

Clearly 50 cycles is not nearly enough data to be able to extrapolate out to 40,000 cycles, and the error is most likely sizable; however, I believe that this illustrates the point that this phenomenon should not be considered a major failure mode. Furthermore, including a separate negative current collector will completely solve this issue where, even if the lithium is completely stripped from a segment, the rest of the electrode is still connected to the negative tab.

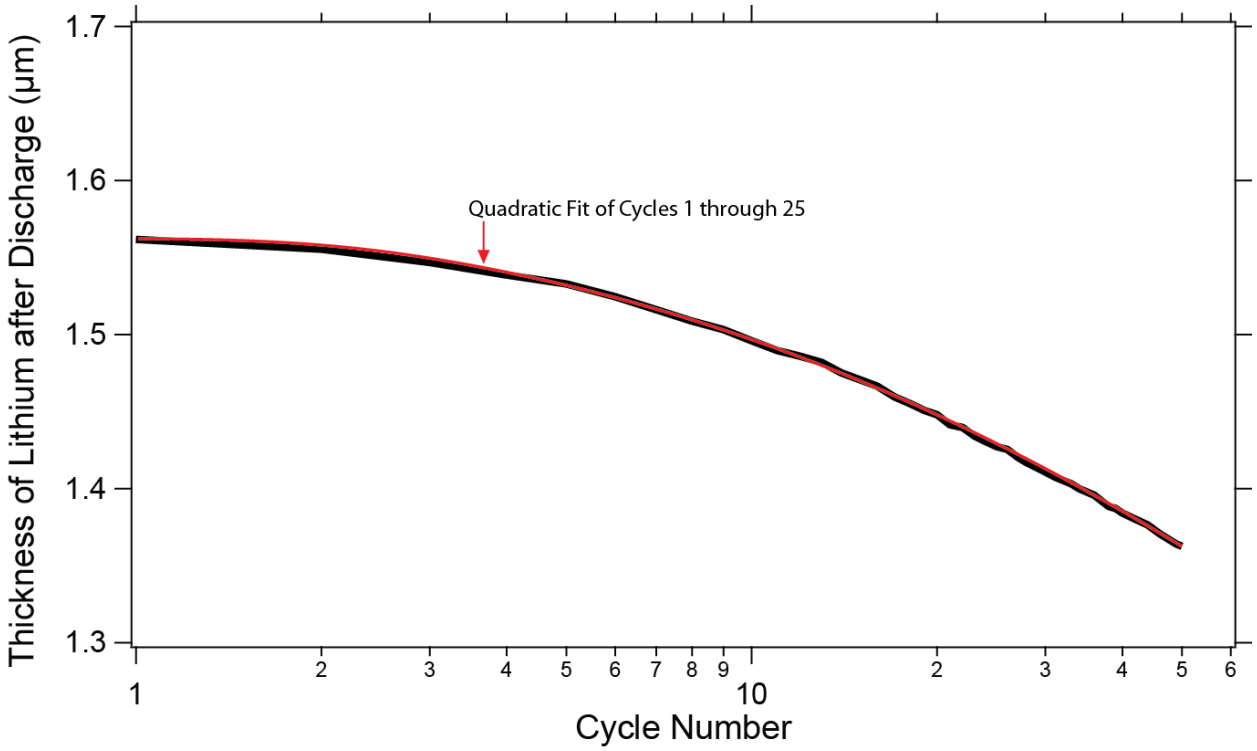

Figure 2.8. Minimum thickness of the lithium negative electrode after discharge at a rate of C/5 with the Sloped OCP function to an 80% depth of discharge based on the negative electrode. The red line is a quadratic fit of cycles 1 through 25 and is projected out to cycle 50 showing a good fit. The slight wavering of the line is due to errors that occur at the edges of the model.

It should be noted here that while only the thickness of the lithium at the end of discharge was plotted, during charge, lithium is deposited returning the negative electrode back to its original thickness with a slight accumulation of lithium on the left side of the cell as seen in Chapter 1. Furthermore, after extended cycling, while the lithium at the left side of the cell is thinning at the end of discharge, at the end of charge the thickness is increasing, meaning that

magnitude of the swing in the local state of charge at the left side of the cell is increasing during cycling.

2.2c The Effect of the C-rate on Cycling

In Subsection 2.2a we saw that, given enough time, and with excess lithium at the negative electrode, the movement of lithium will reach a quasi-steady state and the rate at which this steady state is achieved as well as the magnitude of the movement is determined, in part, by the slope of the OCP. Furthermore, as we see in Figure 2.4, the quasi-steady state seen after one cycle is preserved after multiple cycles.

Both Figures 2.3b and 2.4 were cycled at a C/5 rate. In Figure 2.8, however, we can see the results of cycling the model at a C/5 rate, a C/2 rate, and a C/1 rate. The cycling was performed under the same specifications as in Figure 2.4, with 1,000 second rests following the discharges and charges to a 10 percent depth of discharge (based on the positive electrode), and with a 50 μm thick negative electrode. The OCP function used in these simulations is the 'Sloped OCP' line in Figure 2.3a for the 'C/5 Rate' line, 'C/2 Rate' line, and the 'C/1 Rate' line. The 'C/1 Rate, Matched OCP' line uses the 'Matched OCP' from Figure 2.3a. All the simulations are cycled to 10% of the capacity of the positive electrode. Rather than view the entirety of the movement of the lithium while cycling, the points in Figure 2.8 represent the movement of lithium immediately after charging.

As we can see from Figure 2.8 below, at the C/5 rate, similar to the 'Sloped OCP' line in Figure 2.4, a steady state for the movement of the lithium is reached where the movement after cycle 5 is the same as after cycle one. For the 'C/1 Rate' line, however, we see a substantial increase after the first cycle where the movement starts at 48.3 coulombs after one cycle and climbs to 61.3 coulombs after five. By comparing the 'C/1 Rate' line with the 'C/5' rate line, we can see that increasing the rate of discharge and charge of the cell while holding the depth of discharge and rest periods constant increases the total movement of the lithium and causes the movement to increase as cycling continues.

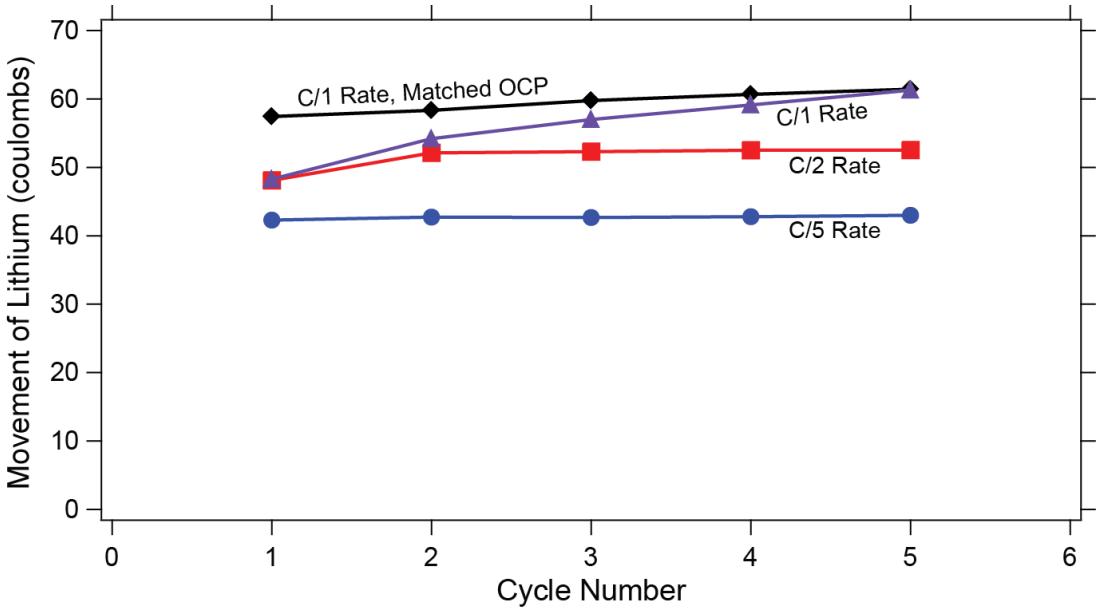

Figure 2.8. Accumulation of lithium as measured in coulombs of lithium on the left side of the negative electrode immediately after charging. All simulations were run to a 10% depth of discharge based on the positive electrode with 1,000 second rests following both the discharge and charge. The OCP function is the 'Sloped OCP' line as seen in Figure 2.3a unless otherwise noted.

Before explaining the increase in the movement at the C/1 rate, let us first compare it to the 'C/1 Rate, Matched OCP' line. In Subsection 2.2a we concluded that decreasing the slope of the OCP function increased the movement of the lithium. In Figure 2.8, however, when comparing the 'C/1 Rate, Matched OCP' line with the 'C/1 Rate' line we see that, after the first cycle, more lithium has accumulated on the left side of the cell in the 'C/1 Rate, Matched OCP' than the 'C/1 Rate' line where the slope of the OCP is lower. This phenomenon can be explained by looking at a more detailed plot of the movement of lithium over five cycles as is seen in Figure 2.9 below.

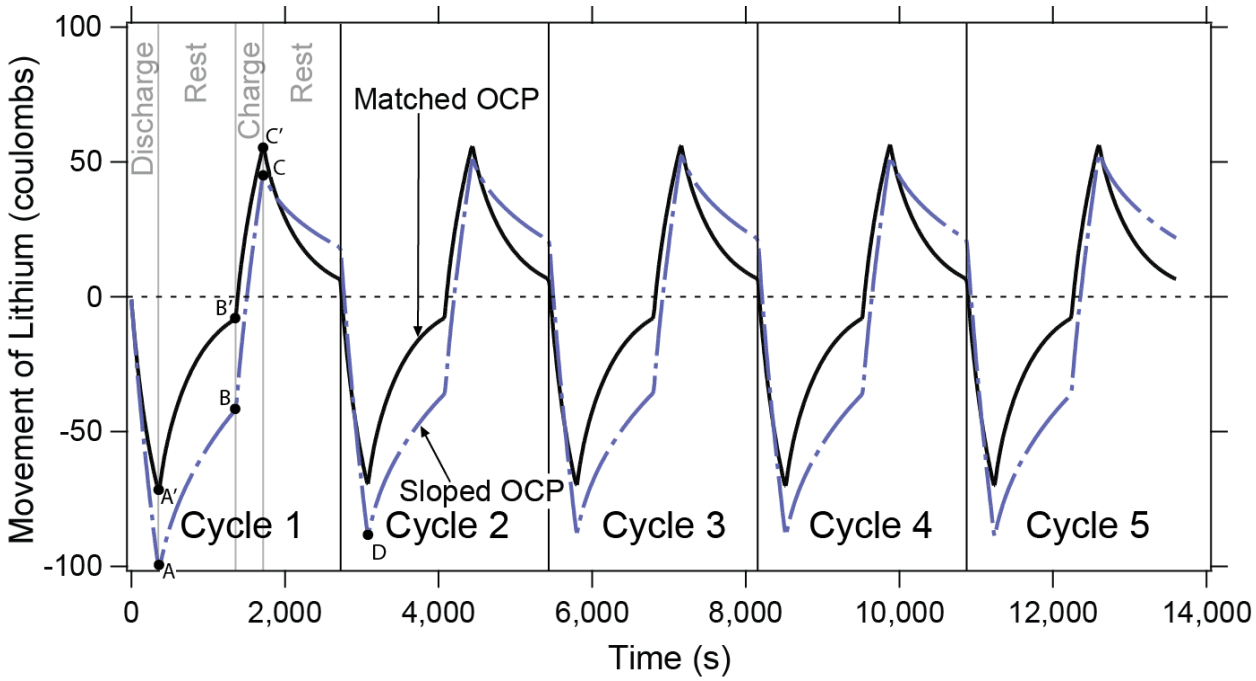

Figure 2.9. Movement of lithium along the lithium/separator interface during five cycles with two different linear OCP slopes at a rate of C/1 to a 10% depth of discharge based on the positive electrode.

In Figure 2.9, when comparing point A to point A', we see that more movement does occur for the 'Sloped OCP' line than the 'Matched OCP' line as would be expected from the slopes of the OCP functions. During rest, both lines relax toward zero, but the 'Sloped OCP' line does not relax as much as the 'Matched OCP' line. This can be seen in Figure 2.9 by noticing that the difference between points A and B is less than the difference between points A' and B'. This is due to the flatter OCP for the 'Sloped OCP' case, meaning that there is less of a potential gradient in the positive electrode driving the negative electrode toward uniformity. This reduced relaxation combined with the greater movement on discharge means that, at the start of charge, the 'Sloped OCP' line is more negative than the 'Matched OCP' line (point B is more negative than point B'). When comparing the difference between points B and C to the difference between points B' and C', we see that the movement during charging is greater for the 'Sloped OCP' case than the 'Matched OCP' case. However, because the 'Sloped OCP' line starts out more negative at point B, even though there is more movement during charge, after charge, the 'Sloped OCP' line at point C still remains below the 'Matched OCP' line at point C'.

Along those lines, we can also see that smaller relaxation during the rest phases is one phenomenon that contributes toward the 'Sloped OCP' line increasing its movement after each subsequent charge phase (seen in the 'C/1 Rate' line in Figure 2.9). On the first discharge, the lithium starts as a uniform thickness before becoming concave down. Then, after the charge phase, the lithium has accumulated on the left side of the cell causing the shape to become

convex at point C. During the subsequent rest phase, the lithium is allowed to relax, but since it does not reach a uniform thickness, on the second discharge phase, it starts positive, or concave up and must flatten out before becoming concave down. This means that, although the magnitude of the movement of the lithium remains nearly the same between the first and second discharge phases, the movement immediately after the second discharge phase is less negative than after the first. This can be seen by comparing point A with point D in Figure 2.9.Taking this analysis one step further, we can see that at the end of the rest following the second discharge, the 'Sloped OCP' line is less negative than at point B. Since the total movement during the charge remains nearly the same for the second charge as it was for the first, the shape of the lithium following the second charge is ultimately more positive, since it started from a smaller negative number.

2.2d Depth of Discharge

In Figures 2.4, 2.8, and 2.9, cycling was limited to a 10 percent depth of discharge based on the positive electrode which limits the movement of lithium during each cycle. This can be seen by comparing the 'Sloped OCP' and 'Matched OCP' lines in Figure 2.3b to the same lines in Figure 2.4 where, in Figure 2.3b, the movement of lithium at the end of discharge or charge is more pronounced than in Figure 2.4. Although limiting the depth of discharge limits the movement of lithium seen in each cycle, it also causes the movement to increase after each successive cycle. This can be seen at the higher C-rates in Figure 2.8 where the movement of lithium continued to increase after the first cycle. This phenomenon was discussed at the end of Subsection 2.2c and can be seen in Figure 2.10 below. Here we see that limiting the depth of discharge limited the movement seen during each discharge and charge phase. This, combined with the limited rest period, means that the movement does not reach a quasi-steady state after the first cycle and thus, multiple cycles are needed for the movement to equilibrate. In the case of the C/5 rate of cycling in Figure 2.4, even though the depth of discharge was held to only 10 percent of the total capacity of the positive electrode, the cell was given sufficient time to equilibrate so that no further movement of lithium during cycling was seen. Of course, for the case of the C/1 rates, both increasing the depth of discharge and increasing the rest period will help the cell to equilibrate, reducing the increase in movement after the first cycle. In this Subsection we discuss the effect of increasing the depth of discharge, and in Subsection 2.2e we discuss the effect of the rest period.

In Figure 2.10 below, we see the results of one cycle at a C/1 rate to a 90 percent depth of discharge. For the 'Matched OCP' case, the movement during both the discharge and charge phases nearly flattens out. For the case of the 'Sloped OCP' line, however, the flatter OCP function and high rate of discharge and charge keep the movement from reaching a quasi-steady state even at a 90 percent depth of discharge. Because of this, we expect that, similar to

the ‘C/1 Rate’ line in Figure 2.8, the movement seen immediately after charging will increase during cycling for the ‘Sloped OCP’ case although to a lesser extent than was seen in Figure 2.8. We also expect a similar result for the ‘Matched OCP’ case where cycling to a 90 percent depth of discharge limits the increase in movement during cycles 2 to 5.

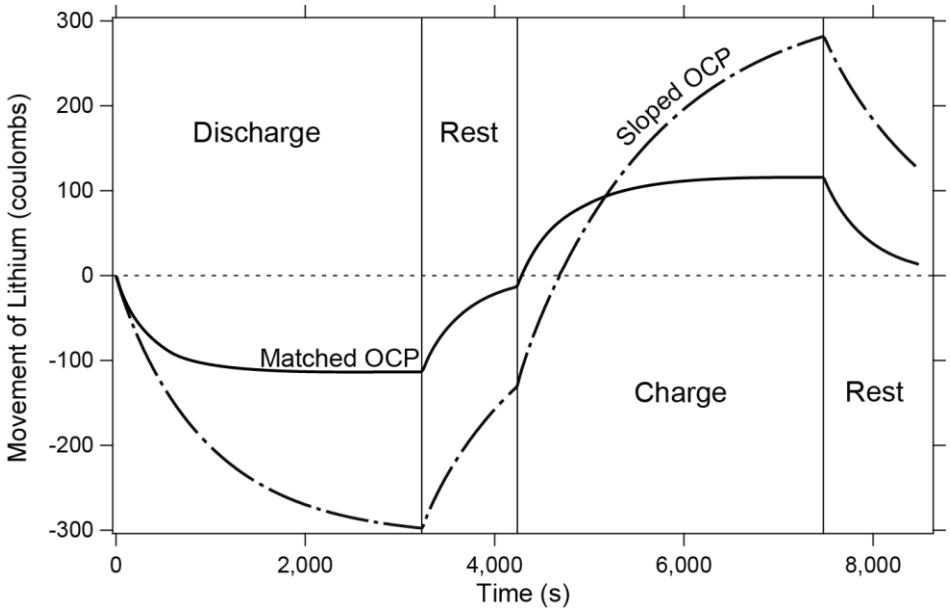

Figure 2.10. Movement of lithium along the lithium/separator interface during one cycle with two different linear OCP slopes at a rate of C/1 to a 90% depth of discharge based on the positive electrode.

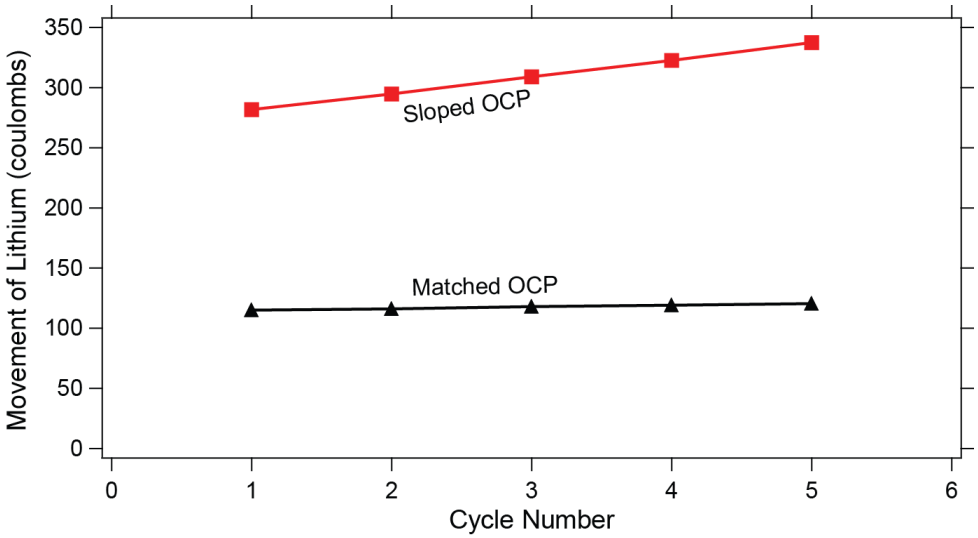

Figure 2.11. Accumulation of lithium as measured in coulombs of lithium on the left side of the negative electrode immediately after charging. All simulations were run at a C/1 rate to a 90% depth of discharge based on the positive electrode with 1,000 second rests following both the discharge and charge phases.

In Figure 2.11, we can see the results of cycling a cell at a C/1 rate, to a 90 percent depth of discharge over five cycles. Similar to Figure 2.8, the movement seen in Figure 2.11 is the movement immediately after charging. Although not readily apparent, increasing the depth of discharge during cycling from 10 percent to 90 percent does limit the increase in movement seen after the first cycle. For example, in the case of the simulation run with the 'Matched OCP' function, at a 10 percent depth of discharge, the movement immediately following charging after the first cycle is 57.4 coulombs and after the fifth cycle is 61.4 coulombs or a 7 percent increase (seen in Figure 2.8). When the depth of discharge is increased to 90 percent however, the movement after the first cycle is increased to 115 coulombs and after five cycles, it reaches 120.4 coulombs or a 4.7 percent increase (seen in Figure 2.11). The difference between the 90 percent and 10 percent depth of discharge is more noticeable for the simulations with the 'Sloped OCP' function. Here, with a 10 percent depth of discharge, after the first cycle, 48.3 coulombs of lithium have accumulated on the left side of the cell and after 5 cycles, 61.3 coulombs of lithium have accumulated, a 27 percent increase. Increasing the depth of discharge to 90 percent again increases the movement seen after the first cycle to 282 coulombs, but after five cycles, the accumulation reaches 337.5 coulombs, which is a 20 percent increase.

This increase in movement can also be limited by extending the rest periods, however, even with very long (10,000 second) rest periods following the discharge and charges, the movement after each cycle continues to increase. This is due to the nonlinearity of the pinching of the negative electrode discussed in Subsection 2.2b. For the case off a 90 percent depth of discharge based on the positive electrode (as in Figures 2.10 and 2.11), even with 50 μm of lithium, during discharge, 18 μm of lithium is stripped from the negative electrode which is 36 percent of the total lithium. Furthermore, because of the high rate of discharge, there is a somewhat significant difference in the thickness of the lithium at the left side of the cell compared to the middle. From Subsection 2.2b, we learned that this nonlinearity causes the movement of the lithium to increase during cycling which, in this Subsection, is seen because of the high depth of discharge and high rate of cycling.

2.2e Rests

From Figures 2.9 and 2.10, we saw that not only are the C-rate and depth of discharge important, but, as is especially seen in Figure 2.9, a short rest limits the relaxation of the lithium at the negative electrode. In Figure 2.12 below, we have plotted the movement of lithium immediately after charging, cycling at a C/2 rate to a 10 percent depth of discharge with a 'Sloped OCP' function in the positive electrode. The '1,000 second Rest' line in Figure 2.12 corresponds to the 'C/2 Rate' line in Figure 2.8. Through changing only the rest periods during cycling, we see that decreasing the rest from 1,000 seconds both decreases the amount of movement seen after the charge phase and causes the movement to increase after each

successive cycle. The reason for this is explained in Subsection 2.2c in the paragraphs under Figure 2.9.

Conversely, when we increase the rest period from 1,000 seconds to 10,000 seconds, we see that the accumulation of lithium on the left side of the cell immediately after charging increases and we see no further increase in accumulation after the first cycle. Again, this is due to the fact that the lithium was allowed to relax back toward uniform after the discharge and charge phases. This means that, at the start of cycle 3 for example, the lithium in the cell is almost in exactly the same place as at the start of cycle 2 and, therefore, the two cycles will behave nearly identically.

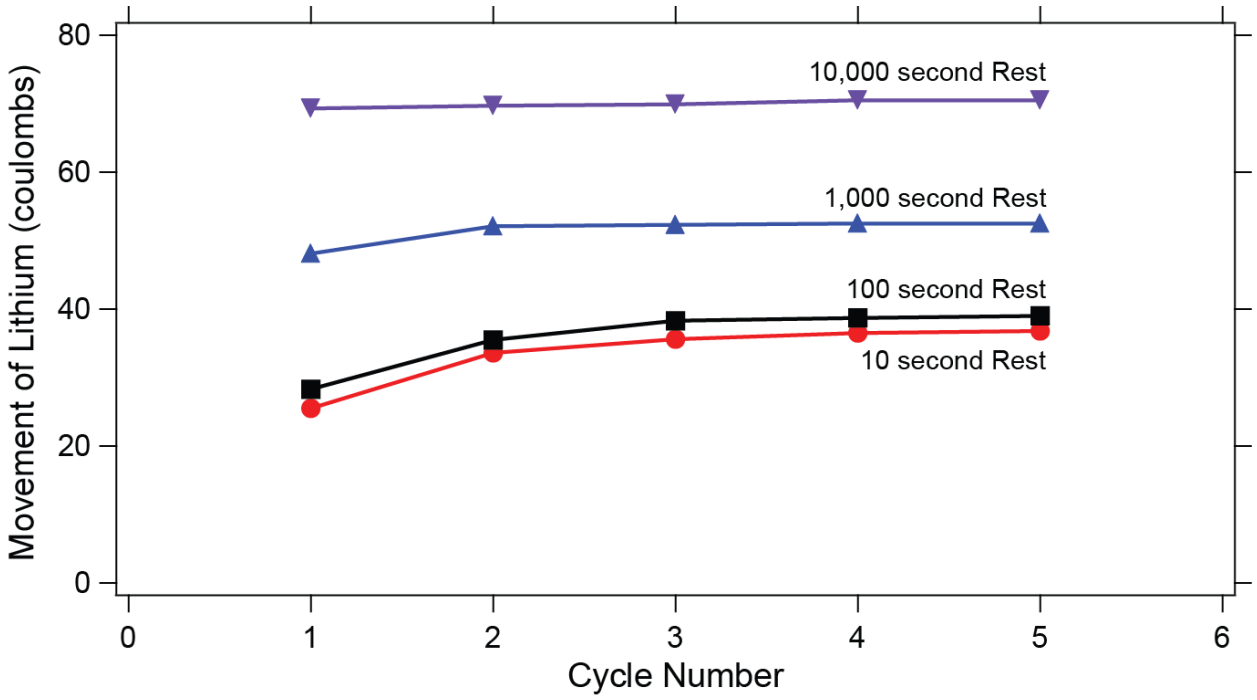

Figure 2.12. Cycling at a C/2 rate with varying rests to a 10% DoD measured immediately after charging. The slope of the OCP is the 'Sloped OCP' function seen in Figure 2.3a.

In Figure 2.12, we plotted the accumulation of lithium immediately after charging and varied the rest periods from 10 to 10,000 seconds. We saw that increasing the rest period increased the accumulation of lithium immediately after charging; however, we have also noted that during the rest phase, the lithium will relax back toward uniform. Therefore, in Figure 2.13, we plot the accumulation of lithium at the end of the rest phase following charging. From Figure 2.13, we see that increasing the rest phase decreases the movement of lithium after each complete cycle. For example, with a 10 second rest, the accumulation after each complete cycle is almost exactly the same as the accumulation of lithium immediately after the charge phase since, with only 10 seconds to relax, the lithium will not have moved appreciably. This can be seen when comparing the '10 second Rest' line in Figure 2.13 to the ’10 second Rest’ line

in Figure 2.12. On the other hand, after resting for 10,000 seconds, the lithium has returned to nearly uniform, as can be seen from the '10,000 second Rest' line in Figure 2.13. It should be noted that both Figures 2.12 and 2.13 are cycled under exactly the same conditions, and the only difference between lines with the same name is at which point the movement of lithium was calculated.

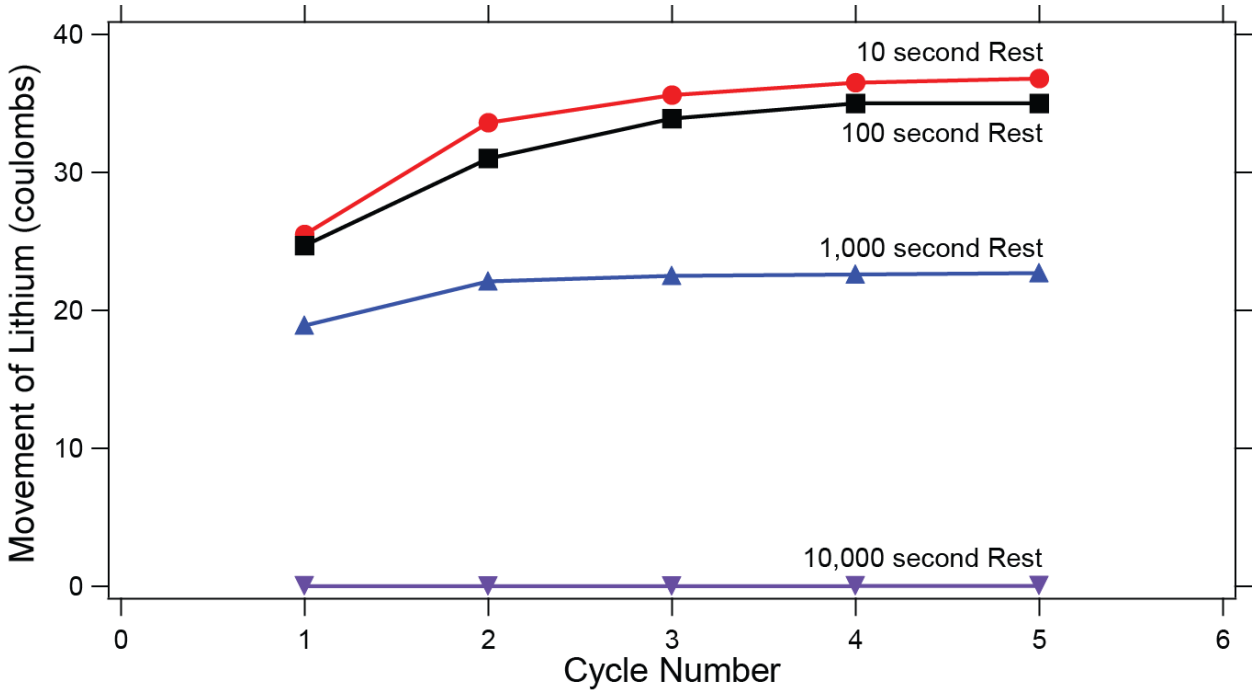

Figure 2.13. Cycling at a C/2 rate with varying rests to a 10% DoD measured after resting and immediately before the subsequent cycle. The slope of the OCP is the 'Sloped OCP' function seen in Figure 2.3a.

2.2f Uneven Charge/Discharge Rates

As we saw in the previous Subsections, both the C-rate and the time of the rest period play an important role in determining both the magnitude of the movement of lithium during cycling and how quickly the movement reaches steady state. In this Subsection we look at the combination of these two effects.

Throughout the previous sections the simulations were run with symmetric charge and discharge profiles. That is, the rate and time of discharge was exactly the same as the rate and time of charge. In this Subsection we look at what happens if the total time of cycling remains constant, but the rate of charge increases. For example, in Figure 2.14, the 'C/5 Symmetric, 100 second Rest' line refers to a C/5 discharge rate and a C/5 charge rate to a 10 percent depth of discharge with 100 second rests following the discharges and charges. This means that the discharges and charges periods take 1800 seconds, making the total time for one cycle 3800

seconds. We then compare this to the 'C/5 Discharge 100 second Rest, C/1 Charge 1540 second Rest' line in Figure 2.14. Here, we discharge the cell at a C/5 rate for 1800 seconds and rest for 100 seconds, but now we charge the cell at a C/1 rate. This charge period only takes 360 seconds to complete; therefore the rest after charging is extended from 100 seconds, to 1540 seconds thereby making the time to complete one cycle 3800 seconds. By comparing these two lines, we can understand whether, if given a certain amount of time to charge the cell, it is better to charge the cell quickly and rest for a longer period of time or charge the cell slowly and rest for a short period of time.

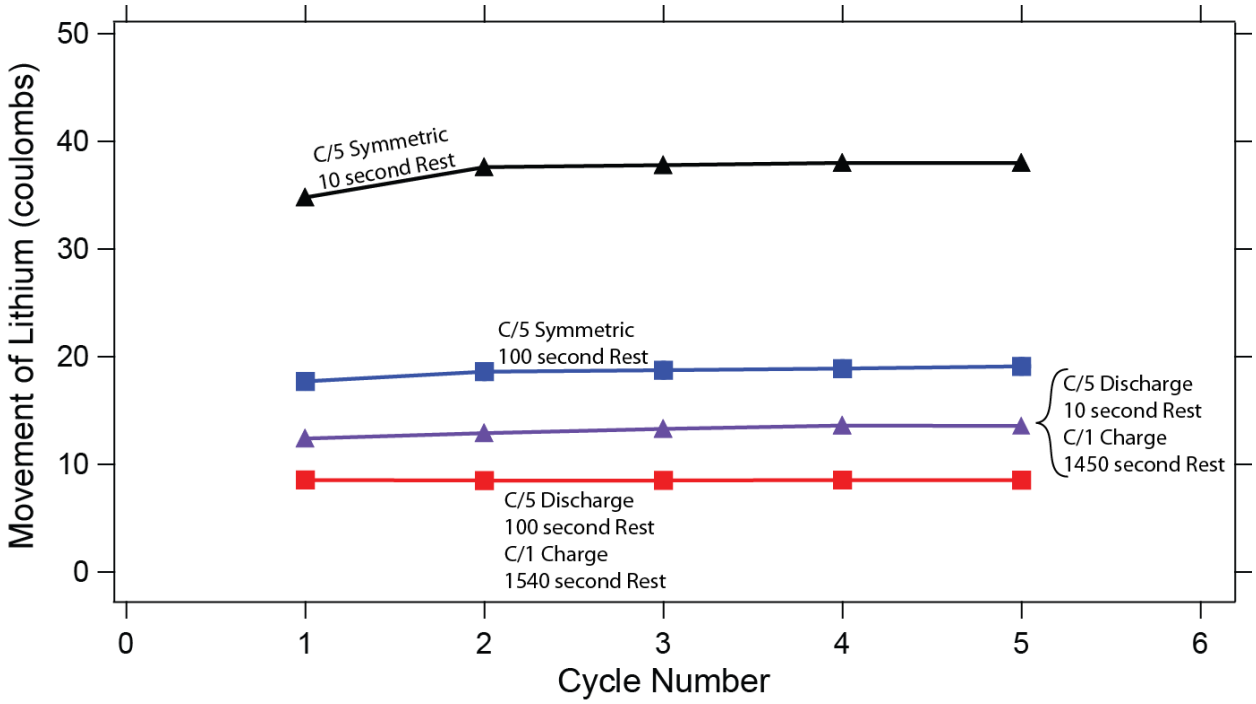

Figure 2.14. Cycling at various rates with varying rests to a 10% DoD measured after resting and immediately before the subsequent cycle. The slope of the OCP is the 'Sloped OCP' function seen in Figure 2.3a.

From Figure 2.14 above, when comparing the symmetric lines to their counterpart asymmetric lines, with everything else equal, it is more favorable, at least in relation to the movement of lithium after resting, to charge the cell quickly and let it rest for longer than charge the cell slowly with a shorter rest. Of course, Figure 2.14 only takes into account the movement of the lithium after the rest following charging and not the maximum movement of the lithium, which is at the end of charging and is much higher, for a C/1 charge than a C/5 charge. Furthermore, if given large amounts of time to complete the charge, then the movement seen after a full cycle will be very similar for both a slow or fast charge. For example, a C/5 symmetric cycle with 10,000 second rests will show similar movement after each

complete cycle to an asymmetric case with a C/1 charge and rest period of 11440 seconds. This is because the rest period is so long in either case that the lithium has become nearly uniform and any further rest will show only minimal changes.

2.3 Conclusions

In this chapter, the two-dimensional model presented in Chapter 1, which is able to capture the movement of lithium during cycling, was run for multiple cycles. This model still incorporates electrode tabbing, a moving boundary at the negative electrode, a CoO_2 intercalation electrode as the cathode, and a lithium-metal negative electrode. The positive electrode is modeled using porous electrode theory, the separator as a liquid electrolyte with a binary salt, and the total volume changes are assumed to be zero. Finally, the negative electrode in this model is twice the thickness required by stoichiometry in order to avoid the need for a separate negative current collector.

The model was cycled at various rates, depths of discharge, and lengths of the rest. From this, we saw that, with a large excess of lithium at the negative electrode, the movement of the lithium will reach a quasi-steady state where the movement during each subsequent cycle will remain at the same magnitude. The rate at which the movement of the lithium reaches that steady state depends on the slope of the open-circuit-potential function, the rate of discharge and charge, the depth of discharge, and the length of time that the cell is allowed to rest both after the discharge and charge phase. First, as was described in Subsection 2.2a, the slope of the open-circuit-potential function strongly affects both the magnitude of the movement of lithium seen during cycling and the rate at which a steady state is reached. A more steeply sloped open-circuit-potential function will cause less movement of lithium during cycling, and a steady state will be reached more quickly than with a flatter open-circuit-potential function. Then, in Subsection 2.2b, we relaxed the assumption that there is a large excess of lithium in the negative electrode and looked at the case where 80 percent of the negative electrode was utilized. This was achieved by reducing the thickness of the negative electrode from 50 to 15 μm with the result that the pinching of the negative electrode is another nonlinearity that leads to a progression of the movement of lithium over multiple cycles. In Subsection 2.2c, we returned to a 50 μm thick negative electrode and discussed the effect of the discharge/charge rate. Here we saw that increasing the C-rate both increased the magnitude of the movement of lithium during cycling and delayed the steady state seen in Subsection 2.2a. In Subsection 2.2d, we explored the effect that the depth of discharge has on the movement of lithium during cycling, and in Subsection 2.2e, the effects of the rest periods. Finally, in Subsection 2.2f, we compared the magnitude of the effect of the C-rate with that of the rest periods and found that the lithium was more uniform if the cell was charged quickly

and allowed to rest for longer and was less uniform if the cell was charged slowly with a limited rest period following charging.

The major assumption in this chapter was that the separator, while inhibiting dendrites, also allows the lithium to move unhindered. However, in order to inhibit dendrites either a stiff polymer separator or a ceramic protective layer is needed. In Chapter 3 we see how the incorporation of a stiff polymer separator will affect the movement of the lithium seen both in this chapter and in Chapter 1. Then, in Chapter 4, we look into the use of a ceramic to inhibit dendrites and calculate the stresses in a ceramic protective layer due to bending.

Chapter 3

Mechanical Deformation of a Lithium-Metal Anode due to a Very Stiff Separator

3.1 Introduction

In Chapters 1 and 2 we created a two-dimensional model to capture the movement of lithium during cycling. This model uses a finite-element method and incorporates electrode tabbing, transport using concentrated-solution theory, Butler-Volmer reaction kinetics, and the net movement of the lithium electrode during cycling. The model was cycled at various rates with the result that, even without dendrites, significant large-scale movement of lithium was seen both during each half cycle and after a full cycle of a discharge followed by a charge. More specifically, the lithium was depleted more near the negative tab, yet after a full cycle, there was a net migration of the lithium towards the negative tab. This migration was found to be caused by three separate phenomena. First, as was described in Section 1.3a, the geometry strongly affects the current density distribution which directly correlates to the asymmetric depletion of lithium during the discharge phase. The second driving force, discussed in Section 1.3b, was the open-circuit-potential function, the slope of which not only affects the magnitude of the movement, but also is the largest nonlinearity that contributes to the movement of lithium after a full cycle. The third and smallest contributor to the movement of the lithium is the concentration gradients in the liquid electrolyte, which was detailed in Section 1.3c. In this section, we saw that, when the OCP is flat and the concentration gradients are reduced by increasing the diffusivity, the lithium will return to its starting position after a full cycle.

The model developed in Chapter 1 was extended, in Chapter 2, to multiple cycles at various rates, depths of discharge, and lengths of the rest. From this, we saw that, with significant excess lithium, the movement of the lithium reaches a quasi-steady state where the movement during each subsequent cycle is the same as during the previous cycle. The rate at which the movement of the lithium reaches a steady state depends on the slope of the open-circuit-potential function, the rate of discharge and charge, the depth of discharge, and the length of time that the cell is allowed to rest. First, as was described in Section 2.2a, the slope of the open-circuit-potential function strongly affects both the magnitude of the movement of lithium seen during cycling and the rate at which a steady state is reached. A more steeply

sloped open-circuit-potential function causes less movement of lithium during cycling, and a steady state will be reached more quickly than with a flatter open-circuit-potential function. In Section 2.2b we explored cases with high lithium utilization and saw that the lithium becomes progressively thinner on the left edge of the cell during extended cycling. While this nonlinearity is a small one, it nonetheless contributes toward the continued movement of lithium during cycling.

In Section 2.2c, we discussed the effect of the discharge/charge rate. Here we saw that increasing the C-rate increased the magnitude of the movement of lithium during cycling. In Section 2.2d, we explored the effect that the depth of discharge has on the movement of lithium during cycling, and in Section 2.2e, the effects of the rest periods were explored. Finally, in Section 2.2f, we compared the magnitude of the effect of the C-rate with that of the rest periods and found that the lithium was more uniform if the cell was charged quickly and allowed to rest for longer and was less uniform if the cell was charged slowly with a limited rest period following charging.

In both Chapters 1 and 2, the major assumption was that the separator, while inhibiting dendrites, also allowed the lithium to move unhindered. This, of course is not physical as lithium which is allowed to move freely forms dendrites during the charge phase. The propagation of dendrites, which is the primary mechanism for failure in lithium-metal batteries,[1-3] can be inhibited through the incorporation of a polymer separator with acceptable ionic conductivity that has a shear modulus about twice that that of lithium.[1, 4-7]

Such a separator resists the movement of lithium seen in Chapters 1 and 2 through the generation of stresses in the cell. As can be imagined, as the lithium moves, the separator is either compressed or stretched. This translates into stresses in the separator and lithium that affect the negative electrode through two mechanisms: altering the thermodynamics of the negative electrode and deforming the negative electrode mechanically. Both of these mechanisms are treated in this chapter. The effect of the stress on the thermodynamics is developed in Section 3.5 along with the elastic deformation of the negative electrode. Then, in Section 3.7, the plastic deformation of the lithium negative electrode is included.

Before discussing the results of modeling a lithium-metal battery with a very stiff separator, it is necessary to gain a solid background in mechanics. Therefore, in Sections 3.2 through 3.4, the mechanical behavior of materials is discussed starting from the definition of stress and strain in Section 3.2, continuing on to elastic deformation in Section 3.3, and finishing on plastic deformation in Section 3.4. In Section 3.6, we look at Limit Analysis, which gives us a first look at what we expect the plastic deformation to look like and the range of stresses under which deformation should be expected to occur. Finally, in Section 3.7, we develop and discuss the full numerical analysis of plastic deformation in a lithium-metal negative electrode.

3.2 Stress and Strain

The following sections concern themselves with the mechanical behavior of materials, which refers to the response of materials to forces. This response, called deformation, can take several different forms including elastic, plastic, or viscoelastic. When a material deforms under small stresses, the deformation may be elastic. In this case, when the stress is removed, the material will revert to its original shape, and the deformation is considered reversible. The physical process involved is a simple stretching of atomic bonds by changing the distance between the atoms and, when the stress is removed, the elastic deformation will recover immediately. In this chapter, and in most continuum-mechanics text books for that matter, it is assumed that the material deforms much more quickly than the rate at which the load is applies, or, conversely, the stress in the material is equilibrated much faster than the rate of deformation. This assumption is typically valid for ductile materials and leads to a quasi-steady state. There may be, however, some time-dependent shape recovery called viscoelasticity which is not covered in this chapter.

Larger stresses may cause plastic deformation, which is defined as irreversible or permanent deformation. After a material undergoes plastic deformation, it will not revert to its original shape when the stress is removed. The physical process of plastic deformation involves the sliding of atoms past each other, permanently changing their relative positions.

In this section we define both stress and strain to provide a basis of understanding on which our later treatment of elastic and plastic deformation of a lithium-metal anode is built. There are several key areas of understanding which are treated in this section. In Section 3.2a we begin with the definition of stress and introduce the reader to the stress tensor and the notation used throughout the remainder of this chapter. Within this section, the concept of principal stress is described as well as the invariants of the stress tensor. We then introduce the concept of the stress deviator tensor which includes the off-diagonal components of the stress tensor. From this concept, we can define a new set of stress invariants based on the stress deviator called the *deviatoric stress invariants*. These invariants are used in plasticity to determine whether the stress in a body is sufficient to cause plastic deformation. This determination is called *yield criteria* and is treated in Section 3.4b.

In Section 3.2b, we define infinitesimal strain, the principal strain, and the strain invariants. Then, in Section 3.2c, we explore the uniaxial tension test, which is commonly used to describe the response of a material to stress. Finally, in Section 3.2d, we generalize the uniaxial loading to multiaxial loading. All the material from this section is built from references 8 through 11, which can be found in the references section.

3.2a Stress

The stress on a material is defined as the intensity of a force at a point or

$$\sigma = \lim_{A \to 0} \frac{F}{A}. \qquad 3.1$$

Because the stresses involve both forces and areas, they are tensor quantities. Nine components of stress are needed to describe fully a state of stress at a point, as shown in Figure 3.1. A normal stress (compressive or tensile) is one in which the force is perpendicular to the area on which it acts, and a shear stress describes a force that is parallel to the area on which it acts. For example, σ_{zz} describes a force in the z-direction acting on a plane perpendicular to the z axis, and σ_{zy} describes a force in the y-direction acting on a plane perpendicular to the z-direction. Thus, σ_{zz} is a normal force, and σ_{zy} is a shear force.

In Figure 3.1, the faces from which the positive axes are extended are taken to be the positive faces; the other faces, lying on the planes, are taken to be the negative faces. By Newton's third law, the forces acting on the positive faces (shown) are counteracted by opposing forces acting on the negative faces are in the negative (x, y, z) directions.

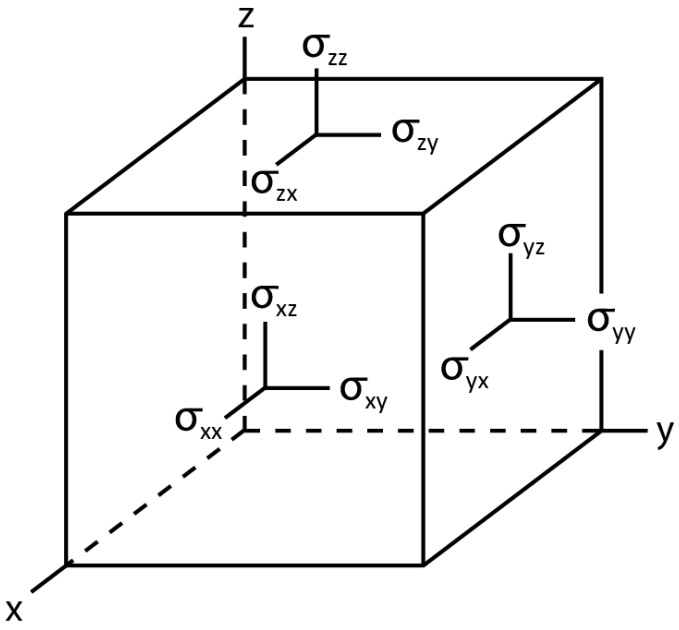

Figure 3.1. Representation of the components of the second-order stress tensor $\underline{\underline{\sigma}}$ acting on the positive faces of a body in the Cartesian coordinate system

In mechanics, it is common to denote the x, y, and z coordinates as x_1, x_2, and x_3; thus, for much of this chapter, we refer to them as such. In keeping with this notation, we redo Figure 3.1 to include the typical coordinate notation (see Figure 3.2).

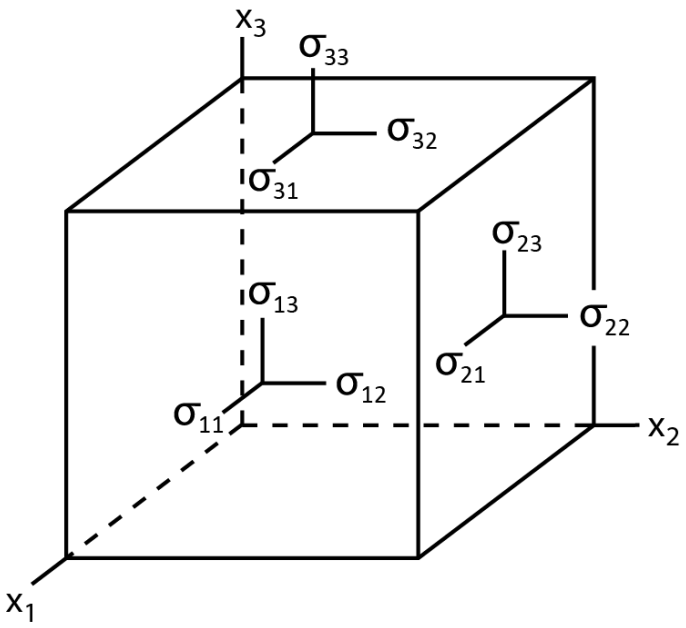

Figure 3.2. Representation of the components of the second-order stress tensor $\underline{\underline{\sigma}}$ acting on the positive faces of a body in the Cartesian coordinate system using the typical notation of x_1, x_2, and x_3 instead of the Cartesian x, y, and z coordinates.

In tensor notation, the state of stress is expressed as

$$\underline{\underline{\sigma}} = \begin{bmatrix} \sigma_{11} & \sigma_{12} & \sigma_{13} \\ \sigma_{21} & \sigma_{22} & \sigma_{23} \\ \sigma_{31} & \sigma_{32} & \sigma_{33} \end{bmatrix}. \qquad 3.2$$

It is also somewhat common to denote normal stresses simply as σ_i and shear stresses as τ_{ij}. This, however, can lead to some confusion with the principal stresses also notated as σ_i; thus σ_{ij}, as described in Equation 3.2, will be used to denote all stresses.

It may be useful here to note that pairs of shear stresses with reversed subscripts are always equal ($\sigma_{ij} = \sigma_{ji}$). If they were not, then a force balance on an infinitesimal element would result in an infinite rotational acceleration. This can be seen from Figure 3.3, where, if $\sigma_{12} \neq \sigma_{21}$ then the element has a net rotational force (torque) on it and undergoes an infinite rotational acceleration. This can be proven through performing a torque balance on a two-dimensional element and equating it to the moment of inertia times the angular acceleration.

Through this analysis, it is seen that the net torque is proportional to δ^2, while the moment of inertia is proportional to δ^4, where δ is the length of a side.

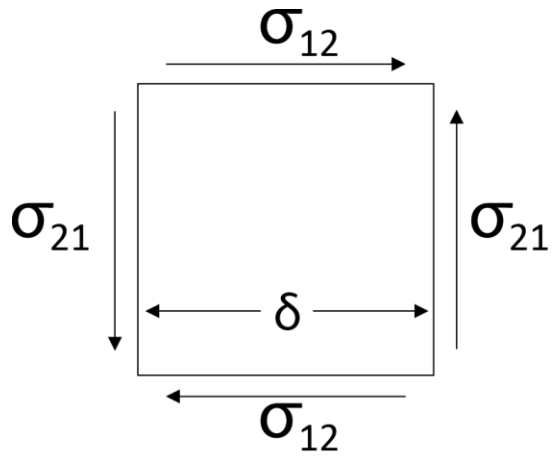

Figure 3.3. An infinitesimal element with a shear stress applied showing that pairs of shear stresses with reversed subscripts must be equal for the element to avoid infinite angular acceleration.

Therefore, the stress may be written in its symmetric form

$$\underline{\underline{\sigma}} = \begin{bmatrix} \sigma_{11} & \sigma_{12} & \sigma_{13} \\ \sigma_{12} & \sigma_{22} & \sigma_{23} \\ \sigma_{13} & \sigma_{23} & \sigma_{33} \end{bmatrix}. \tag{3.3}$$

This stress tensor is often referred to as a Cauchy stress tensor and given the notation $\underline{\underline{T}}$, though in this chapter we simply use the tensor $\underline{\underline{\sigma}}$.

Principal Stresses

Regardless of the state of stress, at a given point, there exist three mutually perpendicular planes on which the shear stresses vanish. The remaining (normal) components on these three planes are called the *principal stresses* and are denoted as σ_1, σ_2, and σ_3. Correspondingly, the three planes are called principal planes, and the three mutually perpendicular axes that are normal to the three planes are called principal axes. Thus, by definition, principal stresses are directed along principal axes that are perpendicular to the principal planes. This is equivalent to denoting the symmetric tensor $\underline{\underline{\sigma}}$ by rotation of the coordinates. As a side note, all symmetric matrices are diagonalizable; more generally, any real normal matrix, where $\underline{\underline{A}}^{\mathrm{T}}\underline{\underline{A}} = \underline{\underline{A}}\underline{\underline{A}}^{\mathrm{T}}$, is also diagonalizable.

Stress Invariants

Every second rank tensor (such as the stress and strain tensor) has three independent invariant quantities associated with it. For the stress tensor, the first invariant is simply the trace of the stress tensor or

$$I_1 = \mathrm{tr}(\underline{\underline{\sigma}}) = \sigma_{11} + \sigma_{22} + \sigma_{33}. \tag{3.4}$$

While the second invariant of the stress tensor is $\underline{\underline{\sigma}} : \underline{\underline{\sigma}}$,[36] in mechanics it is stated in a somewhat more confusing manner as a combination of the first and second invariant of the stress tensor.[9-12, 19, 20, 38] In keeping with the mechanics literature we define the second invariant as

$$\begin{aligned} I_2 &= \frac{1}{2}(\underline{\underline{\sigma}} : \underline{\underline{\sigma}} - I_1^2) \\ &= -\sigma_{11}\sigma_{22} - \sigma_{22}\sigma_{33} - \sigma_{33}\sigma_{11} + \sigma_{12}^2 + \sigma_{23}^2 + \sigma_{31}^2. \end{aligned} \tag{3.5}$$

Finally, the third invariant of the stress tensor is the determinant, or

$$I_3 = \det(\underline{\underline{\sigma}}) = \sigma_{11}\sigma_{22}\sigma_{33} + 2\sigma_{12}\sigma_{23}\sigma_{31} - \sigma_{12}^2\sigma_{33} - \sigma_{23}^2\sigma_{11} - \sigma_{31}^2\sigma_{22}. \tag{3.6}$$

I_1, I_2, and I_3, given by Equations 3.4, 3.5, and 3.6, are invariants of stress and must have the same magnitudes for all choices of coordinate axes. For a more detailed derivation of the principal stresses and stress invariants, please see Section 2.4.2 and 2.4.3 in *Advanced Mechanics of Materials*.[12]

Stress Deviator

Let us now break the stress tensor down into the mean normal stress or mean hydrostatic stress tensor $p\underline{\underline{\mathrm{I}}}$ (where $p = I_1/3$) and the stress deviator tensor $\underline{\underline{S}}$. This leads to

$$\underline{\underline{\sigma}} = \underline{\underline{S}} + p\underline{\underline{\mathrm{I}}} \tag{3.7}$$

or

$$\underline{\underline{S}} = \underline{\underline{\sigma}} - p\underline{\underline{\mathrm{I}}} \tag{3.8}$$

The mean normal stress tensor differs from the thermodynamic pressure because its components (σ_{11}, σ_{22}, and σ_{33}) do not have to be equal. Therefore, even if we rotate our

coordinate system such that only the normal components remain, the stress deviator tensor is not necessarily zero.

Deviatoric Stress Invariants

Now that we have split the stress tensor into its hydrostatic and deviatoric components, let us determine the three stress invariants of the stress deviator. Again, the first deviatoric stress invariant is simply the trace of the stress deviator, or

$$J_1 = \mathrm{tr}(\underline{\underline{S}}) = 0. \tag{3.9}$$

The second invariant of the stress deviator is defined in mechanics as $1/2\ (\underline{\underline{S}} : \underline{\underline{S}} - J_1^2)$. However, because the first invariant of the stress deviator is zero, the second invariant can be written as

$$J_2 = \frac{1}{2}\underline{\underline{S}} : \underline{\underline{S}} = \frac{1}{3}I_1^2 + I_2$$

or

$$J_2 = \frac{1}{6}[(\sigma_{11} - \sigma_{22})^2 + (\sigma_{22} - \sigma_{33})^2 + (\sigma_{33} - \sigma_{11})^2] + \sigma_{12}^2 + \sigma_{23}^2 + \sigma_{31}^2. \tag{3.10}$$

The third deviatoric stress invariant is, again, the determinant of the stress deviator tensor, or

$$J_3 = \det(\underline{\underline{S}}). \tag{3.11}$$

It should be noted here that the deviatoric stress invariants can be put in terms of the stress invariants seen in the previous Subsection. They are stated here simply because they have historically been used in mechanics to describe stresses causing plastic flow. As we see later in this chapter, the second deviatoric stress invariant is used in both the von Mises yield criterion and to define the equivalent stress.

3.2b Strain

In continuum mechanics it is useful to describe a change in the shape of a material relative to its initial shape or reference state. This reference state, also called the undeformed state, corresponds to the shape of a stationary material. If a stress is applied to the material it deforms meaning that its shape changes and all the particles within the material move. From

this deformation, we define $\underline{u}$ (the displacement vector) which gives the distance and direction that a point in the solid has moved from its initial position as a result of the applied stress.

From this definition, we construct the symmetric infinitesimal strain tensor $\underline{\underline{\epsilon}}$ from the displacement gradient $\nabla\underline{u}$ as

$$\underline{\underline{\epsilon}} = \frac{1}{2}\left[\nabla\underline{u} + (\nabla\underline{u})^{T}\right] \tag{3.12}$$

where the quantity of one-half is arbitrary, and makes the results of this analysis consistent with the well-known linear elastic theory when material displacements are small.

We can also define the deformation-rate tensor $\underline{\underline{\dot{\epsilon}}}$ as simply

$$\underline{\underline{\dot{\epsilon}}} = \frac{1}{2}\left[\nabla\underline{v} + (\nabla\underline{v})^{T}\right] \tag{3.13}$$

where $\underline{\underline{\dot{\epsilon}}} = d\underline{\underline{\epsilon}}/dt$.[36-38]

Principal Strains and Strain Invariants

Similar to the stress tensor, we can diagonalize the infinitesimal strain tensor $\underline{\underline{\epsilon}}$ to get the principal strains, which we denote as ϵ_1, ϵ_2, and ϵ_3. Furthermore, the strain tensor also has three invariants, the first of which is the trace of the strain tensor, or

$$\bar{I}_1 = \mathrm{tr}(\underline{\underline{\epsilon}}) = \epsilon_{11} + \epsilon_{22} + \epsilon_{33}. \tag{3.14}$$

The second invariant is defined, in mechanics, as the double dot product of the strain tensor with itself minus the square of the first strain invariant. In keeping with the mechanics literature we define the second invariant of the strain tensor as

$$\begin{aligned}\bar{I}_2 &= \frac{1}{2}(\underline{\underline{\epsilon}} : \underline{\underline{\epsilon}} - \bar{I}_1^2) \\ &= -\epsilon_{11}\epsilon_{22} - \epsilon_{22}\epsilon_{33} - \epsilon_{33}\epsilon_{11} + \epsilon_{12}^2 + \epsilon_{23}^2 + \epsilon_{31}^2.\end{aligned} \tag{3.15}$$

Finally, the third invariant of the strain tensor is the determinant, or

$$\bar{I}_3 = \det(\underline{\underline{\epsilon}}) = \epsilon_{11}\epsilon_{22}\epsilon_{33} + 2\epsilon_{12}\epsilon_{23}\epsilon_{31} - \epsilon_{12}^2\epsilon_{33} - \epsilon_{23}^2\epsilon_{11} - \epsilon_{31}^2\epsilon_{22}. \tag{3.16}$$

Strain Deviator and the Deviatoric Strain Invariants

Similar to our treatment of stress in Section 3.2a, let us now break the strain tensor down into the mean-normal strain $\bar{I}_1/3$ and the strain deviator ϵ'_{ij}. This leads to

$$\underline{\underline{\epsilon}} = \underline{\underline{\epsilon}}' + \frac{1}{3}\mathrm{tr}(\underline{\underline{\epsilon}})\underline{\underline{I}}. \tag{3.17}$$

The strain deviator is useful in describing the equivalent strain. However, when a material is assumed to be incompressible the strain is equal to the strain deviator ($\mathrm{tr}(\underline{\underline{\epsilon}}) = 0$).

The first deviatoric strain invariant is simply the trace of the strain deviator, or

$$\bar{J}_1 = \mathrm{tr}(\underline{\underline{\epsilon}}') = 0. \tag{3.18}$$

The second invariant of the strain deviator is $1/2\left(\underline{\underline{\epsilon}}' : \underline{\underline{\epsilon}}' - \bar{J}_1^2\right)$. However, because the first invariant of the strain deviator is zero, the second invariant can be written as

$$\bar{J}_2 = \frac{1}{2}\underline{\underline{\epsilon}}' : \underline{\underline{\epsilon}}' = \frac{1}{3}\bar{I}_1^2 + \bar{I}_2 \tag{3.19}$$

or

$$\bar{J}_2 = \frac{1}{6}[(\epsilon_{11} - \epsilon_{22})^2 + (\epsilon_{22} - \epsilon_{33})^2 + (\epsilon_{33} - \epsilon_{11})^2] + \epsilon_{12}^2 + \epsilon_{23}^2 + \epsilon_{31}^2.$$

The third deviatoric strain invariant is, again, the determinant of the strain deviator tensor, or

$$\bar{J}_3 = \det(\underline{\underline{\epsilon}}'). \tag{3.20}$$

It should be noted here that the deviatoric strain and the deviatoric strain invariants are simply mathematical creations which have been used historically in mechanics to help to describe plastic flow. The deviatoric strain invariants can be put in terms of the strain invariants seen in the previous Subsection. As we see later in this chapter, the second deviatoric strain invariant is used to define the equivalent strain and is used in the hardening parameter found in the Levy-Mises and Prandtl-Reuss equations describing plastic flow. However, in both the Levy-Mises and Prandtl-Reuss equations, plastic incompressibility (meaning that $\mathrm{tr}(\underline{\underline{\epsilon}}) = 0$) is assumed making the strain tensor and the deviatoric strain tensor equal. This makes the definition of deviatoric strain and the deviatoric strain invariants somewhat pointless. It is, however, included here in order to aid the reader in matching the equations derived in the mechanics literature with the equations derived in this thesis.

3.2c The Uniaxial Tension Test

The most common test for determining the properties of a solid material is the uniaxial tension test. From this, the tensile data can be used to predict a material's behavior for both elastic and plastic deformation under forms of loading other than uniaxial tension. Its importance cannot be overstated as it is used to obtain the material properties (elastic modulus, yield stress, and material hardening properties) around which the equations for both elastic and plastic deformation are built.

In a typical test, the specimen is gripped from each end and stretched at a constant rate until failure. The force required to elongate the material is plotted against the increase in length of the specimen relative to its starting length to create a stress-strain curve (Figure 3.4 below). The first part of the curve, up to point A, defines the region of elastic deformation. The part from point A to B defines the region of stable plastic deformation, point B to C is the region where necking occurs, and point C represents the point of failure of the material.

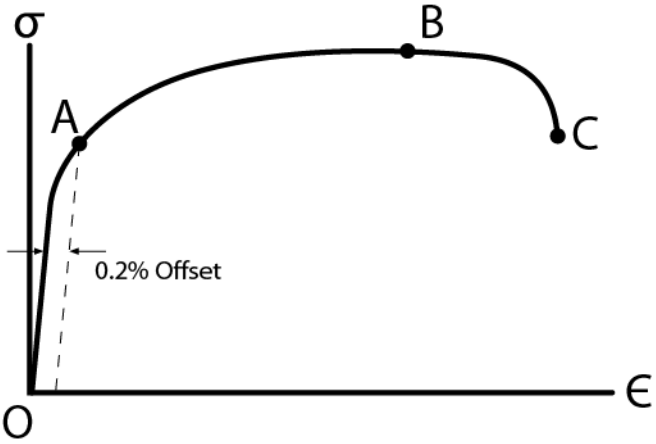

Figure 3.4 Stress σ versus strain ϵ for a uniaxial tension test on a typical ductile material. The Line OA represents the elastic region; point A represents the 0.2% offset yield strength; AB encloses the region of stabile plastic deformation; B is the ultimate tensile strength of the material, BC is the unstable plastic region, and point C represents the point of failure of the material.

It is tempting to define an elastic limit as the stress right before the first plastic deformation occurs or to define it as the first departure from linearity. Neither definition, however, is very useful because they both depend on how accurately strain is measured.[11] To avoid this problem, the onset of plasticity is usually described by an offset yield strength (point A in Figure 3.4 This is found by constructing a straight line parallel to the initial linear portion of the stress-strain curve, but offset from it by $\epsilon = 0.002$ or 0.2% (the dashed line in Figure 3.4). The offset yield strength is then defined as the stress at the intersection between the stress-

strain curve and the offset line (point A in Figure 3.4). The rationale is that if a material had been loaded to this stress and then unloaded, the unloading path would have been along this offset line, resulting in a plastic strain of $\epsilon = 0.002$ or 0.2%. The advantage of this way of defining yielding is that it is easily reproduced and provides a standard around which materials can be tested and compared.

The region between point A and point B in Figure 3.4 constitutes the region of stable plastic deformation. This region is considered stable because each subsequent infinitesimal strain requires a greater stress to cause it. This is defined as strain hardening with a more complete definition in Section 3.4a.

Point B represents the ultimate tensile strength or ultimate strength of the specimen. It is defined as the highest value of the stress and is the point of transition from stable to unstable plastic deformation. To explain this further, as long as the stress-strain curve rises, the deformation occurs uniformly. For a ductile material, the stress will reach a maximum well before fracture. At this maximum (point B), the deformation localizes, forming a neck where the local thickness is smaller than the average thickness. Local thinning continues to occur at the neck until it becomes so severe that fracture occurs at point C.

3.2d Multiaxial Loading

The stress-strain test presented in Section 3.2c is given in terms of the normal stress and the normal strain. Such a representation was possible since only uniaxial loading was considered. However, in many applications of engineering materials, the loading is multiaxial. It is then useful to be able to determine relations for a material under multiaxial loading without having to test the material under every possible loading condition.

In order to achieve this, we generalize uniaxial stress-strain to a multiaxial stress-strain by using the equivalent (or effective) stress, $\bar{\sigma}$, and the equivalent strain $\bar{\epsilon}$. The equivalent stress is related to the second deviatoric stress invariant through

$$\begin{aligned}\bar{\sigma} &= (3J_2)^{\frac{1}{2}} \\ &= \left\{\frac{1}{2}\left[(\sigma_{11}-\sigma_{22})^2+(\sigma_{22}-\sigma_{33})^2+(\sigma_{33}-\sigma_{11})^2\right]\right. \\ &\qquad \left.+3(\sigma_{12}^2+\sigma_{23}^2+\sigma_{31}^2)\right\}^{\frac{1}{2}}\end{aligned} \tag{3.21}$$

or

$$\bar{\sigma} = \left(\frac{3}{2}\underline{\underline{S}} : \underline{\underline{S}}\right)^{\frac{1}{2}}. \tag{3.22}$$

The equivalent strain is defined similarly as

$$\bar{\epsilon} = \frac{2}{3}(3\bar{J}_2)^{\frac{1}{2}}$$

$$= \frac{2}{3}\left\{\frac{1}{2}[(\epsilon_{11}-\epsilon_{22})^2 + (\epsilon_{22}-\epsilon_{33})^2 + (\epsilon_{33}-\epsilon_{11})^2] + 3(\epsilon_{12}^2+\epsilon_{23}^2+\epsilon_{31}^2)\right\}^{\frac{1}{2}} \quad 3.23$$

or

$$\bar{\epsilon} = \frac{2}{3}\left(\frac{3}{2}\underline{\underline{\epsilon}}' : \underline{\underline{\epsilon}}'\right)^{\frac{1}{2}}. \quad 3.24$$

The 2/3 is inserted into the definition of equivalent strain so that the equivalent strain $\bar{\epsilon}$ becomes the uniaxial strain ϵ_{11}(where ϵ_{11} is the only non zero element of $\underline{\underline{\epsilon}}$) under uniaxial loading for incompressible materials.

It has been shown experimentally that uniaxial data (such as in Figure 3.4) can be used to represent the stress-strain relationship under multiaxial loading by simply substituting the equivalent stress and the equivalent strain for the uniaxial stress and uniaxial strain. In fact, when equivalent stress-strain tests are plotted together with uniaxial stress-strain tests, the data show good agreement and tend to fall within the bounds of the normal experimental scatter.[8]

With the definitions of equivalent stress and equivalent strain, we can take our uniaxial stress-strain curve (such as Figure 3.4) and generalize it to multiaxial loading by simply changing the axes from stress and strain to equivalent stress and equivalent strain such as in Figure 3.5 below. As is seen in Sections 3.4c and 3.7a, the multiaxial stress-strain plot is used in plasticity theory to describe the strain hardening properties of the material under multiaxial strain (or multiaxial stress).

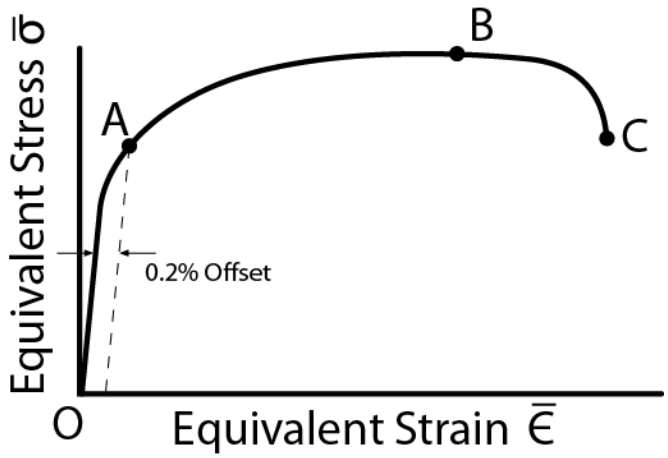

Figure 3.5 A uniaxial tension test on a typical ductile material (from Figure 3.4) generalized to multiaxial loading through the use of equivalent stress $\bar{\sigma}$ and equivalent strain $\bar{\epsilon}$. The Line OA represents the elastic region; point A represents the 0.2% offset yield strength; AB encloses the region of stabile plastic deformation; B is the ultimate tensile strength of the material, BC is the unstable plastic region, and point C represents the point of failure of the material.

3.3 Elasticity and Elastic Behavior of Metals

Small mechanical loads cause elastic deformation. The mechanics for elastic deformation of a crystalline solid, which most metals are, is a stretching of the bonds between atoms due to the applied load. Since there is no long-range movement of the atoms, elastic deformation is recoverable and, when the applied load is removed, the atoms return to their original equilibrium positions.

Since the configuration of the atoms changes with direction in a crystal, the elastic response of a crystal depends on the direction of the load. However, the crystalline materials that are ordinarily used are bulk materials and are typically polycrystalline metals whose elastic properties average those of the individual grains and are, hence, nearly isotropic. Because of this, these materials require only two elastic moduli to describe their behavior. These are typically the Young's modulus or elastic modulus E and Poisson's ratio ν, but also include the shear modulus G and the bulk modulus K which, for isotropic systems, are functions of E and ν.

In this section we first define, in Section 3.3a, the elastic modulus and Poisson's ratio. Then, in Section 3.3b, we use these definitions to describe the equations for elasticity or the general statement of Hooke's law. The equations developed in this section and in Section 3.3c specifically, are used throughout this chapter to relate the elastic stress to the elastic strain.

3.3a The Elastic Modulus and Poisson's Ratio

If we look at the stress-strain curve found from a uniaxial-tension test, such as the one in Figure 3.4, we can see that the curve is linear for very small strains. Because, the specimen is in uniaxial tension, only one component of the stress is present (let us make this the x-direction in this example) and thus, all other stress components are zero (i.e., $\sigma_{22} = \sigma_{33} = \sigma_{12} = \sigma_{23} = \sigma_{13} = 0$). This leads us to take the ratio of the stress to the strain as the slope of the linear portion, and we define this ratio as E, the Young's or elastic modulus, which is a property of the material.

Although uniaxial tension causes stress in only one direction, the strains are in the lateral direction as well as in the direction of the stress. For example, a bar stretched along its length will lengthen, but will also become thinner, reducing in diameter. Different materials, of course, behave differently. A completely incompressible material, for example, maintains its volume throughout deformation. A perfectly elastic material, on the other hand, elongates during uniaxial tension, but maintains its diameter, increasing in volume as it stretches. The ratio between the transverse deformation and axial deformation is called the Poisson's ratio, ν, which is defined for uniaxial tension in the x_1 direction as

$$\nu = -\frac{d\epsilon_{\text{transverse}}}{d\epsilon_{\text{axial}}} = \frac{d\epsilon_{22}}{d\epsilon_{11}} = \frac{d\epsilon_{33}}{d\epsilon_{11}}. \qquad 3.25$$

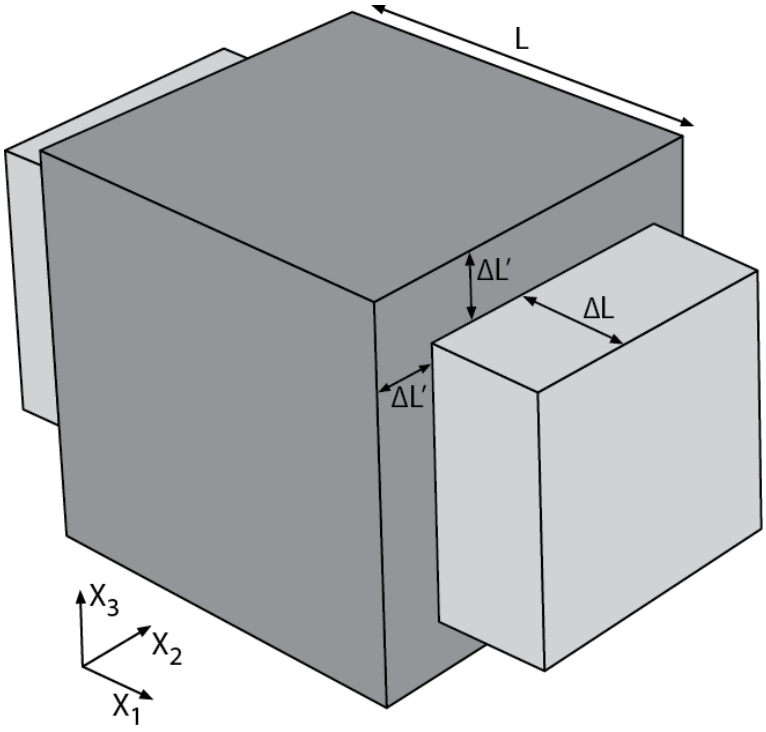

Figure 3.6. An undeformed cube of material (dark grey) with dimensions L, stretched to a length of L+ΔL (light grey). Due to Poisson's ratio, the stretched material will contract in the transverse direction by ΔL'.

To explain this in another way, let us take a cube stretched in the x_1 direction (such as in Figure 3.6). The length increase of the cube is ΔL in the x_1 direction, and has a length decrease of ΔL' in the x_2 and x_3 directions; the infinitesimal diagonal strains are given by

$$d\epsilon_{11} = \frac{dx_1}{x_1}, \qquad d\epsilon_{22} = \frac{dx_2}{x_2}, \qquad d\epsilon_{33} = \frac{dx_3}{x_3}. \tag{3.26}$$

Integrating these expressions and using the definition of Poisson's ratio gives

$$-\nu \int_L^{L+\Delta L} \frac{dx_1}{x_1} = \int_L^{L-\Delta L'} \frac{dx_2}{x_2} = \int_L^{L-\Delta L'} \frac{dx_3}{x_3}. \tag{3.27}$$

Solving this gives us

$$\left(1 + \frac{\Delta L}{L}\right)^{-\nu} = 1 - \frac{\Delta L'}{L}. \tag{3.28}$$

For very small values of ΔL, we can approximate ν as

$$\nu \approx \frac{\Delta L^{'}}{\Delta L} \quad \text{or} \quad \nu \approx -\frac{\epsilon_{22}}{\epsilon_{11}} = -\frac{\epsilon_{33}}{\epsilon_{11}}. \tag{3.29}$$

Most materials have Poisson's ratio values ranging between 0.0 and 0.5. A perfectly incompressible material deformed elastically at small strains has a Poisson's ratio of exactly 0.5, and a spring, or perfectly elastic material, has a Poisson's ratio of 0 meaning that it does not contract in directions transverse to stretching. Most steels and rigid polymers exhibit values of about 0.3.

3.3b Equations for Elasticity: Generalized Hooke's Law

Let us suppose that stresses are applied to a material in all directions. If we assume that the rate of deformation is slow enough, then we can assume a quasi-steady state. We can then simplify the equation of motion to

$$-\nabla \cdot \underline{\underline{\sigma}} = 0. \tag{3.30}$$

So long as the strains are small enough, the strain can be found by summing the strain increments due to each of the stresses. Thus:

$$\begin{aligned}
\epsilon_{11} &= \frac{1}{E}[\sigma_{11} - \nu(\sigma_{22} + \sigma_{33})], \\
\epsilon_{22} &= \frac{1}{E}[\sigma_{22} - \nu(\sigma_{11} + \sigma_{33})], \\
\epsilon_{33} &= \frac{1}{E}[\sigma_{33} - \nu(\sigma_{11} + \sigma_{22})], \\
\epsilon_{12} &= \frac{1+\nu}{E}\sigma_{12}, \\
\epsilon_{13} &= \frac{1+\nu}{E}\sigma_{13},
\end{aligned} \tag{3.31}$$

and

$$\epsilon_{23} = \frac{1+\nu}{E}\sigma_{23}.$$

Or, in matrix notation

$$\underline{\underline{\epsilon}} = \frac{1}{E}\{\underline{\underline{\sigma}} - \nu[\mathrm{tr}(\underline{\underline{\sigma}})\underline{\underline{I}} - \underline{\underline{\sigma}}]\}$$

or

$$\underline{\underline{\epsilon}} = \frac{1-\nu}{E}\underline{\underline{\sigma}} - \frac{\mathrm{tr}(\underline{\underline{\sigma}})}{E}\underline{\underline{I}}, \qquad 3.32$$

where $\mathrm{tr}(\underline{\underline{\sigma}})$ signifies the trace of the stress matrix or $\sigma_{11} + \sigma_{22} + \sigma_{33}$.

Inversion of Equation 3.32 gives us

$$\underline{\underline{\sigma}} = \frac{E\nu}{(1+\nu)(1-2\nu)}\mathrm{tr}(\underline{\underline{\epsilon}})\underline{\underline{I}} + \frac{E}{(1+\nu)}\underline{\underline{\epsilon}} \qquad 3.33$$

where, again, $\mathrm{tr}(\underline{\underline{\epsilon}})$ signifies the trace of the strain matrix and $\underline{\underline{I}}$ is the identity matrix. We call Equation 3.33 the general statement of Hooke's law. Notice that this equation relates one symmetric matrix ($\underline{\underline{\sigma}}$) to another ($\underline{\underline{\epsilon}}$) in a linear manner with coefficients which are functions of the invariants and other scalars. This is true in plasticity except that the coefficients can be nonlinear functions of the scalar invariants.

3.4 Plasticity and Plastic Behavior

In the previous sections we describe stress and strain and have become acquainted with the uniaxial tension test and its resulting stress-strain curve (Figure 3.4). As previously stated, deformation is typically split into two different regimes: elastic deformation and plastic deformation. Because we assume a quasi-steady state, elastic deformation occurs as soon as any load is applied and increases linearly with an increasing stress. We defined elastic deformation in Section 3.3 as a reversible deformation where the crystal structure of the material is maintained and the mechanism for deformation is through the stretching of the bonds between the atoms within the crystal.

Plastic deformation, however, is considered to be irreversible or permanent deformation and takes place at stresses higher than the yield stress of the material. The mechanism for plastic deformation is called *Dislocation Theory* (a more detailed discussion of dislocation theory can be found in Section A.1 of Appendix A) and involves one layer of atoms slipping over an adjacent layer. Such a shift can occur whenever the shear stress on a plane reaches a critical value and is accounted for through a *Yield Criterion.* (A more detailed discussion of yield criteria can be found in Section 3.4b) Because the equilibrium position of the atoms is changed, plastic deformation is considered irreversible and path- or history-dependent.

To explain the difference between elastic and plastic deformation in a physical way, let us conduct a simple test. If one were to bend a paperclip slightly and let go, the paperclip would spring back to its original position (elastic deformation). If, however, more force is applied to the bending of the paperclip, and it is bent substantially, when the force is removed, it will spring back slightly (the elastic component of the deformation), but most of the bending, or deformation, will remain (the plastic component of the deformation). This concept leads to the common assumption that the strain tensor in the plastic regime may be decomposed into its elastic and plastic components.

Because of this path dependence, we start this section by idealizing the stress-strain curve in Section 3.4a. We then explore further the path-dependent nature of plasticity and its relationship to the stress-strain curve through an example of a material stressed above its yield point, resulting in a progression of the yield point. Section 3.4b explains two different yield criteria used in plastic deformation. In Section 3.4c we begin to describe the mathematical treatment of plastic deformation and the assumption made to simplify these equations. The equations developed in this section are used to describe numerically the plastic deformation of lithium metal treated in Section 3.7. Finally, in Section 3.4d we develop an analytical solution to a simplified plasticity problem to give the reader an understanding of how the equations developed thus far are used in practice.

3.4a Idealization of the Stress-Strain Curve

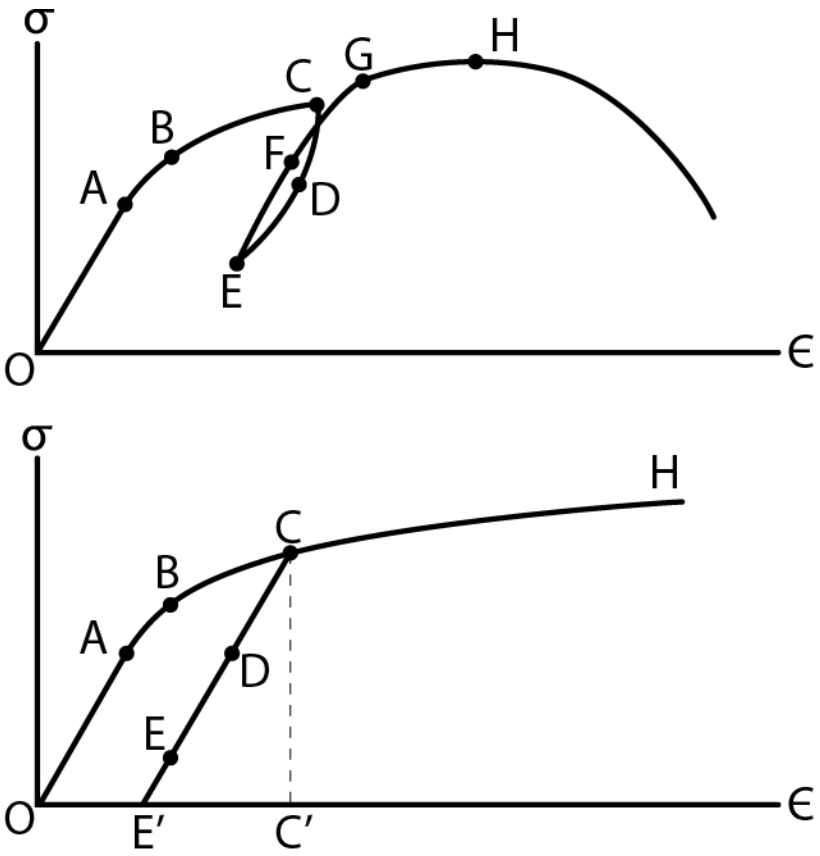

Figure 3.7. (a) An example of a representative stress-strain diagram in uniaxial tension, and (b) its idealization.

The stress-strain diagram of a representative elastic-plastic material in uniaxial tension is shown in Figure 3.7a. The stress σ is a monotonically increasing function of the strain ϵ from O to H, after which it falls off until fracture occurs. From the origin, O, to the proportional limit A (where the stress-strain curve deviates from linearity), the material is linearly elastic and, since the deformation is reversible, unloading takes place along AO. However, as was explained in Section 3.2c, the elastic range generally extends beyond A to the offset yield strength, B. For loading above B, the deformation is irreversible so that unloading from a point C to zero stress would leave a permanent plastic strain. Reloading from a point such as E proceeds along EF to subsequent yielding at G, where further loading proceeds along the path GH. The portion of the plot from B to H is called strain or work hardening for the reason that as the strain increases, the material become harder i.e., a higher stress is required to deform the material further.

The portion of the stress-strain curve from H onwards is called strain softening for the same reason. As the strain continues, the material becomes softer and less stress is required to

deform the material further. Since, in this chapter, attention is focused on the work-hardening range of the stress-strain curve, the portion after H is ignored.

In general, the stress-strain curve in Figure 3.7a is influenced by time effects such as creep and strain rate as well as temperature. Prandtl,[13] following experimental work, assumed isothermal deformation and ignored time effects, thereby idealizing the stress-strain curve to that shown in Figure 3.7b. To be a bit more precise, Prandtl[13] followed the assumptions that, in Figure 3.7a: (a) the slope of EFG at E is taken to be the same as the slope at O; (b) the hysteresis loop is assumed to be determined by the point E; and (c) the reloading path is assumed to pass through C and proceeds thereafter from C to H, as if unloading had never occurred. These assumptions are taken to imply that the hysteresis loss is zero, so that the path CDE coincides with GFE. Furthermore, the proportional limit A is assumed to coincide with the yield limit at B and unloading paths such as along CE are straight lines parallel to OA. This leads to the idealized curve seen in Figure 3.7b where the points A, B, C, D, and E line up with those in Figure 3.7a.

As stated previously, the plastic deformation process is history- or path-dependent. In other words, there will not be a one-to-one correspondence between stress and strain during plastic deformation. For example, in Figure 3.7b, points A and D have the same stress level but different strains. On the other hand, the strains at points B and E are the same, but the stresses are different.

In order to explore the idealized stress-strain curve further, let us say that we have a material that follows an idealized stress-strain curve such as in Figure 3.7b. As we load the material, it deforms elastically until the yield limit is reached at point B. At this point, further loading of the material causes plastic deformation to occur. When point C is reached, we cease loading the material and begin unloading it. The stresses are relaxed, and the material follows the path CDE until the material is fully unloaded and point E' is reached. Since plastic deformation is irreversible, the material still retains some deformation even when no stress is applied, as is evident by the location of E'. Let us now start to load the material again. Since plasticity is path dependent, as we begin to load the material a second time, we start to deform it elastically following the path E'ED. Eventually we load the material enough such that it reaches the new yield limit at point C. This second yield limit is higher than the initial yield limit for the unworked material, and this phenomenon is called strain hardening or work hardening. The increase in the yield point of the material is due to the accumulation of dislocations during plastic deformation thereby changing the property of the material.[12]

Yield Surface

Let us now generalize the increase in the yield point of the material beyond the uniaxial case seen in Figure 3.7b to multiaxial loading. The concept of the yield point from the uniaxial

tension test now becomes a yield surface signifying that yielding can be achieved from any combination of stresses, not just uniaxial.

To illustrate this phenomenon, we consider, as an example, a material loaded first with the normal stress σ_{xx} only. As we increase σ_{xx} while keeping all the other stresses zero, the specimen deforms elastically until the stress reaches point B on the initial yield surface shown in Figure 3.8. If the stress is increased to point C in Figure 3.8, then the specimen deforms plastically, and the yield surface expands to become the subsequent yield surface in Figure 3.8. The subsequent yield surface in Figure 3.8 now constitutes the new yield surface for the specimen, and any stress below this level causes only elastic deformation. As is discussed in the Dislocation Theory Section in Appendix A, this expansion of the yield surface is caused by an increase in the dislocation density.

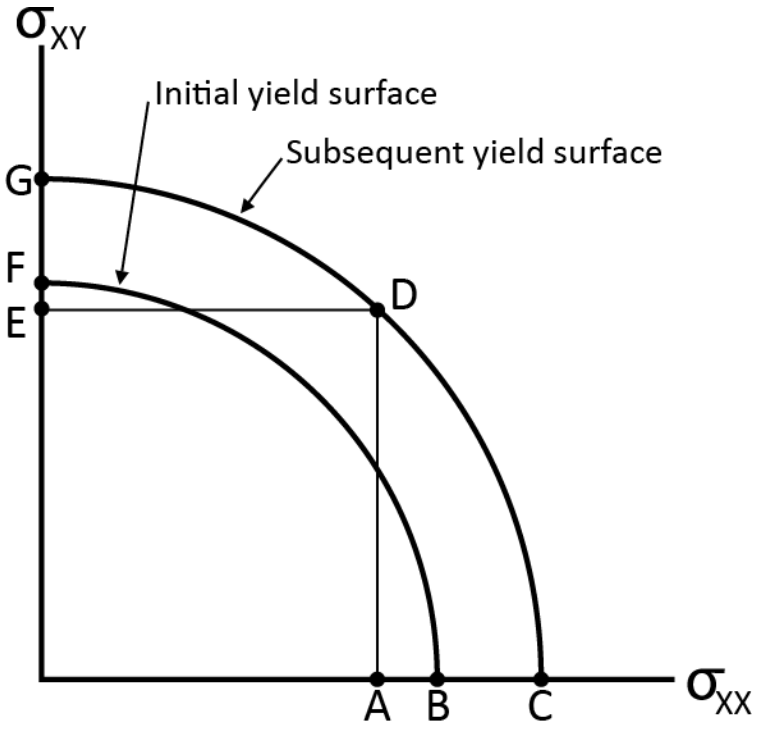

Figure 3.8 A representation of the history dependence of plastic deformation through the expansion of the yield surface. The initial yield surface represents some strain path which leads to the yield point of the material (any point along the 'Initial yield surface' curve) and the subsequent yield surface is the expansion of the yield surface (from an accumulation in the dislocations) due to further strain beyond the initial yield strength. The axes here are two normal stresses σ_{xx} and σ_{yy}.

Now we unload the material from point C to point A, keep the normal stress σ_{xx} constant, and apply a normal stress σ_{yy} until point D is reached on the subsequent yield surface. During this process, following the path CAD, the material behaves elastically because

the path is inside the current yield surface. Therefore, no further plastic deformation occurs when the stress state of the specimen changes from C to D following CAD.

Now let us consider another loading history. Let a new specimen be loaded along the σ_{yy} axis. The elastic deformation continues until the initial yielding at point F. The stress σ_{yy} increases until point G on the subsequent yield surface, which also contained points C and D from the previous loading program. The specimen in then unloaded from point G to E, and the normal stress σ_{yy} is kept constant while the normal stress σ_{xx} is applied and increased to bring the stress state of the specimen to point D. Since the path GED is inside the current yield surface, the material deforms elastically, and no additional plastic deformation occurs.

3.4b Yield Criteria

There are two major yield criteria that are commonly used to describe the yielding of materials. The simplest yield criterion is one first proposed by Tresca. In terms of the principal stresses, the Tresca yield criterion states that plastic deformation occurs when the maximum difference between two principal stresses reaches a critical value κ which is the shear yield stress. Mathematically, this is expressed as

$$\frac{1}{2}\max(|\sigma_1 - \sigma_2|, |\sigma_2 - \sigma_3|, |\sigma_3 - \sigma_1|) = \kappa \qquad 3.34$$

where κ is the shear yield stress and σ_1, σ_2, and σ_3 are the principal stresses.

The second criterion, called the von Mises yield criterion, is related to the Tresca yield criterion but is somewhat more complicated. However, experiments have shown (a number of relevant references are listed in reference 14) that test points generally fall closer to the von Mises yield criterion than to Tresca's.

The von Mises yield criterion assumes that plastic yielding occurs only when the second invariant of the deviatoric stress tensor, J_2, reaches a critical value κ^2, which is the square of the shear yield stress.

$$J_2 - \kappa^2 = 0 \quad \text{for yielding or plastic deformation} \qquad 3.35$$

$$J_2 < \kappa^2 \qquad \text{for elastic deformation} \qquad 3.36$$

From Equation 3.10 (the definition of J_2), in terms of stress components, the yield criterion takes the form:

$$J_2 = \frac{1}{6}[(\sigma_{11} - \sigma_{22})^2 + (\sigma_{22} - \sigma_{33})^2 + (\sigma_{33} - \sigma_{11})^2] + \sigma_{12}^2 + \sigma_{23}^2 + \sigma_{31}^2 = \kappa^2 \quad (3.37)$$

or, in terms of the principal stresses:

$$J_2 = \frac{1}{6}[(\sigma_1 - \sigma_2)^2 + (\sigma_2 - \sigma_3)^2 + (\sigma_3 - \sigma_1)^2] = \kappa^2. \quad (3.38)$$

To relate the shear yield strength κ to the tensile yield strength, σ_Y, we conduct a simple tension test:

$$\sigma_{11} = \sigma_Y \quad (3.39)$$

and all other stresses equal zero, where σ_Y is the yield stress in simple tension. Substituting Equation 3.39 into Equation 3.37 gives

$$\frac{1}{3}\sigma_Y{}^2 = \kappa^2. \quad (3.40)$$

Therefore

$$\kappa = \frac{\sigma_Y}{\sqrt{3}}. \quad (3.41)$$

If we rewrite Equation 3.38 in terms of the tensile yield stress, σ_Y, we can say that yielding occurs when the equivalent stress $\bar{\sigma}$ (defined by Equation 3.21), is equal to the yield stress. Mathematically, this leads to yielding occurring when

$$\sigma_Y = \bar{\sigma} = \left\{\frac{1}{2}[(\sigma_1 - \sigma_2)^2 + (\sigma_2 - \sigma_3)^2 + (\sigma_3 - \sigma_1)^2]\right\}^{1/2} \quad (3.42)$$

or, in full component form,

$$\sigma_Y = \bar{\sigma} = \left\{\frac{1}{2}[(\sigma_{11} - \sigma_{22})^2 + (\sigma_{22} - \sigma_{33})^2 + (\sigma_{33} - \sigma_{11})^2] + 3(\sigma_{12}^2 + \sigma_{23}^2 + \sigma_{31}^2)\right\}^{\frac{1}{2}}. \quad (3.43)$$

While experimental test points generally fall closer to the Mises yield criterion than to Tresca's, the Tresca yield criterion is simpler and never deviates from the Mises yield condition by more than 15%.

3.4c Plasticity

In this section we develop the constitutive equations for plastic deformation that are used in Section 3.7 to determine the deformation of lithium metal with a very stiff separator. Plastic deformation is a very complicated phenomenon with different materials each having a unique behavior. It is very difficult to determine generalized equations that can govern all materials; thus we make several assumptions to simplify the problem and limit ourselves to a select group of materials: ductile, isotropic crystalline materials such as mild steel, copper, or, in our case, lithium. In this section we first describe the assumptions commonly made to simplify plastic deformation. We then state the equations typically used in engineering to relate the stress to the plastic strain. Finally, we describe in detail how the equations for plastic deformation can be derived from Newton's law of viscosity for a non-Newtonian fluid.

Assumptions

Before we develop the constitutive equations for plastic deformation, let us first take a moment to discuss the assumptions that are commonly made in order to simplify plastic deformation.

1) Time independent plasticity

We have already significantly simplified plasticity by limiting ourselves to ductile, isotropic crystalline materials. However, a further simplification is the common assumption of time-independent or rate-independent plasticity.[8,9,11,12,19-22] This assumption is typically valid unless the metal has a unique crystal structure or the strain rates are particularly fast (above 10^{-1}/s to 10^{-2}/s).[21] The justification for this approximation is typically found through a uniaxial-tension test. This test is performed for a given material under a variety of strain rates and, if the tensile stress-strain curves measured at room temperature are changed by only a few percent when the strain rate is changed by an order of magnitude or more (for example from 10^{-4}/s to 10^{-3}/s), then the rate-independent-assumption can be made. This assumption holds true for most structural metals.

2) Plastic incompressibility

The second assumption commonly made is that of plastic incompressibility or, during plastic deformation, Poisson's ration is 0.5. This means that $\mathrm{tr}(\underline{\underline{\epsilon}}) = 0$ (or $\nabla \cdot \underline{v} = 0$) and the deviatoric strain, defined as

$$\underline{\underline{\epsilon}} = \underline{\underline{\epsilon}}' + \frac{1}{3}\mathrm{tr}(\underline{\underline{\epsilon}})\underline{\underline{I}}, \tag{3.17}$$

is equal to the strain, (or $\underline{\underline{\epsilon}} = \underline{\underline{\epsilon}}'$).

3) Simplification of the equation of motion

A further simplification is applied to the equation of motion:

$$\rho\frac{D\underline{v}}{Dt} = -\nabla \cdot \underline{\underline{\sigma}} + \rho\underline{g}. \tag{3.44}$$

where ρ is the density (assumed to be constant), D/Dt is the substantial derivative, $\rho\underline{g}$ is the gravitational term, and the stress is a function of the strain. Here we assume that the inertial terms on the left and the gravitational term on the right are zero leaving us with

$$\nabla \cdot \underline{\underline{\sigma}} = 0. \tag{3.45}$$

4) Decomposition of the strain tensor

The final assumption is that the strain tensor can be decomposed into its elastic and plastic components. We can then we can simplify the equations by treating the elastic deformation and plastic deformation separately and can then combine these deformations back into a total deformation through the equation

$$\underline{\underline{\epsilon}} = \underline{\underline{\epsilon}}^{e} + \underline{\underline{\epsilon}}^{p}, \tag{3.46}$$

where $\underline{\underline{\epsilon}}^{e}$ is the elastic component of the strain tensor and $\underline{\underline{\epsilon}}^{p}$ is the plastic component of the strain tensor.

Constitutive Equations

As a starting point for our discussion, we begin with Newton's law of viscosity

$$\underline{\underline{\tau}} = -\mu\left[\nabla\underline{v} + (\nabla\underline{v})^{T}\right] + \left(\frac{2}{3}\mu - \tilde{\kappa}\right)(\nabla\cdot\underline{v})\underline{\underline{I}} \qquad 3.47$$

where μ is the viscosity, $\tilde{\kappa}$ is the dilatational viscosity (notated with a tilde to distinguish it from the shear yield strength κ) and $\underline{v}$ is the velocity of the particles in the material.[36] Here $\underline{\underline{\tau}}$ is given by

$$\underline{\underline{\tau}} = \underline{\underline{\sigma}} - p\underline{\underline{I}} \qquad 3.48$$

where $\underline{\underline{\sigma}}$ is the total stress tensor and p is the thermodynamic pressure. Following from assumption 2 the term on the right of Equation 3.47 is zero such that Equation 3.47 becomes

$$\underline{\underline{\tau}} = -\mu\left[\nabla\underline{v} + (\nabla\underline{v})^{T}\right] = -2\mu\underline{\underline{\dot{\epsilon}}}. \qquad 3.49$$

The factor of 2 comes into Equation 3.49 due to the factor of 1/2 in the definition of strain.

Let us now subtract the hydrostatic stress tensor $p\underline{\underline{I}}$ from the stress tensor ($\underline{\underline{S}} = \underline{\underline{\sigma}} - p\underline{\underline{I}}$) rather than the thermodynamic pressure. This leaves us with

$$\underline{\underline{S}} = -2\mu\underline{\underline{\dot{\epsilon}}}. \qquad 3.50$$

The Levy-Mises theory of plasticity[18] replaces the viscosity -2μ by

$$\frac{1}{\dot{\lambda}} = \frac{\kappa}{\sqrt{\dot{\bar{J}}_2}} \qquad 3.51$$

where $\dot{\lambda} = d\lambda/dt$ and λ is generically called a "hardening parameter." Here, κ is the shear yield stress, and $\dot{\bar{J}}_2$ is rate of the second invariant of the deviatoric strain or, since we assume plastic incompressibility, $\dot{\bar{J}}_2 = 1/2\,(\underline{\underline{\dot{\epsilon}}} : \underline{\underline{\dot{\epsilon}}})$. (A more detailed derivation of the Levy-Mises equation can be found in the next Subsection) The theory also neglects the elastic component of the strain stating that $\underline{\underline{\epsilon}} = \underline{\underline{\epsilon}}^{p}$. We now have

$$\underline{\underline{S}} = \frac{1}{\dot{\lambda}}\underline{\underline{\dot{\epsilon}}} = \frac{\kappa}{\sqrt{\frac{1}{2}(\underline{\underline{\dot{\epsilon}}} : \underline{\underline{\dot{\epsilon}}})}}\underline{\underline{\dot{\epsilon}}}. \qquad 3.52$$

From the Yield Criteria Section (Section 3.4b), we can relate the shear yield stress κ to the tensile yield stress σ_Y through Equation 3.41:

$$\kappa = \frac{\sigma_Y}{\sqrt{3}}. \tag{3.41}$$

Substituting Equation 3.41 into Equation 3.52 gives

$$\underline{\underline{S}} = \frac{\sigma_Y}{\sqrt{\frac{3}{2}(\dot{\underline{\underline{\epsilon}}} : \dot{\underline{\underline{\epsilon}}})}} \dot{\underline{\underline{\epsilon}}}. \tag{3.53}$$

Since, during yielding, $\sigma_Y = \bar{\sigma} = \sqrt{3/2\,(\underline{\underline{S}} : \underline{\underline{S}})}$ we have (from Equations 3.22 and 3.24):

$$\underline{\underline{S}} = \frac{\sqrt{\frac{3}{2}(\underline{\underline{S}} : \underline{\underline{S}})}}{\sqrt{\frac{3}{2}(\dot{\underline{\underline{\epsilon}}} : \dot{\underline{\underline{\epsilon}}})}} \dot{\underline{\underline{\epsilon}}} = \sqrt{\frac{\underline{\underline{S}} : \underline{\underline{S}}}{\dot{\underline{\underline{\epsilon}}} : \dot{\underline{\underline{\epsilon}}}}} \dot{\underline{\underline{\epsilon}}}. \tag{3.54}$$

The hardening parameter (which is a function of the invariants) in front of the rate of deformation tensor is determined through the multiaxial stress-strain curve (Figure 3.5) which we created from our uniaxial tension test (Figure 3.4) by using the equivalent stress and equivalent strain.

For the problem of plastic deformation of a lithium-metal anode, we would like to include both elastic and plastic deformation of the lithium metal in our calculation. Therefore we use include a superscript p on the strain tensor to denote that we are only looking at the plastic component of the tensor. Since we are assuming time-independent plasticity, we can cancel out dt from Equation 3.52 giving us

$$\underline{\underline{S}} = \frac{1}{d\lambda} d\underline{\underline{\epsilon}}^p = \sqrt{\frac{\underline{\underline{S}} : \underline{\underline{S}}}{d\underline{\underline{\epsilon}}^p : d\underline{\underline{\epsilon}}^p}}\, d\underline{\underline{\epsilon}}^p \tag{3.55}$$

where $d\underline{\underline{\epsilon}}^p$ is the increment of the plastic strain. From Equations 3.22 and 3.24, we can relate the scalar factor to the equivalent stress $\bar{\sigma}$ and the increment of the plastic component of the equivalent strain $d\bar{\epsilon}^p$ given by

$$d\bar{\epsilon}^p = \frac{2}{3}\left(\frac{3}{2} d\underline{\underline{\epsilon}}^p : d\underline{\underline{\epsilon}}^p\right)^{\frac{1}{2}} \tag{3.56}$$

assuming plastic incompressibility. We now have

$$\underline{\underline{S}} = \frac{2}{3}\frac{\bar{\sigma}}{d\bar{\epsilon}^p}\dot{\underline{\underline{\epsilon}}} \tag{3.57}$$

We can then calculate the elastic component of the strain through Hooke's law.

Solving Equation 3.57 for $d\underline{\underline{\epsilon}}^p$ leads to the Prandtl-Reuss equations which, in expanded form, are

$$\begin{aligned}
d\epsilon_{11}^p &= \frac{d\bar{\epsilon}^p}{\sigma_Y}\left[\sigma_{11} - \frac{1}{2}(\sigma_{22}+\sigma_{33})\right],\\
d\epsilon_{22}^p &= \frac{d\bar{\epsilon}^p}{\sigma_Y}\left[\sigma_{22} - \frac{1}{2}(\sigma_{11}+\sigma_{33})\right],\\
d\epsilon_{33}^p &= \frac{d\bar{\epsilon}^p}{\sigma_Y}\left[\sigma_{33} - \frac{1}{2}(\sigma_{11}+\sigma_{22})\right],\\
d\epsilon_{12}^p &= \frac{3d\bar{\epsilon}^p}{\sigma_Y}\sigma_{12},\\
d\epsilon_{23}^p &= \frac{3d\bar{\epsilon}^p}{\sigma_Y}\sigma_{23},
\end{aligned} \tag{3.58}$$

and

$$d\epsilon_{13}^p = \frac{3d\bar{\epsilon}^p}{\sigma_Y}\sigma_{13}.$$

It should be noted here that the Prandtl-Reuss equations can include the tensile yield strength as a function of the equivalent plastic strain ($\sigma_Y(\bar{\epsilon}^p)$) to include the work-hardening behavior of lithium metal.

The Transition from Rate-Dependent to Rate-Independent Plasticity

Let us now take a moment to relate the constitutive equations for plastic flow to those developed for Newtonian and non-Newtonian fluids. For all cases, the constitutive equation can be expressed as

$$\underline{\underline{\sigma}} = -\eta\left[\nabla\underline{v} + (\nabla\underline{v})^T\right] + K\underline{\underline{I}}, \tag{3.59}$$

where η and K are scalar funtions of relevant properties including the temperature, pressure, and composition of the material, as well as the scalar invariants of the tensor $\nabla\underline{v}$.

For a Newtonian fluid, ηand K are chosen so that

$$\underline{\underline{\sigma}} = -\mu\left[\nabla\underline{v} + (\nabla\underline{v})^{T}\right] + \left(\frac{2}{3}\mu - \tilde{\kappa}\right)\underline{\underline{I}}\,\nabla\cdot\underline{v} + p\underline{\underline{I}}, \tag{3.60}$$

where μ and $\tilde{\kappa}$ are physical properties ($\tilde{\kappa}$ is the dilatation viscosity notated with a tilde to distinguish it from κ, the shear yield strength), and p is the thermodynamic pressure of the local fluid element.

For plastic flow, we still use Equation 3.59 choosing η and K such that the stress is related to the rate of deformation $\underline{\underline{\dot{\epsilon}}}$ through

$$\underline{\underline{\dot{\epsilon}}} = \frac{1}{2\eta}\langle 1 - \frac{\kappa}{\sqrt{J_2}}\rangle\,\underline{\underline{S}} \tag{3.61}$$

where $\underline{\underline{S}} = \underline{\underline{\sigma}} - p\underline{\underline{I}}$, p is the hydrostatic pressure, κ is the shear yield strength, J_2 is the second invariant of the stress deviator (defined in Equation 3.10), and η is a function of $\underline{\underline{\dot{\epsilon}}} : \underline{\underline{\dot{\epsilon}}}$.[20] In Equation 3.61, the brackets are defined such that:

$$\langle x\rangle = \begin{cases} 0, & \text{if } x \le 0 \text{ and} \\ x, & \text{if } x \ge 0 \end{cases} \tag{3.62}$$

We can relate Equation 3.61 to the multiaxial stress-strain curve (seen in Figure 3.5 or Figure 3.9 below) through Equation 3.21

$$\bar{\sigma} = \sqrt{3J_2} \tag{3.21}$$

and Equation 3.41

$$\kappa = \frac{\sigma_Y}{\sqrt{3}}. \tag{3.41}$$

Equation 3.61 can now be described as

$$\underline{\underline{\dot{\epsilon}}} = \frac{1}{2\eta}\langle 1 - \frac{\sigma_Y}{\bar{\sigma}}\rangle\,\underline{\underline{S}} \tag{3.63}$$

where $\overline{\sigma}$ is the equivalent stress and σ_Y is the tensile yield strength. We can now imagine the stress-strain plot (such as the one in Figure 3.9 below) as a steady-state line. If the equivalent stress $\overline{\sigma}$ is at or below the current yield stress σ_Y then yielding does not occur. However, if we increase the stress to above the yield stress, we are above the stress-strain curve and the material deforms.

To explain this relation further, let us conduct a simple loading program on an example material whose stress-strain data is given by Figure 3.9. First, we stress the material elastically until it reaches the 0.2% offset yield strength at point A. So far the material has only deformed elastically, the equivalent stress is equal to the yield stress, and $1 - \sigma_Y/\overline{\sigma} = 0$ in Equation 3.63. Now, we suddenly increase the stress on the material to point B in Figure 3.9. The equivalent stress at point B is greater than the yield strength and, if we maintain the applied stress, the material deforms until point C is reached where the yield strength now equals the equivalent stress and the rate of deformation goes to zero. Next, we suddenly increase the stress from point C to point D and hold the stress steady, allowing the material to deform until point E is reached where the equivalent stress again equals the new yield strength of the material. In order to get the strain for each step we must integrate over time. To calculate the total strain for a multi-step loading process, such as the one described previously, we sum the strain for each step to get the total strain for the loading program.

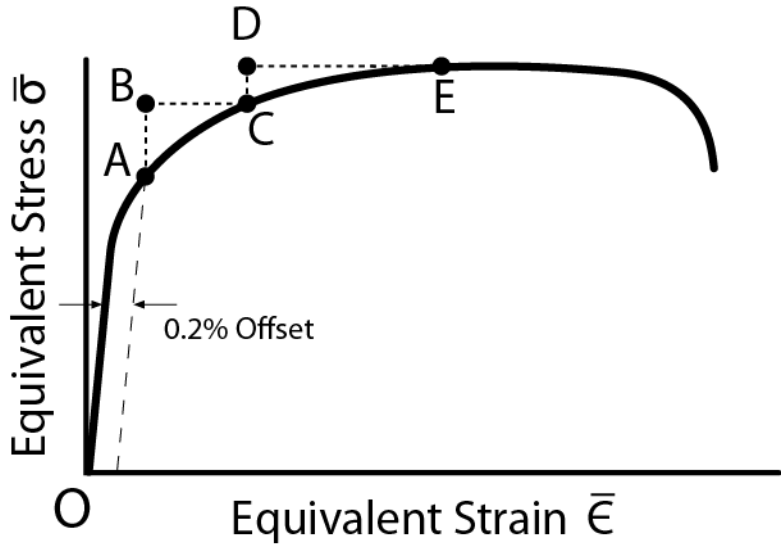

Figure 3.9. Equivalent stress versus equivalent strain for an example material at a very low rate of strain such that the solid line can be thought of as steady state. Point A represents the 0.2% yield stress and point C and E, equilibrium points where the stress equals the yield stress and the stress can be maintained without further deformation occurring. Points B and D represent points away from equilibrium where the stress exceeds the yield stress of the material and deformation occurs.

In the previous example, steps ABC and CDE are rather large. Decreasing the step size is equivalent to a slower and slower process such that eventually the process is very slow and the loading program follows the steady-state line. In terms of Equation 3.63, $(1 - \sigma_Y/\overline{\sigma}) \rightarrow 0^+$. We can now make the assumption that the process is independent of time. This means that the process is slow enough that, by changing the rate at which we stress the material (or, equivalently, the rate at which we strain the material), we do not deviate appreciably from the steady-state stress-strain curve. To implement the time-independent assumption into Equation 3.63 let us perform some algebra.

In this analysis we assume that we are in the plastic region of deformation and are slightly above the steady-state line meaning that $1 - \sigma_Y/\overline{\sigma}$ is small but positive. Taking the double dot product $\underline{\underline{\dot{\epsilon}}} : \underline{\underline{\dot{\epsilon}}}$ of Equation 3.61 yields

$$\eta\sqrt{2(\underline{\underline{\dot{\epsilon}}} : \underline{\underline{\dot{\epsilon}}})} = \sqrt{J_2} - \kappa. \tag{3.64}$$

(The algebra leading from Equation 3.61 to 3.64 can be found in Section A.5 of Appendix A.) Rearranging Equation 3.61 to

$$\underline{\underline{\dot{\epsilon}}} = \langle \frac{\sqrt{J_2} - \kappa}{2\eta\sqrt{J_2}} \rangle \underline{\underline{S}} \tag{3.65}$$

and substituting Equation 3.64 into Equation 3.65 gives

$$\underline{\underline{\dot{\epsilon}}} = \langle \frac{\sqrt{2(\underline{\underline{\dot{\epsilon}}} : \underline{\underline{\dot{\epsilon}}})}}{2\sqrt{J_2}} \rangle \underline{\underline{S}}. \tag{3.66}$$

From Equation 3.10, $J_2 = 1/2\ (\underline{\underline{S}} : \underline{\underline{S}})$ which gives us

$$\underline{\underline{\dot{\epsilon}}} = \langle \frac{\sqrt{\underline{\underline{\dot{\epsilon}}} : \underline{\underline{\dot{\epsilon}}}}}{\sqrt{\underline{\underline{S}} : \underline{\underline{S}}}} \rangle \underline{\underline{S}} = \langle \dot{\lambda} \rangle \underline{\underline{S}} \tag{3.67}$$

where $\dot{\lambda} = \mathrm{d}\lambda/\mathrm{dt}$. If we neglect the elastic component of the strain and assume that we are always in the plastic regime, then we can remove the brackets from Equation 3.67 giving us the Levy-Mises theory of plasticity (Equations 3.52 and 3.54).

$$\underline{\underline{\dot{\epsilon}}} = \dot{\lambda} \underline{\underline{S}} \tag{3.52}$$

Multiplying Equation 3.52 by dt and denoting the strains with a superscript p to denote that they are the plastic component of the strain tensor gives us the Prandtl-Reuss equations:

$$\mathrm{d}\underline{\underline{\epsilon}}^{\mathrm{p}} = \sqrt{\frac{\mathrm{d}\underline{\underline{\epsilon}}^{\mathrm{p}} : \mathrm{d}\underline{\underline{\epsilon}}^{\mathrm{p}}}{\underline{\underline{S}} : \underline{\underline{S}}}}\,\underline{\underline{S}} = \frac{3}{2}\frac{\mathrm{d}\bar{\epsilon}^{\mathrm{p}}}{\sigma_{\mathrm{Y}}}\underline{\underline{S}} \qquad 3.55$$

seen in expanded form in Equations 3.58. The Prandtl-Reuss equations relate the plastic component of the strain to the stress and are used in Section 3.7a to calculate numerically the plastic deformation of a lithium-metal anode.

3.4d Analytical Solution to a Simplified Plasticity Problem

Before we solve numerically for the plastic deformation of lithium metal at the negative electrode, let us first solve a simplified problem analytically in order to gain an understanding of how the equations work. Building off an example in Section IV-6 of *Elements of the Mechanical Behavior of Solids*,[8] let us take, for example, an aluminum sheet of length l_0, width w_0, and thickness t_0. We now pull on the ends of the slab and make the simplifying assumption that the width remains the same, but the length increases to l. Following this program, we determine the final thickness of the slab and the maximum force necessary to stretch the aluminum to that length. As a first step, we decouple the elastic deformation and plastic deformation. Because the deformation is large, we assume that the elastic deformation is negligible and consider only the plastic deformation. Let us also assume that, rather than use an experimental stress-strain curve, the plastic portion of the uniaxial stress-strain curve can be fit by the power-law form:

$$\bar{\sigma} = \mathrm{C}\bar{\epsilon}^{n} \qquad 3.68$$

where, again, $\bar{\sigma}$ is the equivalent stress and $\bar{\epsilon}$ is the equivalent strain governed by Equations 3.21 and 3.23, respectively. Here, C and *n* are constants and are fitting parameters where *n* typically varies between 0 and 0.5.

We now align our axes such that x_1 is in the direction of the thickness of the slab, x_3 is along the length of the slab, and x_2, is along the width. Since we consider plastic deformation to be incompressible deformation, then:

$$\epsilon_{11} + \epsilon_{22} + \epsilon_{33} = 0 \qquad 3.69$$

or

$$\ln\left(\frac{t}{t_0}\right) + \ln\left(\frac{w}{w_0}\right) + \ln\left(\frac{l}{l_0}\right) = 0. \qquad 3.70$$

As defined by the problem, the width of the slab remains the same so that $\epsilon_2 = 0$, or $w = w_0$. This leads to

$$t = \frac{l_0}{l} t_0 \tag{3.71}$$

which relates the final thickness to the initial thickness and the initial and final lengths of the aluminum slab, all of which are known.

To determine the stress required to stretch the aluminum to length l, we use the Prandtl-Reuss equations. These were derived in Section 3.4c, and are repeated below (using principle stresses) for clarity:

$$\mathrm{d}\epsilon_1^{\mathrm{p}} = \frac{\mathrm{d}\bar{\epsilon}^{\mathrm{p}}}{\sigma_{\mathrm{Y}}}\left[\sigma_1 - \frac{1}{2}(\sigma_2 + \sigma_3)\right],$$

$$\mathrm{d}\epsilon_2^{\mathrm{p}} = \frac{\mathrm{d}\bar{\epsilon}^{\mathrm{p}}}{\sigma_{\mathrm{Y}}}\left[\sigma_2 - \frac{1}{2}(\sigma_1 + \sigma_3)\right], \tag{3.58}$$

and

$$\mathrm{d}\epsilon_3^{\mathrm{p}} = \frac{\mathrm{d}\bar{\epsilon}^{\mathrm{p}}}{\sigma_{\mathrm{Y}}}\left[\sigma_3 - \frac{1}{2}(\sigma_1 + \sigma_2)\right].$$

Since the slab deforms uniformly and is thin, σ_1 is assumed to be negligible. This leads to:

$$\mathrm{d}\epsilon_1^{\mathrm{p}} = -\frac{\mathrm{d}\bar{\epsilon}^{\mathrm{p}}}{2\sigma_{\mathrm{Y}}}(\sigma_2 + \sigma_3)\,,$$

$$\mathrm{d}\epsilon_2^{\mathrm{p}} = \frac{\mathrm{d}\bar{\epsilon}^{\mathrm{p}}}{\sigma_{\mathrm{Y}}}\left(\sigma_2 - \frac{1}{2}\sigma_3\right), \tag{3.72}$$

and

$$\mathrm{d}\epsilon_3^{\mathrm{p}} = \frac{\mathrm{d}\bar{\epsilon}^{\mathrm{p}}}{\sigma_{\mathrm{Y}}}\left(\sigma_3 - \frac{1}{2}\sigma_2\right).$$

Since $\epsilon_2 = \mathrm{d}\epsilon_2^{\mathrm{p}} = 0$, and

$$\sigma_2 = \frac{1}{2}\sigma_3, \tag{3.73}$$

Equations 3.70 thus reduce to

$$d\epsilon_1^p = -\frac{3}{4}\frac{d\bar{\epsilon}^p}{\sigma_Y}\sigma_3,$$

and 3.74

$$d\epsilon_3^p = \frac{3}{4}\frac{d\bar{\epsilon}^p}{\sigma_Y}\sigma_3.$$

Since the material is yielding, the yield stress can be related to the equivalent stress through Equation 3.42. With the prior simplification that $\sigma_1 = 0$, $\bar{\sigma}$ becomes

$$\sigma_Y = \bar{\sigma} = \left\{\frac{1}{2}[(\sigma_2 - \sigma_3)^2 + {\sigma_2}^2 + {\sigma_3}^2]\right\}^{1/2} = \frac{\sqrt{3}}{2}\sigma_3. \quad 3.75$$

The substitution of Equation 3.75 into Equations 3.74 yields

$$d\epsilon_1^p = -\frac{\sqrt{3}}{2}d\bar{\epsilon}^p,$$

and 3.76

$$d\epsilon_3^p = \frac{\sqrt{3}}{2}d\bar{\epsilon}^p.$$

Integrating Equations 3.76 from the initial strain (which is zero) to the final strain gives us

$$\epsilon_1^p = -\frac{\sqrt{3}}{2}\bar{\epsilon}^p,$$

and 3.77

$$\epsilon_3^p = \frac{\sqrt{3}}{2}\bar{\epsilon}^p.$$

Inverting the equations and substituting $\ln\left(\frac{l}{l_0}\right)$ for ϵ_3^p yields:

$$\bar{\epsilon}^p = \frac{2}{\sqrt{3}}\ln\left(\frac{l}{l_0}\right). \quad 3.78$$

Finally, substituting Equation 3.78 into Equation 3.68, we find

$$\bar{\sigma} = C\left[\frac{2}{\sqrt{3}}\ln\left(\frac{l}{l_0}\right)\right]^n. \quad 3.79$$

Using empirically found values for C and n gives us the equivalent stress through Equation 3.79. We can then employ Equation 3.75 to solve for the stress pulling on the ends of the metal plate that is required to stretch the plate to the dimensions specified.

As we can see from this example, the equations derived in Section 3.4 can be simplified so that, with simple geometries, they can be solved analytically without too much difficulty. For the problem at hand, the plastic deformation of lithium due to a very stiff separator, we use the general equations and solve them numerically such as will be described in Section 3.7.

3.5 Elastic Deformation of Lithium Metal due to a Very Stiff Separator

Now that we have developed an understanding of stress, strain, and elastic and plastic deformation, we can turn our focus onto the problem at hand: to determine the effects of a stiff polymer separator on a lithium-metal negative electrode. Such a separator resists the movement of lithium seen in Chapters 1 and 2, through the generation of stresses in the cell. As you can imagine, as the lithium moves, the separator is either compressed or stretched. This translates into stresses throughout the cell that affect the negative electrode through two mechanisms: altering the thermodynamics of the negative electrode and deforming the negative electrode mechanically. To that end, in this section, the model developed in Chapter 1 is updated to include both of these mechanisms.

In this section the effect of the stress on the thermodynamics is developed along with the elastic deformation of the negative electrode. In Section 3.5a, we introduce the assumptions made and the geometry used in the model. Then, in Section 3.5b, we develop equations for the effect of stress on the thermodynamics of lithium metal and incorporate the change into the Butler-Volmer kinetic equation for the reaction at the surface of the negative electrode. In Section 3.5c we update the model developed in Chapter 1 to include the kinetic equation developed in Section 3.5b and discuss the results. Subsection 3.5d devotes itself to the addition of elastic deformation of the lithium into the model and the discussion of the results of the addition of elastic deformation.

3.5a Introduction, Assumptions, and Model Geometry

Before we describe how the pressure, due to the addition of a stiff polymer separator, affects the thermodynamics of the reaction kinetics at the negative electrode, we first describe the model geometry and assumptions. In this chapter we update the model developed in Chapter 1, which incorporates a moving boundary at the negative electrode, a CoO_2 intercalation electrode as the cathode (modeled using porous electrode theory), and a lithium-metal negative electrode. In Chapter 1, the separator was modeled as a liquid electrolyte with a

binary salt, and the total volume changes were assumed to be zero. In this chapter, however, the separator is updated to a theoretical polymer separator which has similar transport properties to the liquid electrolyte but has mechanical properties which inhibit dendrites. As an approximation, the separator is modeled as a series of springs, such as is seen in Figure 3.10. It should be noted here that the same cell geometry from Chapter 1 is used in this chapter and that Figure 3.10 is a repeat of the model geometry shown in Figure 1.1.

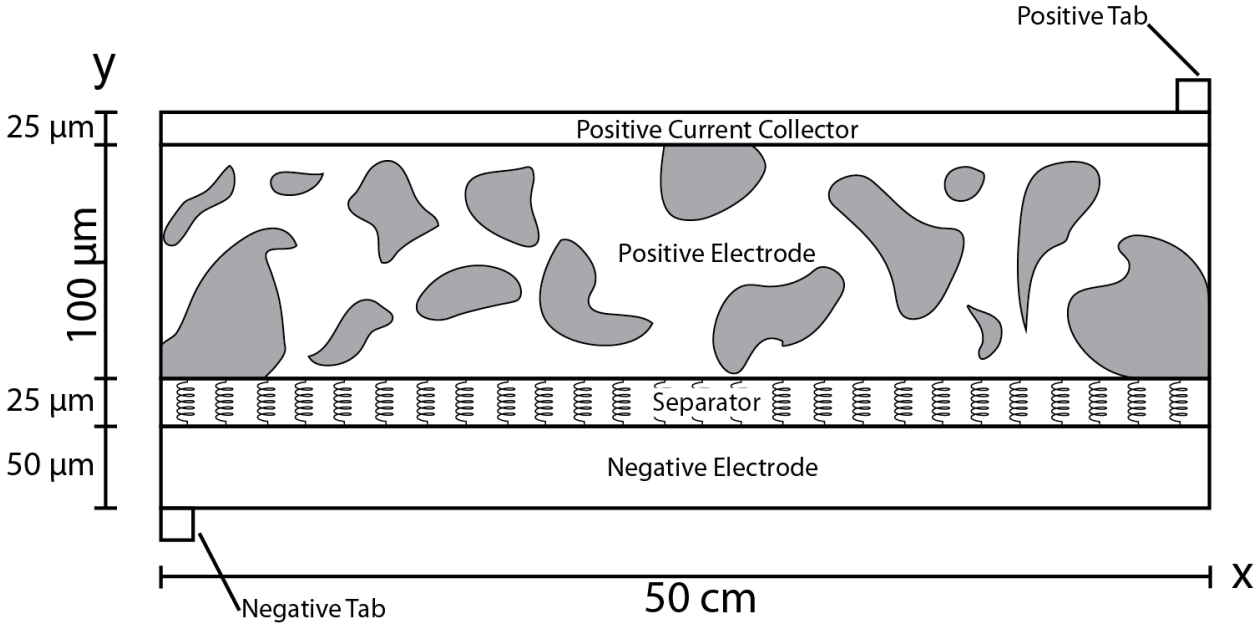

Figure 3.10 Two-dimensional model geometry of a lithium-metal battery, consisting of a lithium-metal negative current collector, a lithium-metal negative electrode, a polymer separator, composite cathode, and aluminum positive current collector. The polymer separator is modeled here as a series of springs.

Furthermore, while in Chapter 1 the volume of the separator was assumed to vary with the consumption or deposition of lithium, thereby maintaining the total volume of the cell, in this chapter, the volume of the separator remains constant. This means that the total volume of the cell decreases during discharge, when the lithium is consumed, and the thickness of the negative electrode shrinks. Conversely, on charge, the deposition of lithium at the negative electrode causes the total volume to increase. If the volume of the separator were to vary during discharge (as it was allowed to do in Chapter 1), one can imagine that during discharge, as the lithium is consumed and the volume of the separator increases, the entire cell would experience considerable tension well beyond anything that could be considered reasonably possible. Furthermore, a commercially available cell is typically in a casing which allows for some expansion and contraction while still preserving some compression on the cell to maintain contact between the separator and electrodes. To put it another way, one can

imagine this system, where the volume of the separator is conserved, to be equivalent to a small weight being placed on the cell such that a compressive force is maintained while the volume of the cell is allowed to expand and contract.

To gain an initial understanding of how the stresses change during cycling, we turn our attention to Figure 3.11, below, where we have zoomed in on Figure 3.10 to get a closer look at the separator. In this state, the lithium is in its starting position and is flat. The local pressure is the average pressure, and we take this as the initial pressure in the cell or p^o.

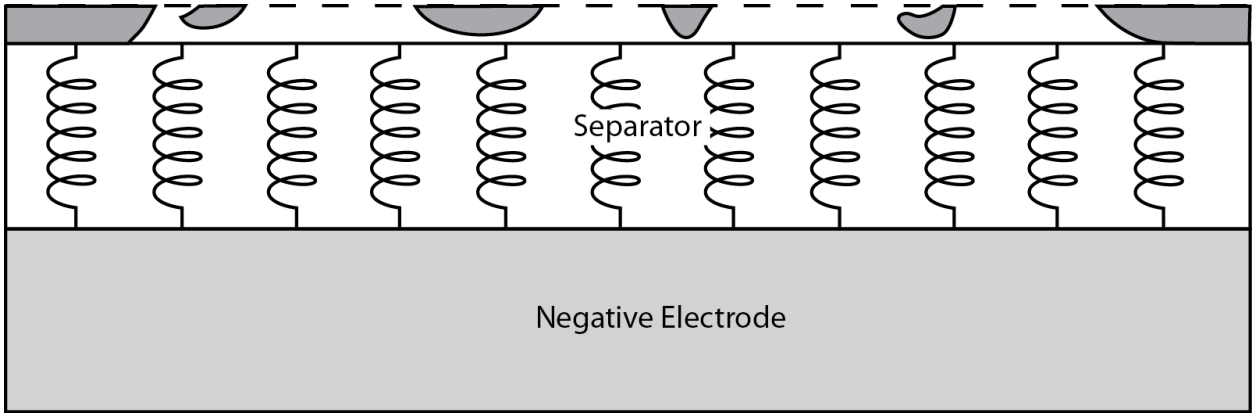

Figure 3.11. Close-up of the separator and negative electrode seen in Figure 3.10 in its undeformed state. Here the separator is modeled as a series of springs which, with the movement of the negative electrode, will exert a resisting force.

As we discharge the cell, we saw in Chapter 1 that current distributions led to more lithium being removed on the left side of the cell than the right. This led to a lithium profile such as is seen in Figure 3.12 below. Again, in this chapter, the volume of the separator remains the same while the thickness of the negative electrode decreases due to the lithium being consumed. Therefore, the faster consumption of lithium on the left leads to a local tensile force on the left, where the separator is stretched, and a local compressive force on the right, where the separator is compressed. It should be noted here that because the volume of the separator remains the same, the average pressure in the cell, after discharge, remains at p^o.

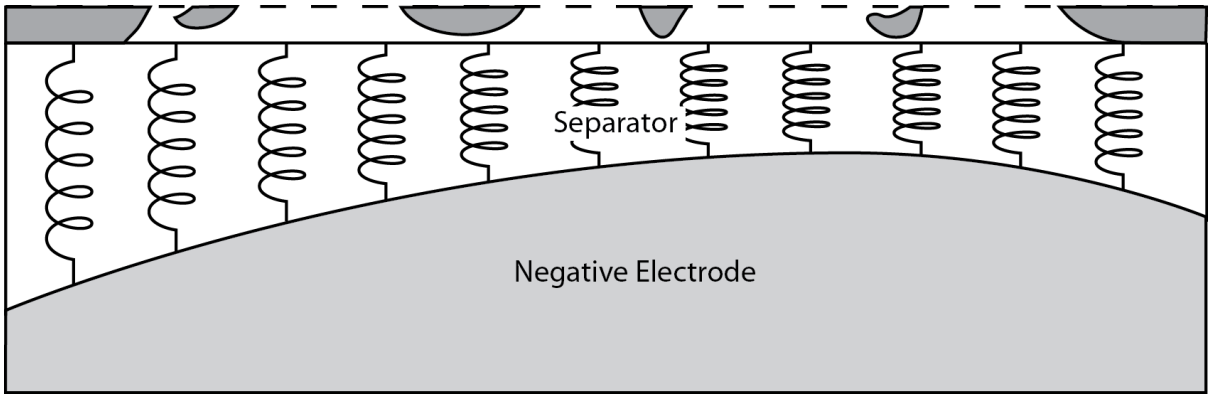

Figure 3.12. Close-up of the separator and negative electrode seen in Figure 3.10 in its deformed state directly following a discharge phase. Here the separator is modeled as a series of springs which, due to the uneven distribution of lithium, is exerting a resisting force.

Of course, the opposite is true after a full cycle where, as we saw in Chapter 1, the lithium accumulated on the left side of the cell after the charge phase. In this case, the separator is compressed on the left side of the cell where the negative electrode is thicker and is in tension on the right side where the lithium is thinner. Again, since the volume of the separator is maintained, the average pressure in the separator is maintained at $\mathrm{p^o}$, which is the base pressure.

3.5b The Effects of Pressure on the Reaction Kinetics

The Effect of Pressure on the Thermodynamics of a Reaction

Now that we have an understanding of the model geometry and some of the basic assumptions that we are making, let us derive how the pressure on the negative electrode will alter the chemical potential of the lithium.

Maxwell's relations may be used to get an expression for the chemical potential as a function of pressure

$$\left(\frac{\partial \mu_i}{\partial p}\right)_{T,\, c_i} = \overline{V}_i \tag{3.80}$$

where $\overline{V}_i$ is the partial molar volume of species i. If we assume that the partial molar volume is constant, we can integrate the partial derivatives and get:

$$\mu_i - \mu_i^o = (p - p^o)\overline{V}_i \tag{3.81}$$

or

$$\Delta\mu_i^p = \Delta p\overline{V}_i \tag{3.82}$$

where $\Delta\mu_i^p$ is the change in the chemical potential of species i due to an applied pressure, Δp. We note that p is now the thermodynamic pressure.

Let us take the reaction at the interface at the negative electrode to be

$$Li \leftrightarrow Li^+ + e^-. \tag{3.83}$$

If we convert the reaction into chemical potentials we get

$$\mu_{Li} = \mu_{Li^+} + \mu_{e^-}. \tag{3.84}$$

Let us define the electrochemical potential of species i under pressure to be μ_i^p giving us

$$\mu_{Li}^p = \mu_{Li^+}^p + \mu_{e^-}^p. \tag{3.85}$$

Subtracting Equation 3.84 from Equation 3.85 gives us

$$\Delta\mu_{Li}^p = \Delta\mu_{Li^+}^p + \Delta\mu_{e^-}^p. \tag{3.86}$$

Substituting Equation 3.82 into Equation 3.86 gives us

$$\Delta\mu_{e^-}^p = \Delta p^M\overline{V}_{Li} - \Delta p^e\overline{V}_{Li^+} \tag{3.87}$$

or, the change in the electrochemical potential of an electron in the metal due to a change in the pressure. Here Δp^M is the change in pressure in the metal phase and Δp^e is the change in pressure in the electrolyte phase. The difference in pressure between the solid phase and the electrolyte phase is due to the surface tension and the curvature of the surface. Since we are interested in how the change in pressure effects the chemical potentials we need to use the change in the surface tension as the material deforms. This change in the surface tension is give by

$$\Delta p^\gamma = \gamma\left(\frac{1}{r_1} + \frac{1}{r_2}\right) \tag{3.88}$$

where γ is the surface tension (a function of temperature, pressure, and composition) and r_1 and r_2 are the radii of curvature, as given by the Laplace equation. Since r_1 and r_2 are very large, then we can assume that the surface tension does not change appreciably. Monroe et al.[4] also found the contribution of surface tension to be very small compared to the other mechanical forces involved in the abatement of dendrites. Thus:

$$\Delta p^{M} \approx \Delta p^{e} \approx \Delta p \tag{3.89}$$

and

$$\Delta \mu_{e^-}^{p} = \Delta p \overline{V}_{Li} - \Delta p \overline{V}_{Li^+} = \Delta p \left(\overline{V}_{Li} - \overline{V}_{Li^+} \right). \tag{3.90}$$

To obtain the partial molar volume of the lithium ion in solution, we employ the relationship proposed by Newman and Chapman,[33]

$$\overline{V}_{Li^+} = \frac{t_-^0 \overline{V}_{LiX}}{\nu_+ (t_-^0 + t_+^0)}. \tag{3.97}$$

where $\overline{V}_{LiX}$ is the partial molar volume of neutral salt in the electrolyte, ν_+ and ν_- are the stoichiometric numbers of ions in a unit formula of the neutral salt, and t_-^0 and t_+^0 are the anionic and cationic transference numbers.

In this analysis by Newman and Chapman,[33] Q was used to represent the quantity

$$Q = \frac{t_+^0}{z_+} \overline{V}_+ + \frac{t_-^0}{z_-} \overline{V}_-. \tag{3.92}$$

It was noted that this quantity could not be measured independently, and was arbitrarily taken to be zero. This led to the assumption (based solely on convenience) that the transference numbers of the ions were inversely proportional to their partial molar volumes and no physical significance should be attached to it.[33]

The Effects of Pressure on the Reaction Kinetics at the Negative Electrode

Let us now turn our attention to deriving the effect of pressure on the reaction kinetics at the negative electrode. To do this, we first take the Butler-Volmer equation and assume that the activity of the reduced species (which is the lithium metal) is one. This gives us the familiar equation:

$$\frac{i_{loc}}{F} = k_a \exp\left(\frac{\alpha_a F \Phi}{RT}\right) - k_c a_{Li^+} \exp\left(-\frac{\alpha_c F \Phi}{RT}\right). \quad 3.93$$

We now state that the measured potential across the interface of the negative electrode is equal to the open-circuit potential of lithium at standard pressure plus the surface overpotential plus the open-circuit potential due to deformation of the electrode:

$$\Phi = U_0 + \eta_s - \frac{\Delta\mu_{e^-}^p}{F}. \quad 3.94$$

Substituting Equation 3.94 into Equation 3.93 leads to

$$\frac{i_{loc}}{F} = k_a \exp\left[\frac{\alpha_a F\left(U_0 + \eta_s - \frac{\Delta\mu_{e^-}^p}{F}\right)}{RT}\right] - k_c c_{Li^+} \exp\left[-\frac{\alpha_c F\left(U_0 + \eta_s - \frac{\Delta\mu_{e^-}^p}{F}\right)}{RT}\right]. \quad 3.95$$

Through algebra, we get:

$$\frac{i_{loc}}{F} = k_a \exp\left(\frac{\alpha_a F(U_0 + \eta_s)}{RT}\right)\exp\left(-\frac{\alpha_a \Delta\mu_{e^-}^p}{RT}\right) - k_c c_{Li^+} \exp\left(-\frac{\alpha_c F(U_0 + \eta_s)}{RT}\right)\exp\left(\frac{\alpha_c \Delta\mu_{e^-}^p}{RT}\right). \quad 3.96$$

And, through further rearranging, we get

Since we set our reference at standard pressure, at open circuit $\eta_s = \Delta\mu_{e^-}^p = i_{loc} = 0$. Thus, the open-circuit potential U_0 is

$$U_0 = \frac{RT}{F} \ln\left(\frac{k_c c_{Li^+}}{k_a}\right). \quad 3.97$$

Plugging U_0 into Equation 3.96 and doing some algebra leads to

$$\frac{i_{loc}}{F} = k_a{}^{\alpha_c} k_c{}^{\alpha_a} c_{Li^+}{}^{\alpha_a} xp\left(-\frac{\alpha_a \Delta\mu_{e^-}^{p}}{RT}\right)\exp\left(\frac{\alpha_a F}{RT}\eta_s\right) - k_a{}^{\alpha_c} k_c{}^{\alpha_a} c_{Li^+}{}^{\alpha_a}\exp\left(\frac{\alpha_c \Delta\mu_{e^-}^{p}}{RT}\right)\exp\left(-\frac{\alpha_c F}{RT}\eta_s\right). \quad 3.98$$

We can now factor out the pre-exponential terms into the exchange current density leaving

$$i_{loc} = i_0\left[\exp\left(-\frac{\alpha_a \Delta\mu_{e^-}^{p}}{RT}\right)\exp\left(\frac{\alpha_a F}{RT}\eta_s\right) - \exp\left(\frac{\alpha_c \Delta\mu_{e^-}^{p}}{RT}\right)\exp\left(-\frac{\alpha_c F}{RT}\eta_s\right)\right], \quad 3.99$$

where $i_0 = F k_a{}^{\alpha_c} k_c{}^{\alpha_a} c_{Li^+}{}^{\alpha_a}$. Equation 3.99 gives us a kinetic expression for the reaction at the lithium-metal negative electrode as we vary the pressure.

There is, however, an alternate form of the pressure-modified kinetic expression proposed by Monroe et al.[39] which is build off the work by Barton and Bockris[34] and Diggle et al.[34] From an analysis of growth rates of zinc dendrites, Diggle et al. extended the model proposed by Barton and Bockris for the kinetics of the reaction at the tip of a dendrite. They state that the ratio of the activities of the reverse anodic reaction must take into account the Kelvin term, which becomes appreciable at low values of dendrite tip radii. The Kelvin term is, for the case of lithium metal,

$$\frac{2\gamma \overline{V}_{Li}}{r} \quad 3.100$$

where γ is the surface energy (i.e., surface tension) of the lithium/electrolyte interface, r is the radius of the dendrite tip, and $\overline{V}_{Li}$ is the molar volume of lithium. From this, Diggle et al. include Equation 3.100 in the Butler-Volmer kinetic expression through the addition of an exponential term in front of the reverse reaction rate such that

$$i_{tip} = i_0\left[\left(1 - \frac{i}{i_L}\right)\exp\left(\frac{-\alpha_c F}{RT}\eta_s\right) - \exp\left(\frac{2\gamma \overline{V}_{Li}}{RT \cdot r}\right)\exp\left(\frac{\alpha_a F}{RT}\eta_s\right)\right], \quad 3.101$$

where i_{tip} is the current density at the tip of the dendrite, i is the average current, and i_L is the limiting current.

Monroe et al.[39] extended this kinetic expression to include mechanical pressure effects which appear in both the surface overpotential (as in Equation 3.94) and in exponential terms in front of both the anodic and cathodic terms in the Butler-Volmer equation. This leads to the equation

$$i_{loc} = i_0 \left\{ \exp\left[\frac{(\alpha_m - \alpha_a)\Delta\mu_{e^-}^p}{RT}\right] \exp\left(\frac{\alpha_a F}{RT}\right)\eta_s - \exp\left[\frac{(\alpha_m + \alpha_c - 1)\Delta\mu_{e^-}^p}{RT}\right] \exp\left(-\frac{\alpha_c F}{RT}\eta_s\right)\right\} \quad 3.102$$

where Monroe et al. defines a new mechanical transfer coefficient, α_m. They then assume that $\alpha_a = \alpha_c = 0.5$ and $\alpha_m = 1$ which allows for the exponents to be factored out leaving

$$i_{loc} = i_0 \exp\left[\frac{(1-\alpha_a)\Delta\mu_{e^-}^p}{RT}\right]\left[\exp\left(\frac{\alpha_a F}{RT}\eta_s\right) - \exp\left(-\frac{\alpha_c F}{RT}\eta_s\right)\right]. \quad 3.103$$

The assumption that $\alpha_m = 1$ and the difference between Equation 3.99 and 3.103 should be explored further. However, in this thesis, only Equation 3.99 is used. This is due to the fact that, as seen in Section 3.7b, with the addition of plastic deformation, the pressure-modified kinetics play only a very small role in forcing the lithium toward uniformity.

3.5c The Effects of Kinetics on the Movement of Lithium

Now that we have updated the Butler-Volmer kinetics to include the effects of pressure, we can turn our attention toward describing how the kinetics affects the movement of lithium seen in Chapter 1. As we saw in Figures 3.10, 3.11, and 3.12, the separator is considered to be maintained at a constant volume and is modeled as a series of ideal springs. This allows the use of Hooke's law where σ_y is the force on lithium, Δy is the change in the local thickness of the separator relative to its initial thickness before cycling (y^0), and E_{Sep} is the elastic modulus of the separator:

$$\sigma_y = \frac{E_{Sep}}{y^0}\Delta y. \quad 3.104$$

Because the separator is a series of springs, the only force exerted on the negative electrode by the separator is σ_y. Therefore, Δp in Equation 3.89 is simply $\sigma_y - \sigma_y^o$, where σ_y^o is the initial force on the negative electrode or, in this case, 1 bar. Thus,

$$\Delta p = \frac{E_{Sep}}{y^0}\Delta y. \qquad 3.105$$

We can now use Equation 3.99 for the kinetic equation at the negative electrode in the model developed in Chapter 1, using Equation 3.90 as the expression for the change in the electrochemical potential of the electron due to pressure. The pressure is determined by the movement of lithium and is calculated through Equation 3.105. Thus, the movement of the lithium is coupled to the kinetics at the interface through the pressure caused by the resistance of the separator to the movement of the lithium.

In this section the lithium is assumed to be rigid and does not deform mechanically. The separator, however, is allowed to deform and exerts a force on the lithium governed by Equation 3.104. While this force on the negative electrode due to the deformation of the separator does not mechanically deform the lithium, it does alter the kinetics at the negative electrode through Equation 3.99. As can be seen in this Section (which is consistent with the finding of Monroe et al.[4,39]), the deformation of the separator forces the current distribution to be more nearly uniform causing a much more uniform lithium profile.

The lithium-metal battery was cycled galvanostatically at a C/2 rate for one cycle beginning with a discharge, followed by a rest period of 1000 seconds, and completed by a charge at the same rate and duration as the discharge. The current needed to achieve the C/2 rate was calculated from the theoretical current needed to achieve a 2 hour discharge rate at the positive electrode. The time of the discharge was calculated based on the theoretical time required to fill 50 percent of the available capacity in the positive electrode such that y in Li_yCoO_2 varied from 0.5 to 0.75.

In order to determine the effect that the separator has on the movement of lithium, two different elastic moduli for the separator where chosen, 400 MPa and 16 GPa. An elastic modulus of 400 MPa was chosen because it falls within the range of values for the elastic modulus of polyethylene and polypropylene found in the literature.[26-28] The second value for the elastic modulus of the separator was chosen to be 16 GPa which, when converted to a shear modulus, is 6.8 GPa, or twice the shear modulus of lithium at 3.4 GPa.[4, 29, 30] (The requirement for the shear modulus of the separator to be at least 6.8 GPa was predicted by Monroe et al.[4] to be sufficient to inhibit the growth of dendrites. This model included the pressure-modified kinetic equation (Equation 3.99) as well as elastic deformation of the lithium due to mechanical forces). The results of the model immediately after the charge phase are shown in Figure 3.13 below and are labeled '400 MPa Separator' and '16 GPa Separator'. The 'Pliable Separator' line in Figure 3.13 is the 'C/2' result from Figure 1.4 where the separator did not resist the movement of the lithium at the negative electrode and is used as a comparison for the 400 MPa separator and 16 GPa separator.

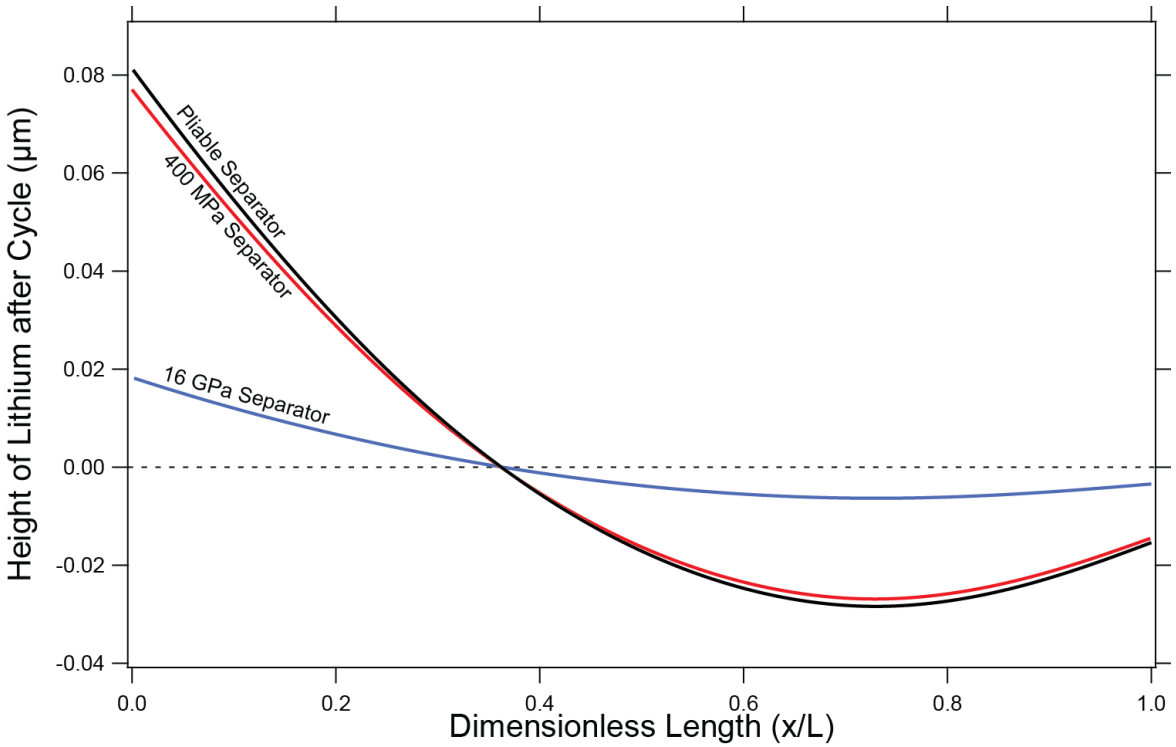

Figure 3.13. Height of the lithium negative electrode along the lithium/separator interface relative to its starting position immediately after a cycle consisting of a discharge, rest, then a charge at a C/2 rate to a 50% depth of discharge with three different separator rigidities. The 'Pliable Separator' line is taken from the 'C/2' line in Figure 1.4, where the separator did not resist movement of the lithium.

From Figure 3.13, we can see that a separator with an elastic modulus of 400 MPa does not change the movement of the lithium appreciably from the results found in Chapter 1. However, the '16 GPa Separator' line shows a significant departure from the results of Chapter 1. Both of these results are somewhat expected since Monroe and Newman found that the elastic modulus of the separator needs to be on the order of 16 GPa to inhibit dendrite propagation.[4] If such a separator is employed to inhibit dendrites, then it should also significantly resist any movement of lithium whether dendritic or otherwise. The '400 MPa Separator' line does, however, show that the results from Chapter 1 are fairly accurate if a standard polypropylene Celgard separator with a liquid electrolyte is used and dendrites are not found.

3.5d Elastic Deformation of Lithium Metal

From the '16 GPa Separator' line in Figure 3.13, we see that a very stiff separator significantly reduces the movement of the lithium (over a 75% reduction) when compared to a

pliable separator. However, this comes at the cost of the through-cell pressure peaking at 120 bar or 12 MPa, as is seen in Figure 3.14 below.

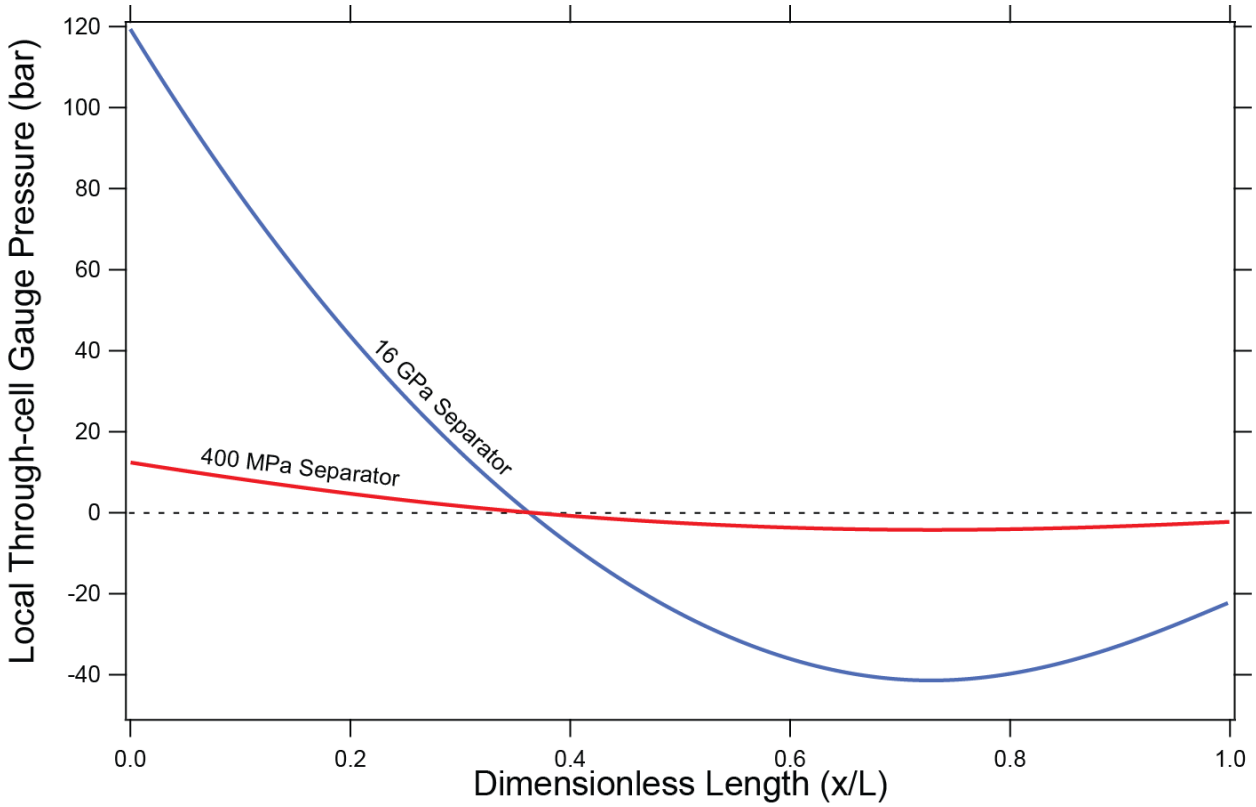

Figure 3.14 Pressure distribution along the lithium/separator interface immediately after a cycle consisting of a discharge, rest, then a charge at a C/2 rate to a 50% depth of discharge with two different elastic moduli for the separator.

Furthermore, on the right side of the cell, where the lithium is thinner, the cell is in tension by over 40 bar. Under these conditions one should expect some sort of mechanical failure within the battery and, at least, significant elastic deformation of the lithium, thereby relieving the stresses in the cell. Even with a separator with an elastic modulus of only 400 MPa, the through-cell pressure peaks at about 12 bar on the left, which would cause at least some elastic deformation of the lithium. The case for including elastic deformation of the lithium is strengthened when we compare the elastic modulus of lithium, which is 4.9 GPa, to the elastic modulus of the dendrite-inhibiting polymer, which is 16 GPa. From a simple inspection, we can conclude that the lithium would deform much more readily than the stiffer separator, causing the results found in both Figures 3.13 and 3.14 to be overestimations. Therefore, we include the elastic deformation of the lithium through Hooke's law:

$$\underline{\underline{\epsilon}}_{Li} = \frac{1-\nu}{E_{Li}}\underline{\underline{\sigma}} - \frac{\mathrm{tr}(\underline{\underline{\sigma}})}{E}\underline{\underline{I}}, \tag{3.32}$$

Here we assume that the lithium is perfectly elastic, or the Poisson's ratio is zero. This leads to

$$\underline{\underline{\epsilon}}_{Li} = \frac{\underline{\underline{\sigma}}}{E_{Li}}, \quad \text{or} \quad \epsilon_{y\,Li} = \frac{\sigma_y}{E_{Li}} \tag{3.106}$$

due to the fact that the separator is only assumed to exert a force on the lithium in the y direction. In Equation 3.106, $\epsilon_{y\,Li}$ is the elastic deformation of the lithium in the y direction, σ_y is the local force on the lithium (seen in Figure 3.14), and E_{Li} is the Young's modulus of the lithium. The elastic deformation of the lithium, calculated through Equation 3.106, now modifies the thickness of the lithium through the equation:

$$\Delta y_{Li} = y_{Li} - \epsilon_{y\,Li} y_{Li} - y_{Li}^0, \tag{3.107}$$

where Δy_{Li} is the change in the height of the lithium relative to its average height, y_{Li} is the local thickness of the lithium, and y_{Li}^0 is the average height of the lithium. We update Equation 3.104 to include the elastic deformation of the negative electrode:

$$\sigma_y = \frac{E_{Sep}}{y^0}\Delta y_{Li}. \tag{3.108}$$

We now iterate Equations 3.106 through 3.108 using the stress found in Section 3.6c as the initial condition, and the results are in Figure 3.15 below.

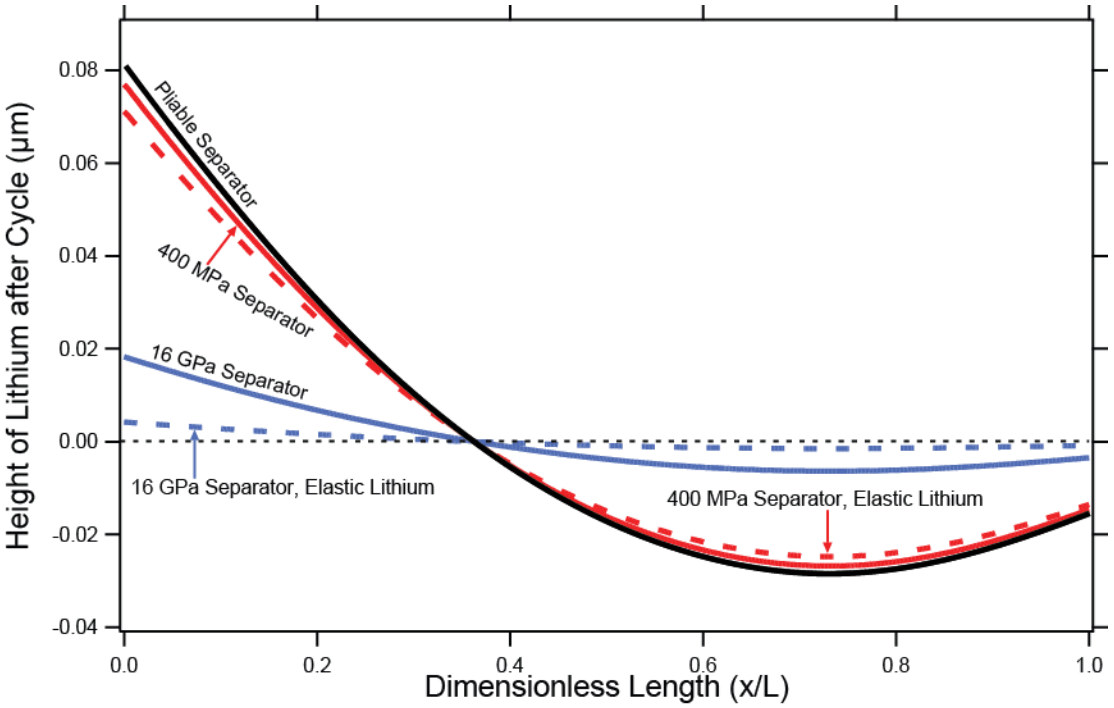

Figure 3.15 Height of the lithium negative electrode along the lithium/separator interface relative to its starting position immediately after a cycle consisting of a discharge, rest, then a charge at a C/2 rate to a 50% depth of discharge with three different elastic moduli for the separator. The 'Pliable Separator' line is taken from the 'C/2' line in Figure 1.4, where the separator did not resist movement of the lithium, and the dashed lines represent the inclusion of elastic deformation of the lithium. The solid colors are from Figure 3.13 and represent the effect of pressure on the electrode kinetics and elasticity of the separator, but not the elastic response of the lithium.

From Figure 3.15, we can see that a separator with an elastic modulus of 400 MPa causes only slight elastic compression (red dashed line in Figure 3.15). This slight deviation is expected since the separator is about an order of magnitude more elastic than the lithium. Thus, the separator will deform much more readily. However, with a dendrite-inhibiting separator with an elastic modulus of 16 GPa, significant elastic deformation of the lithium is seen (blue dashed line in Figure 3.15). In fact, by including elastic deformation, the lithium is deformed to around a quarter of the height it was when it was assumed to be rigid (solid blue line in Figure 3.15), and the movement is reduced to only 5 percent of its original height from Chapter 1, when a pliable separator was used (black line in Figure 3.15).

The elastic deformation of the lithium also has an effect on the through-cell pressure, as can be seen from Figures 3.16 and 3.17 below. With a separator that has a 400 MPa elastic modulus, the elastic deformation of the lithium only slightly reduced the through-cell pressure since the separator is much more elastic than the lithium. In the case of a separator with a 16

GPa elastic modulus, however, the through-cell pressure was significantly reduced to a maximum of around 27 bar. Again, this is due to the fact that the lithium deformed significantly.

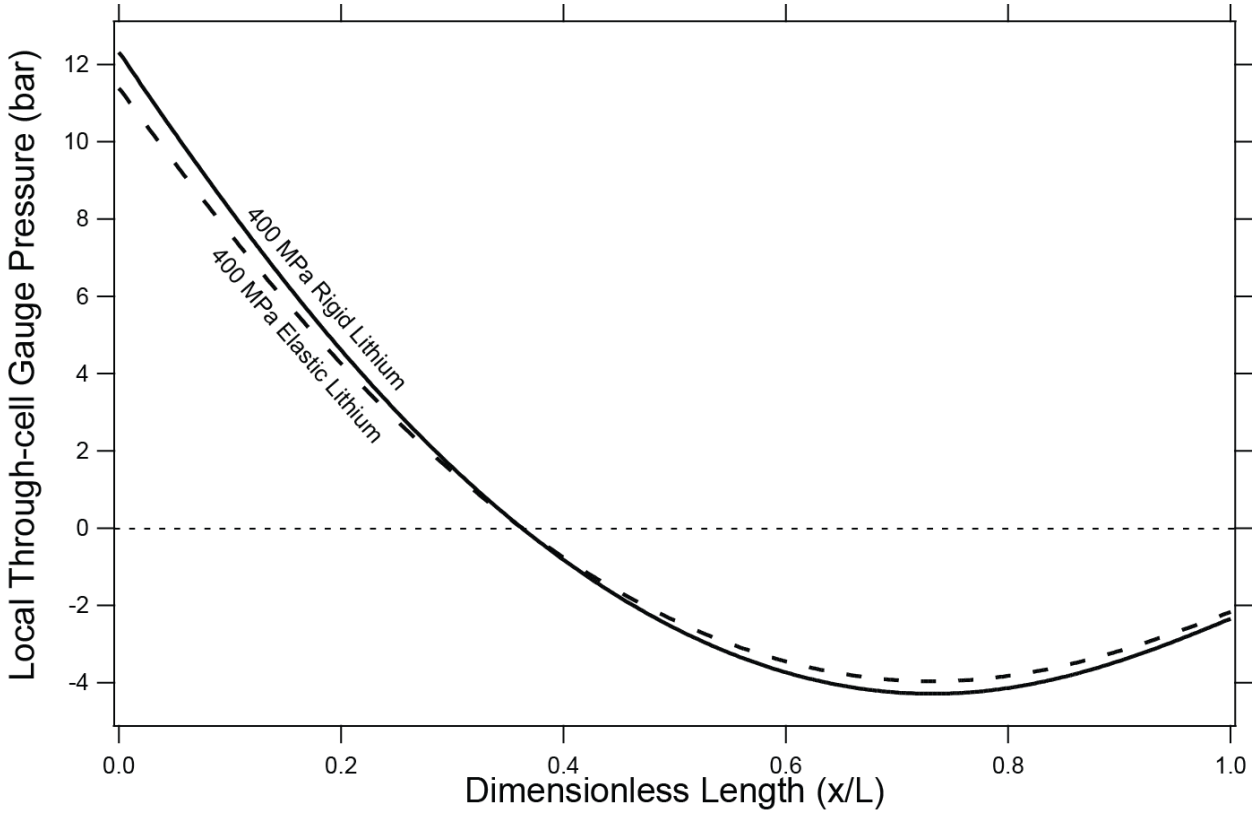

Figure 3.16. Pressure distribution along the lithium/separator interface immediately after a cycle consisting of a discharge, rest, then a charge at a C/2 rate to a 50% depth of discharge for a separator with an elastic modulus of 400 MPa. The solid line assumes that the lithium is perfectly rigid, and the dashed line allows for elastic deformation of the lithium.

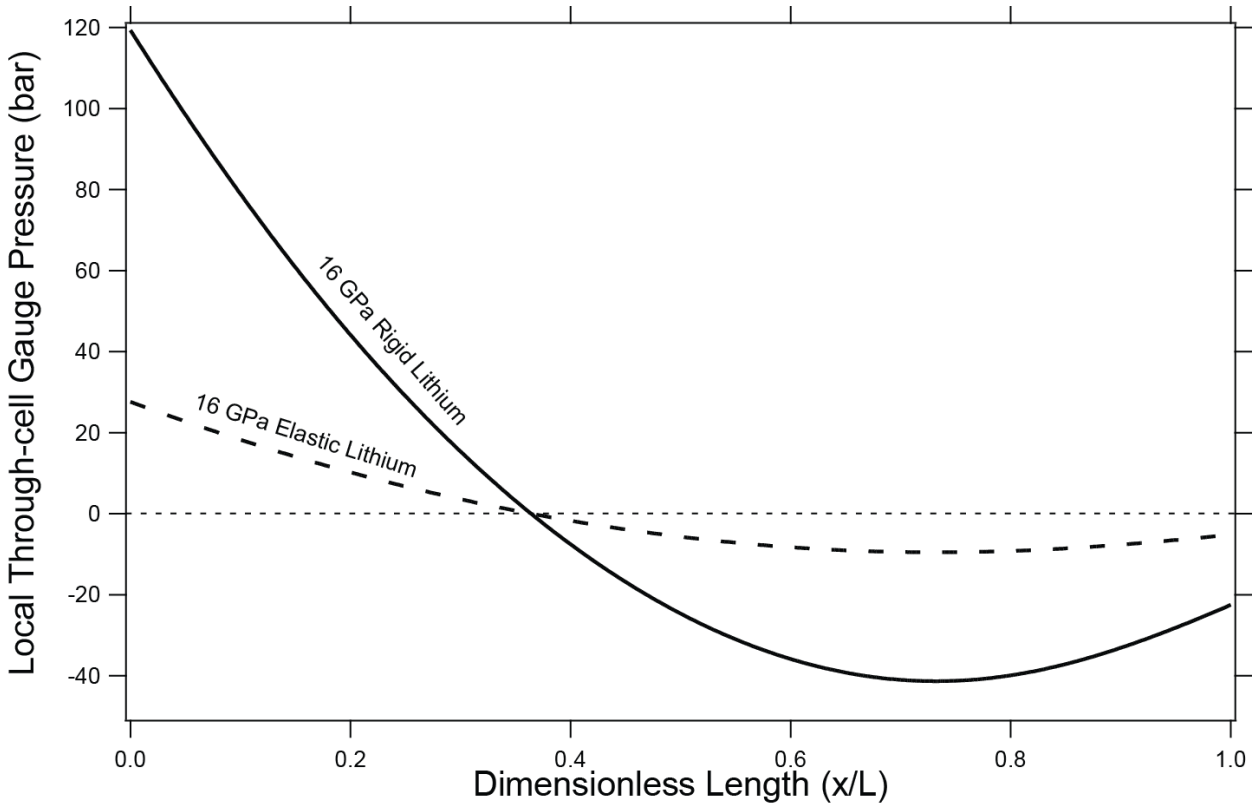

Figure 3.17. Pressure distribution along the lithium/separator interface immediately after a cycle consisting of a discharge, rest, then a charge at a C/2 rate to a 50% depth of discharge for a separator with an elastic modulus of 16 GPa. The solid line assumes that the lithium is perfectly rigid, and the dashed line allows for elastic deformation of the lithium.

Testing the Assumption of Constant Partial Molar Volume

If we are to assume that the lithium is able to deform elastically, then we must also look at the assumption in Equation 3.81 that the partial molar volume of the lithium, $\overline{\mathrm{V}}_{\mathrm{Li}}$, remains constant. From the definition of partial molar volume, we derive that the partial molar volume of lithium is related to the pressure by

$$\overline{\mathrm{V}}_{\mathrm{Li}} = \overline{\mathrm{V}}_{\mathrm{Li}}^{0}\left(1 - \frac{\Delta \mathrm{P}}{\mathrm{E}_{\mathrm{Li}}}\right). \qquad 3.109$$

Here $\overline{\mathrm{V}}_{\mathrm{Li}}$ is the partial molar volume of the lithium under pressure, $\overline{\mathrm{V}}_{\mathrm{Li}}^{0}$ is the initial partial molar volume of lithium, $\Delta \mathrm{P}$ is the change in pressure from its initial state, and E_{Li} is the Young's modulus of lithium. We now use Equation 3.109 to calculate Table 3.1 at various pressures.

Table 3.1. The change in the partial molar volume (calculated from Equation 3.109) and the corresponding percent change from the initial partial molar volume of lithium due to elastic deformation caused by a pressure, ΔP. Δy_{comp} (calculated from Equation 3.106) is the corresponding change in the height of the lithium due to elastic deformation.

ΔP (bar)	$\overline{V}_{Li}$ (m^3/mol)	Percent Change	Δy_{comp} (μm)
0	1.299×10^{-5}	0.0000%	0.00
20	1.2993×10^{-5}	-0.0408%	-1.02×10^{-2}
40	1.2987×10^{-5}	-0.0816%	-2.04×10^{-2}
60	1.2982×10^{-5}	-0.1224%	-3.06×10^{-2}
80	1.2977×10^{-5}	-0.1633%	-4.08×10^{-2}
100	1.2972×10^{-5}	-0.2041%	-5.10×10^{-2}
120	1.2966×10^{-5}	-0.2449%	-6.12×10^{-2}
140	1.2961×10^{-5}	-0.2857%	-7.14×10^{-2}
160	1.2956×10^{-5}	-0.3265%	-8.16×10^{-2}
180	1.2950×10^{-5}	-0.3673%	-9.18×10^{-2}
200	1.2945×10^{-5}	-0.4082%	-1.02×10^{-1}

From Table 3.1, we see that even with a significant pressure of 100 bar applied to lithium metal, the partial molar volume changes by only about 0.2%. Thus, the partial molar volume of lithium metal, $\overline{V}_{Li}$, can be assumed to be constant with little error. This does not mean, however, that elastic deformation is negligible, simply that the partial molar volume of lithium can be thought of as a constant. The lithium is still compressed due to pressure thereby changing both the profile and the pressure gradient seen during cycling. We can see this in the Δy_{comp} column in Table 3.1, which estimates the change in the height of the lithium from elastic deformation due to an applied pressure. Even though the change in the partial molar volume of lithium metal is slight, the compression of lithium is on the order of the movement of lithium seen in Figures 3.13 and 3.15.

3.6 Limit Analysis as it Applies to Plasticity in Batteries

As we saw in Figure 3.17, including the elastic deformation of the lithium at the negative electrode reduces the stress on the lithium substantially. Even so, if we take the yield strength of lithium metal into account, which is 6.55 bar,[31] even modest changes in the thickness of the lithium result in pressures above the yield strength. This can be seen more clearly in Figure 3.18 below, where horizontal lithium yield-stress lines are superimposed on the plot of the through-cell pressure after elastic deformation of the lithium (taken from the '16 GPa Elastic Lithium'

line in Figure 3.17). From Figure 3.18, we can see that, even if the lithium is deformed elastically, there are regions of stress on the left and right sides of the plot, where the pressures exceed the yield strength of lithium. Therefore, in these regions (notated as 'Plastic Region' in Figure 3.18), plastic deformation of the lithium at the negative electrode should occur.

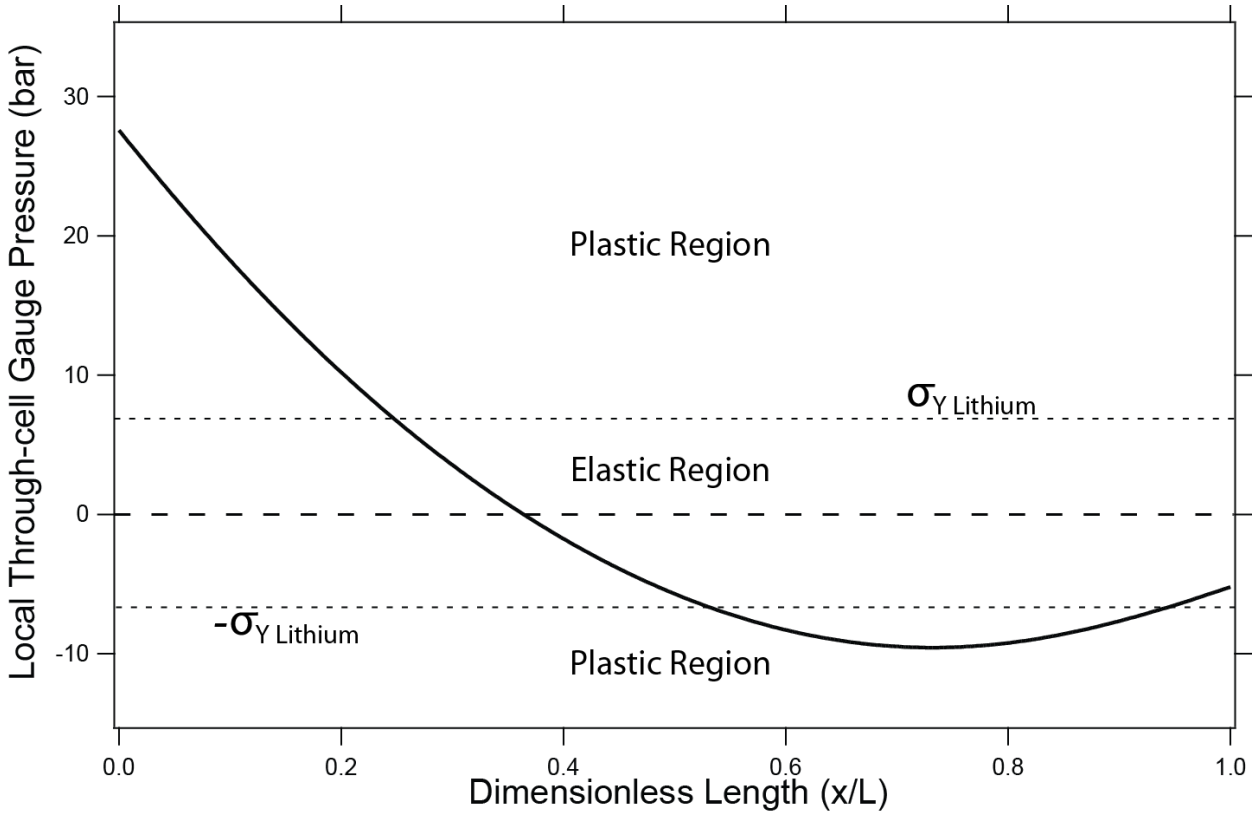

Figure 3.18. Pressure distribution along the lithium/separator interface immediately after a cycle consisting of a discharge, rest, then a charge at a C/2 rate to a 50% depth of discharge for a separator with an elastic modulus of 16 GPa, allowing for elastic deformation of the lithium (taken from the '16 GPa Rigid Lithium' line in Figure 3.17). The horizontal dashed lines represent the yield stress of lithium.

Before we include the equations for plasticity in the model developed in Chapter 1 and updated in Section 3.5, it is useful to get a basic understanding of how we expect the negative electrode to deform plastically under the stress profile seen in Figure 3.18. Therefore, a limit analysis of the problem, the foundation for which is detailed in Section A.5 of Appendix A, is employed.

If we simplify the problem at hand such that only plastic deformation is included, then we can also simplify Figure 3.18 to include only pressures above the yield strength of lithium. Therefore, we split Figure 3.18 into three sections: pressures above the compressive yield strength, pressures below the tensile yield strength, and pressures between the yield strengths.

This can be seen in Figure 3.19 below where vertical dashed lines are added to signify the regions where the pressure exceeds the yield strength of lithium. The region on the left, labeled 'Compressive Region,' is where the pressure exceeds the compressive yield strength of lithium, the region on the right, labeled 'Tensile Region,' is where the pressure exceeds the tensile yield strength of lithium, and the region in the middle, labeled 'No Pressure,' is where the pressure falls between the compressive and tensile yield strengths of lithium and only elastic deformation is expected to occur.

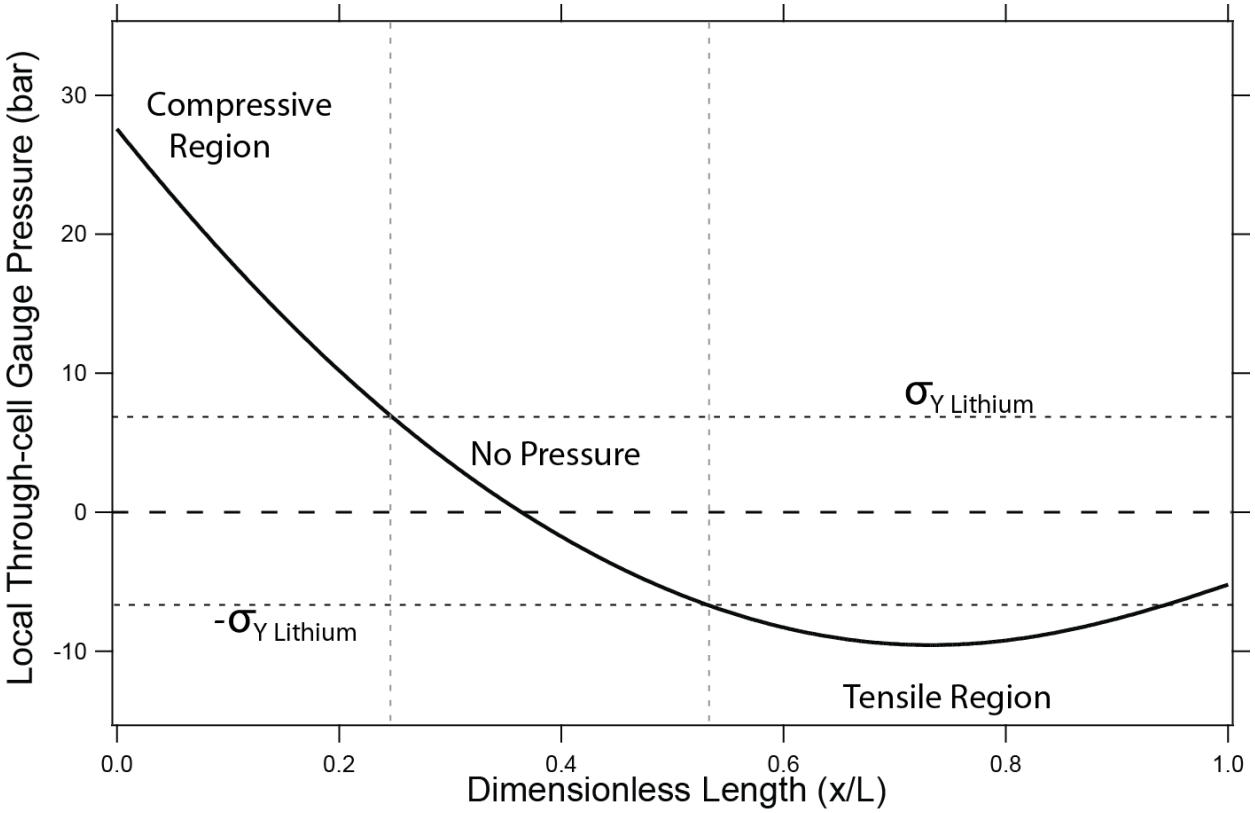

Figure 3.19. Pressure distribution along the lithium/separator interface immediately after a cycle consisting of a discharge, rest, then a charge at a C/2 rate to a 50% depth of discharge for a separator with an elastic modulus of 16 GPa allowing for elastic deformation of the lithium (taken from the '16 GPa Rigid Lithium' line in Figure 3.17). The horizontal dashed lines represent the yield stress of lithium, and the vertical lines divide the plot into the different pressure regions.

We now take this simplification to be an extension of the punch-indentation problem found in Section A.5 of Appendix A and find the upper-bound solution. Rather than have one punch being forced into the metal (as is seen in Figure A.3), we now have two punches, fixed to the metal, which have equal but opposite forces (see Figure 3.20a). The left punch, P_1, is compressed by pressure p, and the right punch, P_2, is in tension by pressure -p. With this

analysis, we can determine the stresses necessary to cause plastic deformation and gain an understanding of how we expect the lithium to deform.

If we consider the left punch only, punch P_1 is forced down, pushing triangle A down and to the right. This moves triangle B to the right, which forces triangle C up and to the right. If we now consider the right punch only, punch P_2 is forced up, which pulls triangle E up and to the right. This pulls triangle D to the right, which moves triangle C down and to the right. As we can see, Punch P_1 forces triangle C up and to the right, and punch P_2 forces triangle C down and to the right. The combination of both of these vectors results in triangle C moving directly to the right at the same rate as triangles B and C. This means that no shearing takes place between triangles B and C or C and D and triangles B, C, and D all move to the right.

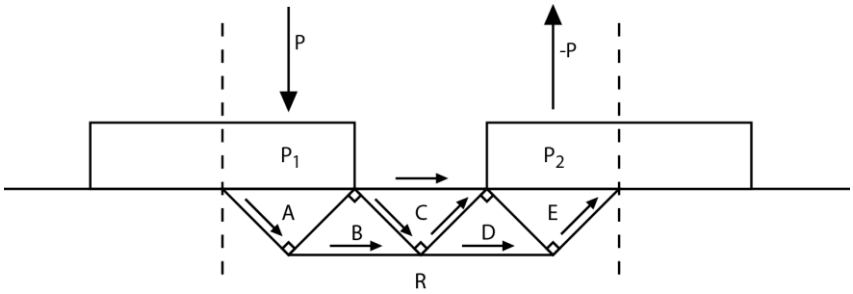

Figure 3.20. Displacement field of a continuation of the punch-indentation problem in Section A.5 of Appendix A. Here two closely spaced punches are forced into a metal (R) with opposite forces. This results in triangle C being forced to the right at the same rate as B and D.

The results of this analysis show us that plasticity can indeed be a factor at the pressures shown in Figure 3.18. Furthermore, we expect the lithium on the left to be deformed down toward the compressive yield strength of lithium line and the lithium on the right to be deformed up toward the tensile-yield-strength line. This flattens the negative electrode and limits the stress build up to that of the yield strength of lithium. More interestingly though, is that we expect, the lithium in the center of Figure 3.18, where the pressure falls between the yield strengths of lithium metal, to be deformed to the right, toward the region in tension.

With this preliminary analysis, we can now move forward to include the equations for plastic deformation, described in Section 3.4, into the model for lithium movement developed thus far.

3.7 Numerical Analysis of Plasticity in Lithium-metal Batteries

In Section 3.5 we included elastic deformation of the negative electrode as well as a stiff separator into the model created in Chapter 1. From that analysis we saw that, with a separator that could inhibit dendrite formation, significant elastic deformation of the negative electrode

occurred due to very high stresses. By comparing the stresses seen to the yield strength of lithium (Figures 3.18 and 3.19) we determined that the stresses in the lithium were well beyond the yield strength of lithium, where plastic deformation should occur. Therefore, in this section we include the plastic deformation of lithium, the equations for which were developed in Section 3.4, and determine the extent of the deformation and its effect on the cell.

3.7a Methods and Assumptions

We now set up the equations for calculating numerically the plastic deformation of lithium in the negative electrode. There is a general lack of data on the mechanical properties of lithium metal; therefore, we make the general assumption that lithium metal behaves as a normal ductile metal. We now give a summary of the material learned thus far that is particularly relevant to the subject of plastic deformation in the hope that the reader gains a further understanding of the equations solved in this Section to determine the plastic and elastic deformation of lithium metal.

Solid mechanics can be considered part of the field of rheology and is closely related to fluid mechanics, involving Newtonian, non-Newtonian, and viscoelastic fluids. These are very complicated, and a complete and accurate mathematical description is probably not possible.

The momentum balance applies to all these fluids. It can be written as

$$\rho\left(\frac{\partial \underline{v}}{\partial t} + \underline{v}\cdot\nabla\underline{v}\right) = -\nabla\cdot\underline{\underline{\sigma}} + \rho\underline{g}. \tag{3.110}$$

Even this is incomplete; for example, the electric force on a nonelectrically neutral medium is neglected.

For many applications, particularly in plasticity, the inertial terms (on the left) and the gravitational term are neglected. This is partly an attempt to get down to a tractable formulation. The equation to solve is then

$$\nabla\cdot\underline{\underline{\sigma}} = 0. \tag{3.111}$$

The continuity equation is generally applicable as

$$\frac{\partial \rho}{\partial t} + \underline{v}\cdot\nabla\rho = -\rho\nabla\cdot\underline{v}. \tag{3.112}$$

This may be simplified to an equation of incompressibility:

$$\nabla \cdot \underline{v} = 0. \tag{3.113}$$

A really complex problem is to relate $\underline{\underline{\sigma}}$ to other physical quantities in the problem, such as the velocity gradient $\nabla\underline{v}$, the deformation of the particles $\underline{u}$, and the history of the material, such as the stress that it has been subjected to. In solid mechanics, the gradient of the deformation vector $\nabla\underline{u}$ also describes the state of strain in the material.

The mathematics of solid mechanics is similar to that of fluid mechanics. From the gradient of the displacement vector $\nabla\underline{u}$, we can construct a symmetric tensor called the infinitesimal strain tensor,

$$\underline{\underline{\epsilon}} = \frac{1}{2}\left[\nabla\underline{u} + (\nabla\underline{u})^{T}\right], \tag{3.114}$$

where the factor of 1/2 was introduced historically. Otherwise, the rate of deformation tensor $\dot{\underline{\underline{\epsilon}}}$ is simply related to the strain tensor:

$$\dot{\underline{\underline{\epsilon}}} = \frac{\partial \underline{\underline{\epsilon}}}{\partial t}. \tag{3.115}$$

A general property of the stress is that it is symmetric,

$$\underline{\underline{\sigma}} = \underline{\underline{\sigma}}^{T} \quad \text{or} \quad \sigma_{ij} = \sigma_{ji}. \tag{3.116}$$

Any symmetric tensor can be diagonalized by a rotation of the coordinate system. This rotated coordinate system defines the principal axis of stress; in this coordinate system, the off diagonal elements of $\underline{\underline{\sigma}}$ are zero, and there are only normal stresses. If the three normal stresses are equal we have a situation of hydrostatics, where a material element can be compressed, but is not distorted. If these three normal stresses are not equal, there is a driving force for distortion of a material element.

A substantial simplification for fluids occurs if the system is isotropic and fluid properties are not dependent on the history of the fluid. Then $\underline{\underline{\sigma}}$ depends on the velocity gradient, and the relationship must be able to be expressed in a proper vectorial (or tensorial) relationship, which means that it is valid in any coordinate system.

Again, $\underline{\underline{\sigma}}$ is symmetric, as stated previously. There are two relevant symmetric tensors, the rate of deformation $\nabla\underline{v} + (\nabla\underline{v})^{T}$ and the unit tensor $\underline{\underline{I}}$. The sought constitutive equation can be expressed as

$$\underline{\underline{\sigma}} = -\eta\left[\nabla\underline{v} + (\nabla\underline{v})^{T}\right] + K\underline{\underline{I}}, \tag{3.117}$$

where η and K are scalar funtions of relevant properties. These properties include the temperature, pressure, and composition of the material, and composition of the material as well as the scalar invariants of the tensor $\nabla\underline{v}$. These relevant invariants are $\nabla \cdot \underline{v}$ and $(\nabla\underline{v}) : (\nabla\underline{v})$. Frequently, η is taken to be an arbitrary function of $\underline{\underline{\dot{\epsilon}}} : \underline{\underline{\dot{\epsilon}}}$ (the functional dependence being defined by the particular fluid).

For a Newtonian fluid, ηand K are chosen so that

$$\underline{\underline{\sigma}} = -\mu\left[\nabla\underline{v} + (\nabla\underline{v})^{T}\right] + \left(\frac{2}{3}\mu - \tilde{\kappa}\right)\underline{\underline{I}}\,\nabla \cdot \underline{v} + p\underline{\underline{I}}, \qquad 3.118$$

so that $\underline{\underline{\sigma}}$ depends linearly on first velocity derivatives and μ and $\tilde{\kappa}$ are physical properties ($\tilde{\kappa}$ is the dilatation viscosity notated with a tilde to distinguish it from κ, the shear yield strength) dependent on temperature, pressure, and composition and p is the thermodynamic pressure of the local fluid element. η and K (and p) are independent of the velocity derivatives.

For a non-Newtonian fluid η and (in principle) K can depend nonliearly on velocity derivatives. Worse yet, there are viscoelastic fluids where η and K can depend on the previous stress history of the fluid.

For an elastic solid, the stress $\underline{\underline{\sigma}}$ is related to the deformation through

$$\underline{\underline{\sigma}} = \frac{E}{(1+\nu)}\underline{\underline{\epsilon}} + \frac{E\nu}{(1+\nu)(1-2\nu)}\,\mathrm{tr}(\underline{\underline{\epsilon}})\underline{\underline{I}}, \qquad 3.33$$

in a manner very similar to the stress relation for a Newtonian fluid. E is a physical parameter called the Young's modulus, dependent on temperature, pressure, and composition, but independent of $\underline{\underline{\epsilon}}$. The Poisson's ratio ν is another physical property, equal to 1/2 for an incompressible material and 0 for an ideally elastic material (where the material can stretch in one direction without decreasing in the transverse direction).

For a Hookian elastic solid, one has the momentum equation, the continuity equation, and Hooke's law relating $\underline{\underline{\sigma}}$ to $\underline{\underline{\epsilon}}$. With sufficient boundary conditions, one can solve problems in elastic mechanics.

However, if enough stress is applied to an elastic solid, the material will eventually begin to flow or deform plastically. When the stress is removed, the solid will not relax to its original shape.

First, we should understand that a uniform compression (or tension) does not generally lead to a distortion of shape. Consequently, we construct an effective stress which, in principal axes, depends on difference in normal stresses:

$$\bar{\sigma} = \left\{\frac{1}{2}[(\sigma_1 - \sigma_2)^2 + (\sigma_2 - \sigma_3)^2 + (\sigma_3 - \sigma_1)^2]\right\}^{\frac{1}{2}} \quad 3.21$$

Since this is a scalar invariant, it can be expressed in any coordinate system.

$$\bar{\sigma} = (3J_2)^{\frac{1}{2}} = \left(\frac{3}{2}\underline{\underline{S}} : \underline{\underline{S}}\right)^{\frac{1}{2}} = (I_1^2 + 3I_2)^{\frac{1}{2}}. \quad 3.22$$

Thus, a solid is likely to behave elastically until a certain yield stress is reached. Beyond this, it essentially becomes a non-Newtonian fluid.

The situation has now become quite complicated and simplifications become necessary. Similar to non-Newtonian fluids (and turbulence) we may impose a condition of incompressibility. To jump way ahead, we should anticipate that most plastic flow situations are treated by solving the momentum and continuity equations and let the material flow until, with a combination of increase of equivalent strain ($\bar{\epsilon}$) and a decrease of equivalent stress ($\bar{\sigma}$), the material again reaches a condition where the equivalent stress ($\bar{\sigma}$) is equal to or drops below the yield stress σ_Y.

This is not so simple, because now the yield stress can depend on the history of the stress and strain of the material. This increase of σ_Y toward the ultimate strength of the material is called work hardening.

In this complicated situation we need experimental data. For this we study the uniaxial stress test (refer to Section 3.2c) which we generalize to multiaxial loading (refer to Section 3.2d) through the use of the equivalent stress and equivalent strain. For the case of lithium, the uniaxial stress-strain curve can be seen in Figure 3.21.

For plastic flow, we still use Equation 3.117 choosing η and K such that the stress is related to the rate of deformation $\underline{\underline{\dot{\epsilon}}}$ through

$$\underline{\underline{\dot{\epsilon}}} = \frac{1}{2\eta}\langle 1 - \frac{\kappa}{\sqrt{J_2}}\rangle \underline{\underline{S}} \quad 3.119$$

where $\underline{\underline{S}} = \underline{\underline{\sigma}} - p\underline{\underline{I}}$, p is the hydrostatic pressure, κ is the shear yield strength, J_2 is the second invariant of the stress deviator (defined in Equation 3.10), and η is a function of $\underline{\underline{\dot{\epsilon}}} : \underline{\underline{\dot{\epsilon}}}$.[20] In Equation 3.119, the brackets are defined such that:

$$\langle x\rangle = \begin{cases} 0, & \text{if } x \leq 0 \text{ and} \\ x, & \text{if } x \geq 0 \end{cases} \quad 3.120$$

We can relate Equation 3.119 to the multiaxial stress-strain curve (seen in Figure 3.9 below) through Equation 3.21

$$\bar{\sigma} = \sqrt{3J_2} \tag{3.21}$$

and Equation 3.41

$$\kappa = \frac{\sigma_Y}{\sqrt{3}}. \tag{3.41}$$

Equation 3.119 can now be described as

$$\dot{\underline{\underline{\epsilon}}} = \frac{1}{2\eta}\langle 1 - \frac{\sigma_Y}{\bar{\sigma}}\rangle \underline{\underline{S}} \tag{3.121}$$

where $\bar{\sigma}$ is the equivalent stress and σ_Y is the tensile yield strength. We can now imagine the stress-strain plot (such as the one in Figure 3.9 repeated below for clarity) as a steady-state line. If the equivalent stress $\bar{\sigma}$ is at or below the current yield stress σ_Y then yielding does not occur. However, if we increase the stress to above the yield stress, we are above the stress-strain curve and the material deforms. With sufficient boundary conditions and with knowledge of η (a function of $\dot{\underline{\underline{\epsilon}}} : \dot{\underline{\underline{\epsilon}}}$) for the specific material, we can solve Equation 3.121 along with the momentum equation and the continuity equation to determine the plastic deformation of a material.

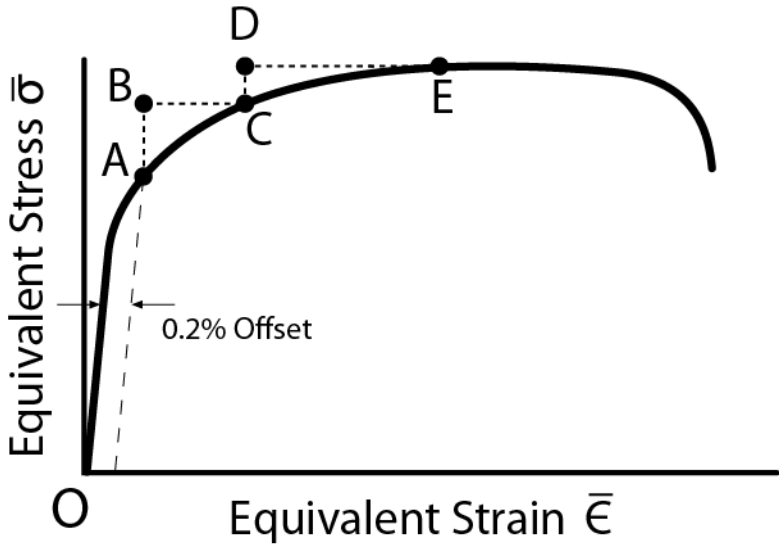

Figure 3.9. Equivalent stress versus equivalent strain for an example material at a very low rate of strain such that the solid line can be thought of as steady state. Point A represents the 0.2% yield stress and point C and E, equilibrium points where the stress equals the yield stress and the stress can be maintained without further deformation occurring. Points B and D represent points away from equilibrium where the stress exceeds the yield stress of the material and deformation occurs.

However, one further simplification that is often made is that of time-independent deformation. As the rate at which we strain the material becomes slower and slower, we get closer to equilibrium. At slow enough rates, we can say that the process has become time independent meaning that, by changing the rate at which we stress the material (or, equivalently, the rate at which we strain the material), we do not deviate appreciably from the steady-state stress-strain curve. To implement the time-independent assumption into Equation 3.119 or 3.121, we take the double dot product $\dot{\underline{\underline{\epsilon}}} : \dot{\underline{\underline{\epsilon}}}$ of Equation 3.118 giving us

$$\eta\sqrt{2(\dot{\underline{\underline{\epsilon}}} : \dot{\underline{\underline{\epsilon}}})} = \sqrt{J_2} - \kappa. \tag{3.122}$$

(The algebra leading from Equation 3.119 to 3.122 can be found in Section A.5 of Appendix A.) Substituting this into Equation 3.119 gives us

$$\dot{\underline{\underline{\epsilon}}} = \langle \frac{\sqrt{\dot{\underline{\underline{\epsilon}}} : \dot{\underline{\underline{\epsilon}}}}}{\sqrt{\underline{\underline{S}} : \underline{\underline{S}}} \rangle \underline{\underline{S}} = \langle \dot{\lambda} \rangle \underline{\underline{S}} \tag{3.123}$$

where $\dot{\lambda} = \mathrm{d}\lambda/\mathrm{dt}$. If we neglect the elastic component of the strain and assume that we are always in the plastic regime, then we can remove the brackets from Equation 3.123 giving us the Levy-Mises theory of plasticity. Multiplying Equation 3.123 by dt gives us the Prandtl-Reuss equations:

$$\mathrm{d}\underline{\underline{\epsilon}}^{\mathrm{p}} = \sqrt{\frac{\mathrm{d}\underline{\underline{\epsilon}}^{\mathrm{p}} : \mathrm{d}\underline{\underline{\epsilon}}^{\mathrm{p}}}{\underline{\underline{S}} : \underline{\underline{S}}}} \underline{\underline{S}} = \frac{3}{2} \frac{\mathrm{d}\bar{\epsilon}^{\mathrm{p}}}{\sigma_{\mathrm{Y}}} \underline{\underline{S}}. \tag{3.55}$$

(For a more detailed explanation of the application of the time independent assumption to Equation 3.119, please refer to the “The Transition from Rate-Dependent to Rate-Independent Plasticity” Subsection in Section 3.4c.)

We can use uniaxial stress-strain data seen in Figure 3.21 below (generalized to multiaxial through the use of equivalent stress $\bar{\sigma}$ and equivalent strain $\bar{\epsilon}$) to determine the scalar function $\mathrm{d}\bar{\epsilon}^{\mathrm{p}}/\sigma_{\mathrm{Y}}$. With the boundary conditions listed below, we solve numerically the momentum equation, the continuity equation, and Equation 3.55 relating the incremental plastic strain $\mathrm{d}\underline{\underline{\epsilon}}^{\mathrm{p}}$ to the deviatoric stress $\underline{\underline{S}}$.

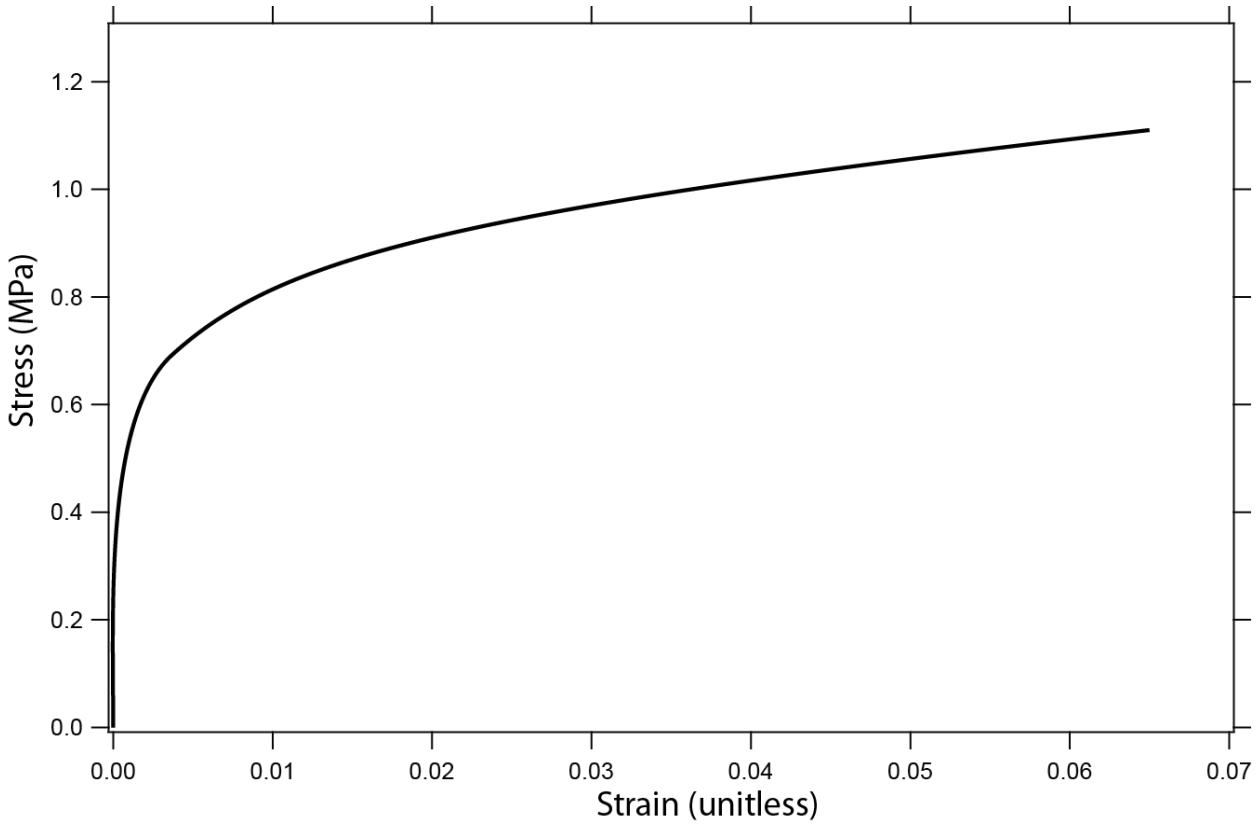

Figure 3.21. Stress-strain curve for lithium under uniaxial loading as taken from "Li Material Testing -Fermilab Antiproton Source Lithium Collection Lens."[32] Here, the initial 0.2% offset yield strength is 6.55 bar.

Now that we have an equations necessary, let us determine the boundary conditions in the lithium metal. We use the same model geometry as was used in Chapters 1, 2, and Section 3.5, which can be seen in Figure 3.10. Since the model is two dimensional in the x and y dimension, we neglect all stresses and strains in the z direction, significantly simplifying the problem. We assume that the sides of the electrode deform only in the y direction and that the bottom of the negative electrode does not deform in the y-direction but can slide, frictionlessly in the x direction. That is to say, we assume that there is some sort of frictionless packaging around the cell such that the lithium will not squeeze out the sides if under compression and is supported along the bottom. Thus,

$$\epsilon_{11} = 0 \quad \text{at} \quad \frac{\mathrm{x}}{\mathrm{L}} = 0 \text{ and } \frac{\mathrm{x}}{\mathrm{L}} = 1 \tag{3.124}$$

and

$$\epsilon_{22} = 0 \quad \text{at} \quad \mathrm{y} = 0 \text{ (bottom of the negative electrode).} \tag{3.125}$$

Because the forces at the interface must balance, at the boundary between the lithium and the separator the deformation of the lithium is equal to the deformation of the separator and we set the stress in the lithium equal to the stress in the separator through

$$\sigma_{22} = \sigma_{22_{\mathrm{Sep}}} \tag{3.126}$$

where σ_{22} is the stress in the y-direction in the lithium and $\sigma_{22_{\mathrm{Sep}}}$ is the stress in the separator due to its deformation.

With the model of the separator as a series of ideal springs, the separator only deforms elastically with a Poisson's ratio of zero. Because of the high aspect ratio, it is appropriate to set certain σ_{ij}'s and ignore others. Therefore to determine the change in pressure in the separator due to its deformation, we use Hooke's law such that

$$\sigma_{22_{\mathrm{Sep}}} = \mathrm{E}_{\mathrm{Sep}}\epsilon_{22_{\mathrm{Sep}}} = \mathrm{E}_{\mathrm{Sep}}\frac{\Delta \mathrm{y}_{\mathrm{Sep}}}{\mathrm{y}^{0}_{\mathrm{Sep}}}. \tag{3.127}$$

Here $\mathrm{E}_{\mathrm{Sep}}$ is the elastic modulus of the separator and $\epsilon_{22_{\mathrm{Sep}}}$ is the deformation of the separator in the y-direction. Because the separator is assumed to be perfectly elastic and the deformations of the separator are small compared to the thickness of the separator, the local deformation of the separator in the y-direction can be calculated by dividing the local change in the thickness of the separator by the initial thickness or $\Delta \mathrm{y}_{\mathrm{Sep}}/\mathrm{y}^{0}_{\mathrm{Sep}}$.

Let us now turn to the elastic portion of the strain in the lithium metal. To relate the stress to the elastic deformation in the lithium metal, we take Equation 3.35 from Section 3.3b, which is the matrix form of the inverted generalized Hooke's law and is repeated below for clarity:

$$\underline{\underline{\epsilon}}^{\mathrm{e}} = \frac{1}{\mathrm{E}}\{\underline{\underline{\sigma}} - \nu[\mathrm{tr}(\underline{\underline{\sigma}})\underline{\mathrm{I}} - \underline{\underline{\sigma}}]\}. \tag{3.35}$$

We use the same boundary conditions as for the plastic deformation (Equations 3.124 through 3.126). Again, the deformation in the x-direction is set to zero at left and right edges of the lithium (Equation 3.124). At the bottom boundary of the negative electrode the deformation in y-direction is zero (Equation 3.125), and, at the negative electrode/separator interface, the stress in the lithium in the y-direction is equivalent to the change in pressure due to the deformation of the separator (Equation 3.126).

The deformation, calculated through Equations 3.55 and 3.35, now modifies the thickness of the lithium determined through the electrochemical model developed in Chapter 1. The stress at the boundary is determined by Equations 3.55 and 3.127. These equations solve

for the mechanical deformation of the lithium at the negative electrode and, when implemented into the model developed in Chapter 1, the movement of lithium during cycling with a very-stiff separator can be determined.

3.7b Results and Discussion

Let us now look at how the incorporation of a very stiff separator deforms the negative electrode. In Figure 3.22 below we see the results of the simulation after a full cycle of a discharge, rest, and charge. The simulations were run at a C/5 rate to a 10 percent depth of discharge based on the positive electrode. The dashed line, labeled 'Movement with Pliable Separator' represents the movement of lithium immediately after charge with a pliable separator that does not resist the movement of lithium. This line is simply used as a comparison for the case with a very stiff separator. The solid line, labeled 'Movement with a Stiff Separator' represents a simulation run under the same conditions at the 'Movement with Pliable Separator' simulation (that is at a C/5 rate to a 10 percent depth of discharge), with a very stiff, dendrite-inhibiting separator (16 GPa).

As we can see from the 'Stiff-Separator' case, the very stiff separator (16 GPa) has caused significant deformation to occur. As expected from Figures 3.18 and 3.19, plastic deformation has occurred at the left and right sides of the negative electrode, where the line is flat, and only elastic deformation has occurred in the middle of the negative electrode where the profile is sloped. These plastic and elastic deformation zones can be seen better if the stress were somehow to be relaxed in the negative electrode as is seen in the 'Stress-Relaxed' line in Figure 3.22. Here, the elastic deformation that occurred in the middle of the negative electrode has recovered to its original profile. The elastic portions of the deformation in the left and right sides of the graph have also recovered when the stress was relaxed; however, the plastic or irreversible portion of the deformation has not recovered, leading to a flat profile.

To explain the mechanism for this plastic deformation, during charge the lithium is deposited more on the left than on the right, leading to a build-up of lithium. As the lithium starts to build up on the left, the compressive stresses also start to build due to the lithium displacing the very stiff separator. Eventually the stresses will build to a point where the compressive yield strength of lithium is reached. As more lithium is deposited on the left side, it yields such that the stress in the left side of the negative electrode is maintained at the compressive yield strength. This means that as more lithium is deposited at the left side, it is deformed such that the height remains the same. These results are quasi-steady, where enough time has passed to permit this flow.

On the right side of the negative electrode a similar mechanism occurs where the lithium is deposited more slowly than on the left such that the local thickness of the lithium on the right side is less than the average thickness of the lithium thereby creating a region of

tension. As the charge progresses, the stresses reach the tensile yield strength of lithium, and the lithium yields.

Even though the deformation of the separator applies pressure in the y-direction, both the elastic and plastic deformation of the lithium causes stresses to build-up in the x-direction as well. This can be seen for the case of elastic deformation through inspection of Equation 3.35. In Equation 3.35 we see that a stress in one direction (such as the y-direction) causes strains not only in that direction, but also in the perpendicular directions (such as the x-direction) that are proportional to ν/E. In plastic deformation, the same effect holds true where the material deformed pushes other material out of the way leading to stresses in that direction, such as in the limit analysis in Section 3.6.

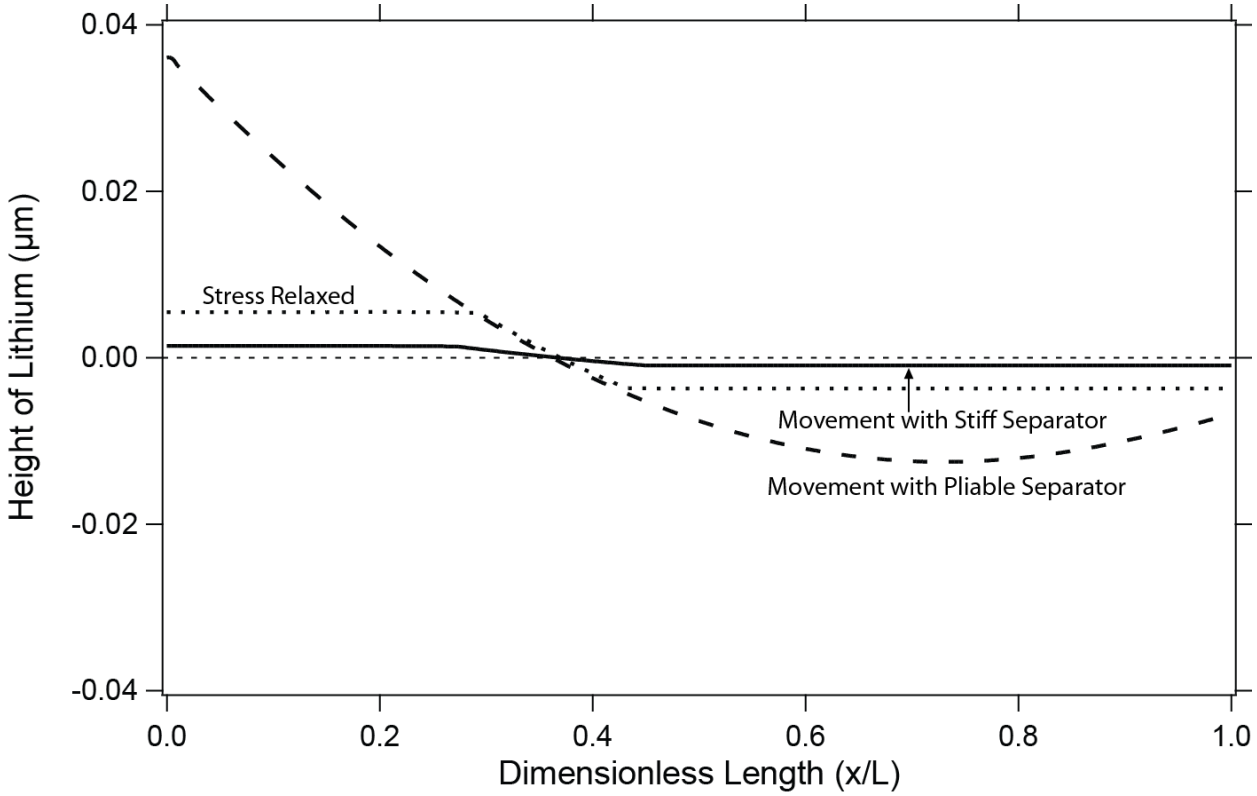

Figure 3.22. Height of the lithium negative electrode along the lithium/separator interface after a cycle consisting of a discharge, rest, then a charge at a C/5 rate to a 10 percent depth of discharge. The dashed, 'Movement with Pliable Separator' line includes a separator that does not resist movement of the lithium. The solid, 'Movement with Stiff Separator' line includes a very stiff, dendrite-inhibiting separator (16 GPa), and the dotted, 'Stressed-Relaxed' line, is the height of the lithium with a very stiff separator if the stress were somehow relaxed.

In Figure 3.23 below, we see the pressure on the separator measured in bar after a charge. This pressure is due to the movement of the lithium deforming the very stiff (16 GPa) separator. From this plot we see, as would be expected, a flat maximum and minimum where the profile of the lithium is flat due to plastic deformation. When comparing the pressures seen in Figure 3.23 to Figures 3.13 or 3.16, we can see that the plastic deformation of the lithium at the negative electrode has significantly reduced the stresses.

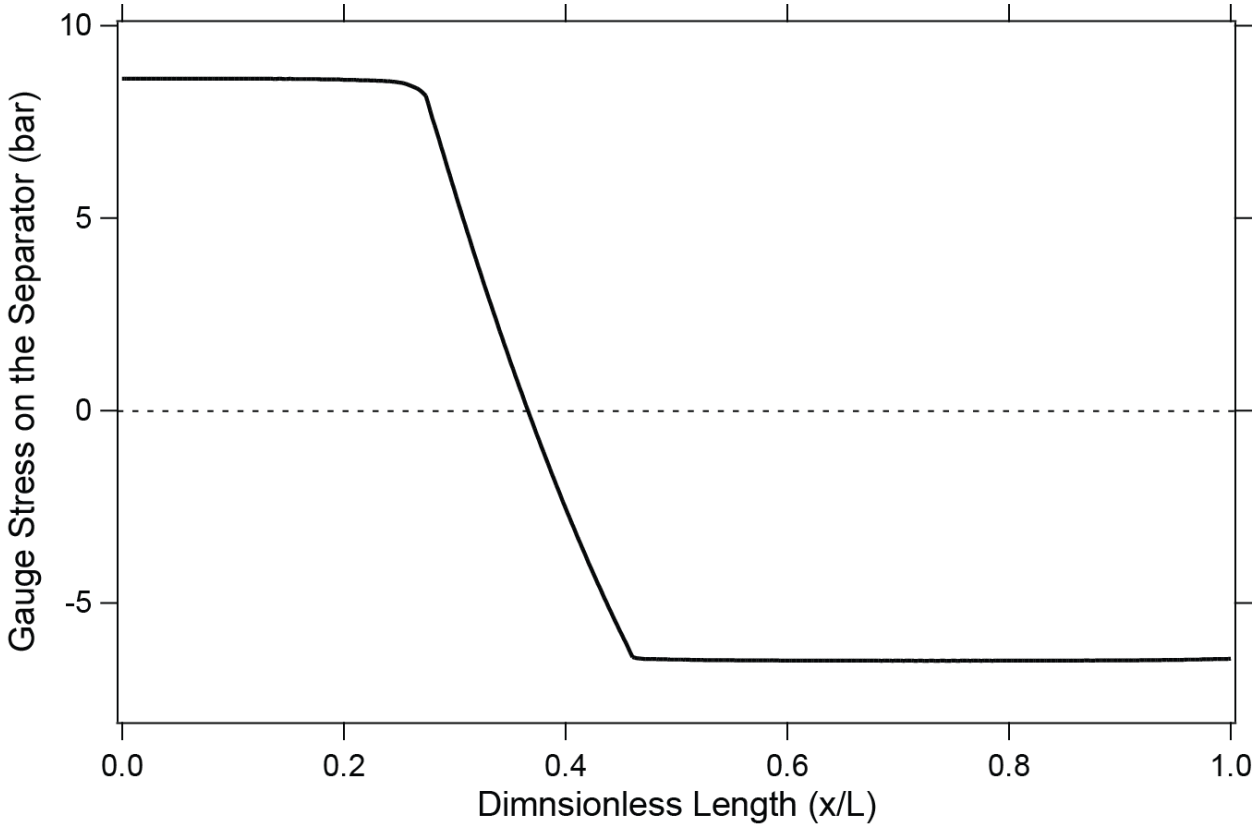

Figure 3.23. Gauge stress on the separator measured in bar after charge with a very stiff separator (16 GPa) caused by the movement of the lithium negative electrode.

Let us next turn our attention to the movement of lithium during the cycle. Figure 3.24 shows the profile of lithium after discharge at a C/5 rate to a 10 percent depth of discharge. As seen in Chapters 1 and 2, with a pliable separator the profile of the lithium is concave down. With a stiff separator, the lithium is deformed substantially from the pliable separator case, with plastic deformation occurring on the left and right sides of the negative electrode and elastic deformation occurring in the middle. As the cell is discharged, more lithium is removed from the left side of the cell than the right, causing tensile stresses to build on the left and compressive stresses on the right. Once the stresses build to the yield strength of lithium, plastic deformation occurs such that the lithium is deformed toward the region in tension. This

causes the lithium to flatten and the profile to be similar to that seen in Figure 3.22, but opposite due to the fact that the cell is being discharged rather than charged.

The more interesting phenomenon, however, occurs during rest. In Chapter 1 we learned that during rest the concentration of lithium in the solid phase of the positive electrode equilibrates during rest by interacting with the negative electrode. After discharge, for example, the positive electrode equilibrates by depositing lithium on the left side of the negative electrode and stripping lithium from the right. This phenomenon also occurs with a very stiff separator, as is seen in Figure 3.25 below. By comparing the 'Movement with Pliable Separator' lines in Figures 3.23 and 3.24, we see that the equilibration of the positive electrode has resulted in a flattening out of the negative electrode through deposition on the left and stripping on the right. However, when comparing the 'Movement with Stiff Separator' lines in Figures 3.24 and 3.25 below, we see that the equilibration of the positive electrode has caused the lithium to build up such that the height of lithium is now positive on the left and negative on the right. This is, again, due to the equilibration of the positive electrode where, during rest, lithium was deposited on the left and stripped from the right. Because the lithium started out fairly uniform due to the plastic deformation, only a small amount of lithium being deposited on the left was required for the height to become positive. This, again, caused the stresses in the negative electrode to build beyond the yield strength of the lithium and plastic deformation to occur, thereby limiting the overall change in the height of the lithium during rest, but still allowing the positive electrode to equilibrate.

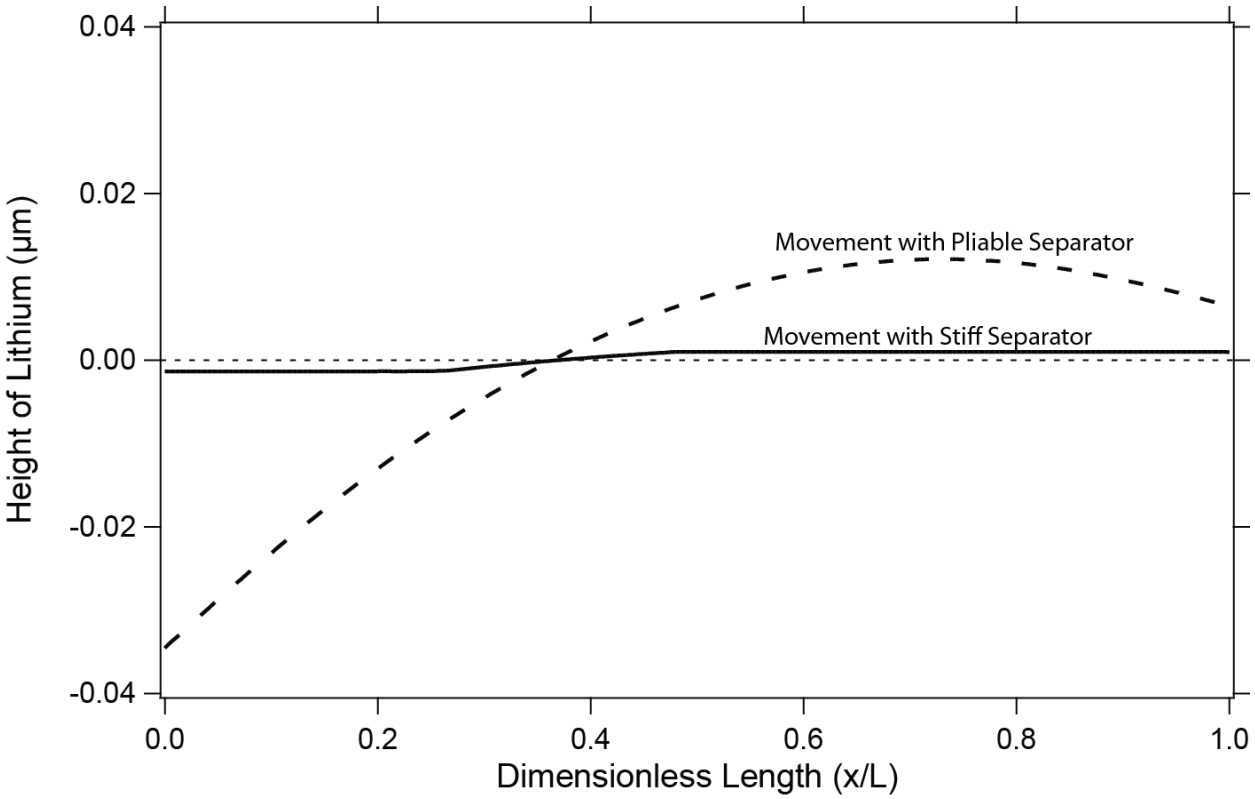

Figure 3.24. Height of the lithium negative electrode along the lithium/separator interface at the end of discharge at a C/5 rate to a 10 percent depth of discharge. The dashed, 'Movement with Pliable Separator' line includes a separator that does not resist movement of the lithium, and the solid, 'Movement with Stiff Separator' line includes a very stiff, dendrite-inhibiting separator with an elastic modulus of 16 GPa.

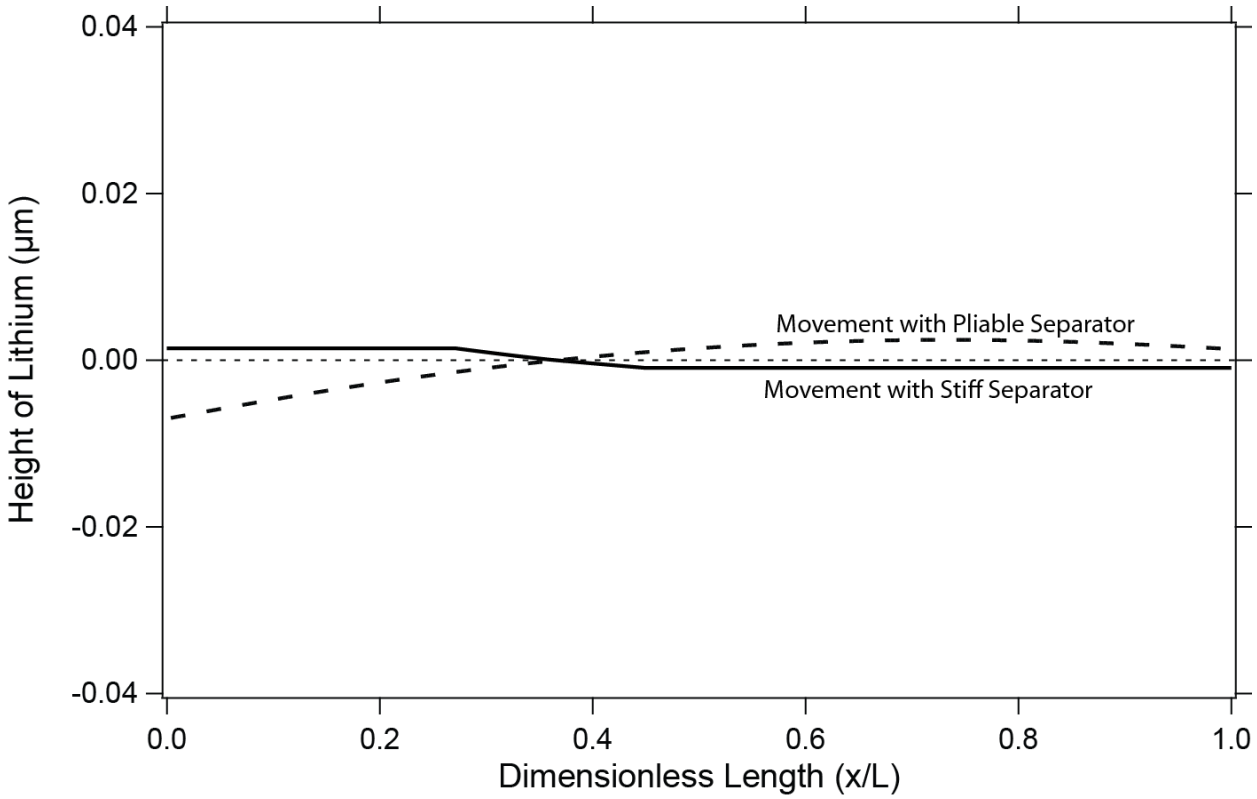

Figure 3.25. Height of the lithium negative electrode along the lithium/separator interface after resting for 1,000 seconds following a discharge at a C/5 rate to a 10 percent depth of discharge. The dashed, 'Movement with Pliable Separator' line includes a separator that does not resist movement of the lithium and the solid, 'Movement with Stiff Separator' line includes a very stiff, dendrite-inhibiting separator with an elastic modulus of 16 GPa.

After discharging and then resting, we charge the cell, the result of which can be seen in Figure 3.22 above. During rest, because of the equilibration of the positive electrode, the lithium built up so that the height is positive on the left and negative on the right. Furthermore, the stresses in the negative electrode have already reached the yield strength of lithium such that plastic deformation occurred. This means that, during charge, lithium is continuing to be deposited on the negative electrode, with more lithium deposited on the left than the right, but, due to the plastic deformation of the lithium, the profile stays relatively similar during charge such that the height profile after charge (seen in Figure 3.22) is very similar to the height profile after resting as seen in Figure 3.25.

Finally, in Figure 3.26 below, we look at the lithium after the rest following the charge. Again, the equilibration of the positive electrode causes lithium to be stripped from the left side of the cell and deposited on the right, leading to a flattening of the negative electrode relative to the pliable separator case. Similar to what occurred during the rest phase after discharge

with the stiff-separator case, after charge the stripping of the lithium from the left causes the height of lithium to become negative on the left, and the deposition of lithium on the right causes the height of lithium to become positive on the right.

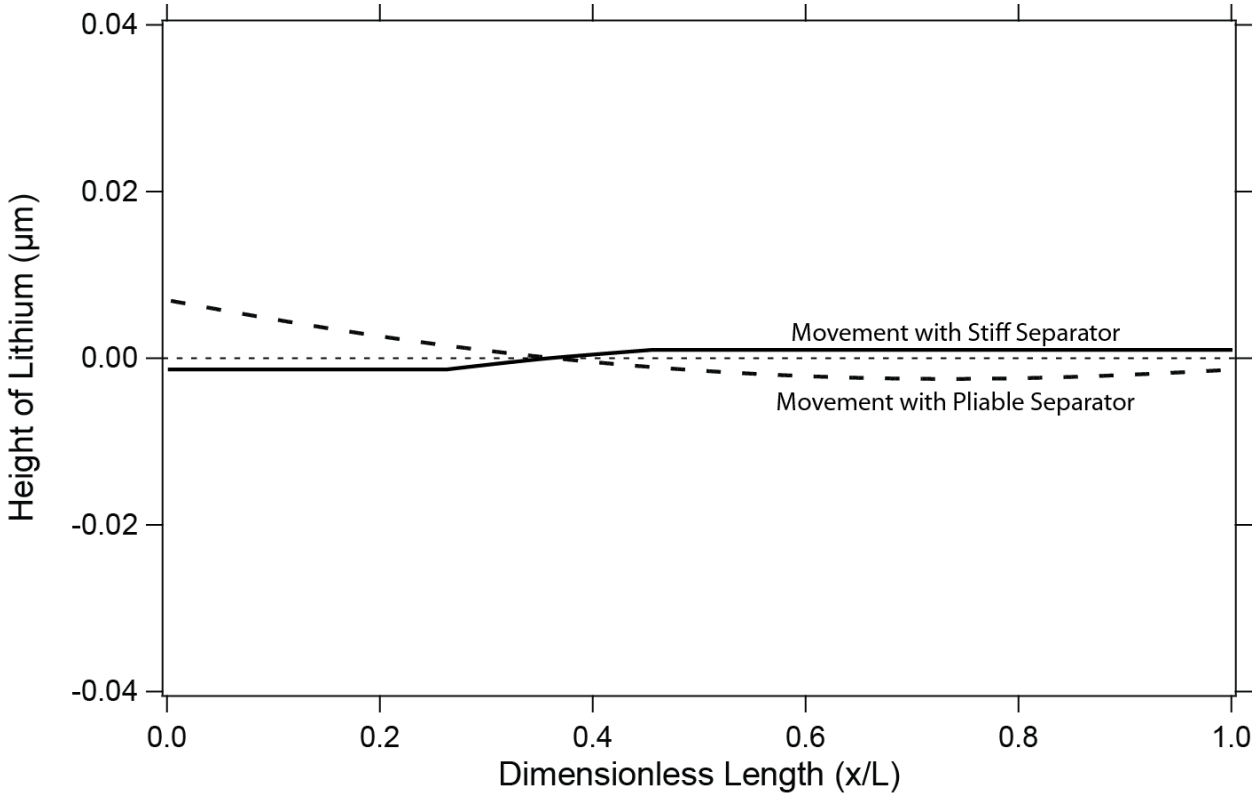

Figure 3.26. Height of the lithium negative electrode along the lithium/separator at the end of a full cycle consisting of a discharge, rest, charge, and rest at a C/5 rate to a 10 percent depth of discharge. The thick, dashed, 'Movement with Pliable Separator' line includes a separator that does not resist movement of the lithium, and the solid, 'Movement with Stiff Separator' line includes a very stiff, dendrite-inhibiting separator with an elastic modulus of 16 GPa.

Effect of a Very Stiff Separator on the State of Charge in the Positive Electrode

From Figures 3.21 through 3.25, we see that a very stiff separator (16 GPa) causes the height of the lithium at the negative electrode to remain substantially more uniform than with a very pliable separator. This is due to stresses building up beyond the yield strength of lithium, causing elastic and plastic deformation to occur, which deforms the lithium back toward uniform. We now turn our attention to how this more uniform lithium profile affects the positive electrode, primarily the state of charge.

For comparison we look at two limiting cases. Both cases were run at a C/5 rate to a 10 percent depth of discharge based on the positive electrode, and the only difference between the two cases is the strength of their separators. First, in Figure 3.27 we see the state of charge in the positive electrode after charge with a liquid electrolyte. Because the liquid does not resist the movement of the lithium at all, the profile of the lithium at the negative electrode will be at its most extreme for the given charge rate and depth of discharge. On the other extreme, in Figure 3.27, we see the state of charge of the positive electrode after charge with an infinitely stiff separator such that the height of the lithium at the negative electrode stays almost perfectly uniform throughout the cycle. Through the comparison of Figures 3.27 and 3.28, we see that the state of charge for the two extremes looks nearly the same. This leads us to the conclusion that the more uniform lithium profile caused by a very stiff separator has a very small effect on the state of charge of the positive electrode.

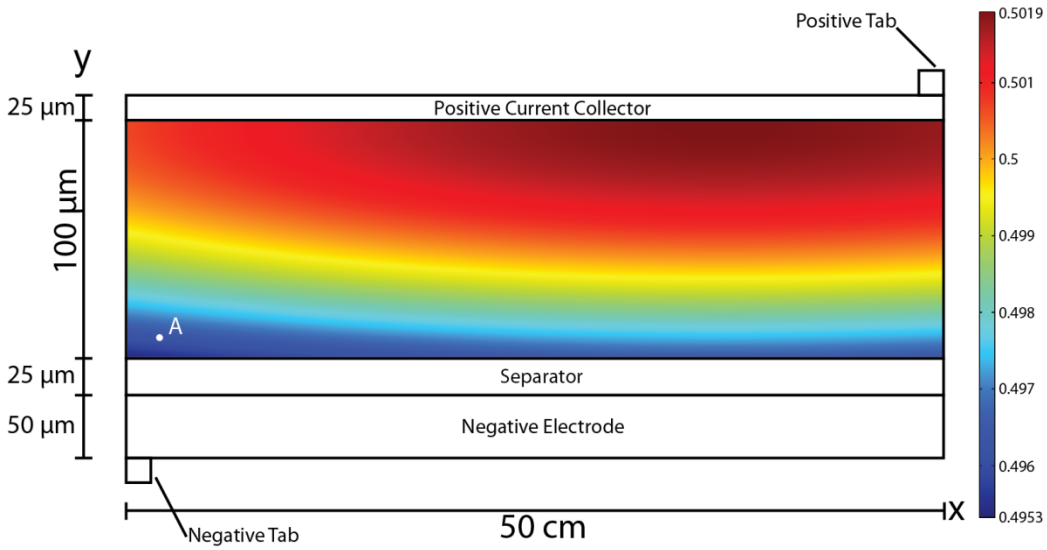

Figure 3.27. State of charge of the positive electrode at the end of charging after a cycle consisting of a discharge, rest, and charge at a C/5 rate to a 10 percent depth of discharge based on the positive electrode. The separator is a liquid electrolyte that does not inhibit the movement of lithium at the negative electrode.

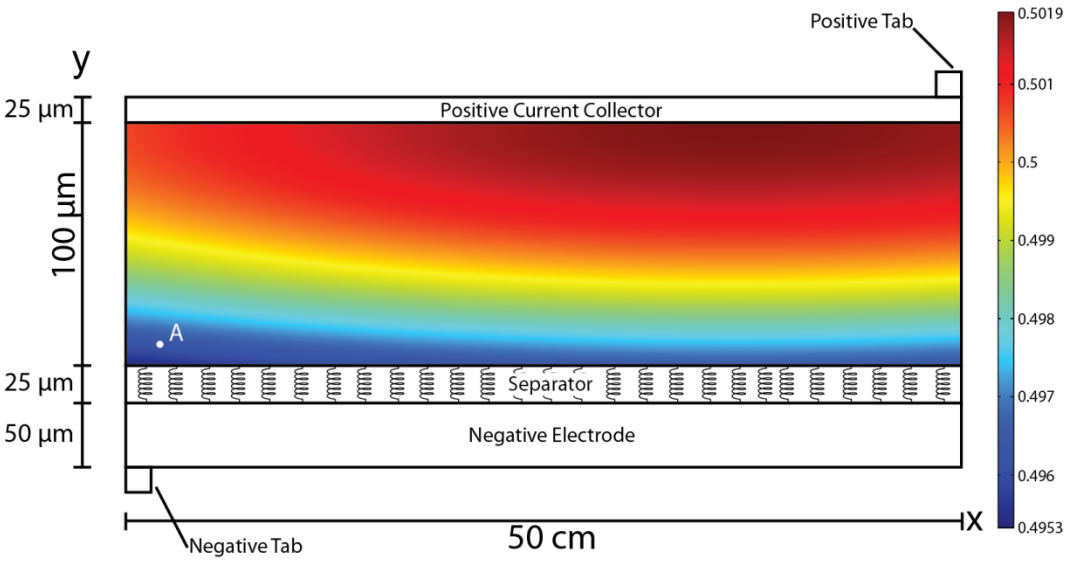

Figure 3.28. State of charge of the positive electrode at the end of charging after a cycle consisting of a discharge, rest, and charge at a C/5 rate to a 10 percent depth of discharge based on the positive electrode. The shear modulus of the separator is infinite such that the profile of the lithium is almost exactly uniform.

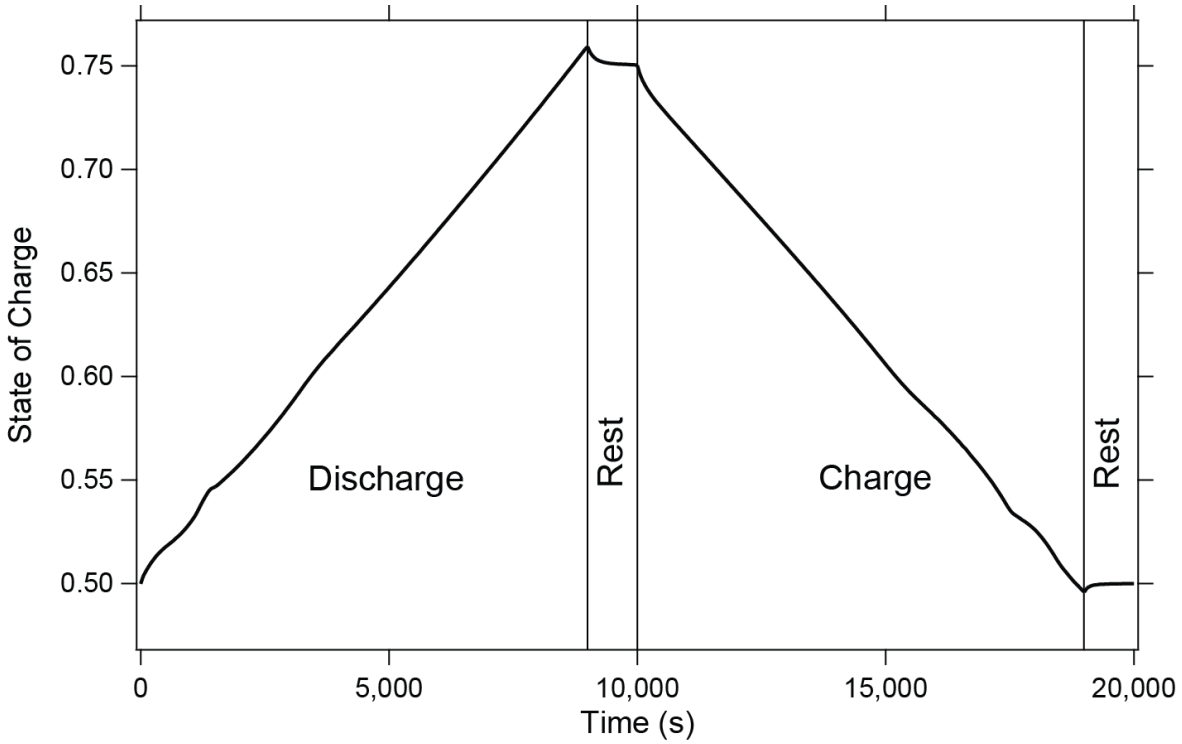

Figure 3.29. Local state of charge at point A in Figure 3.27 with a pliable separator and Figure 3.28 with an infinitely stiff separator. The state of charge for the two cases falls almost exactly on top of each other with a maximum difference at any point in time of 0.18% and an average difference of 0.0087%.

The comparison of Figures 3.27 and 3.28 is fairly qualitative; thus, in Figure 3.28 we look at the state of charge over time at point A seen in both Figures 3.27 and 3.28. In this plot, the state of charge from the pliable separator and infinitely stiff separator fall on top of one another such that they are indistinguishable. Through an analysis of the data points, the maximum difference between the state of charge at point A for the pliable separator and infinitely stiff separator cases is only 0.18 percent, and the average difference is only 0.0087 percent. Several other points in the positive electrode other than point A were compared with similar results, although only the comparison of point A is shown here. From this analysis we can conclude that a more uniform lithium electrode, caused by a stiff separator does not change the state of charge in the positive electrode appreciably.

Effect of Pressure Modified Reaction Kinetics on the Movement of Lithium with a Very Stiff Separator

In Section 3.5b, we modified the Butler-Volmer reaction kinetics at the negative electrode to be a function of pressure. Then, in Section 3.5c, we examined how this kinetics modified the height of lithium after cycling due to the stress build-up in the negative electrode. In that section, we found that it took a significant amount of pressure to modify the kinetics enough so that the height of lithium was significantly altered. In fact, we found that the pressures required to modify significantly the kinetics were so high that both elastic and plastic deformation of the lithium were likely to occur.

In the previous Subsection we included plastic deformation of the lithium at the negative electrode and saw that it significantly reduced the movement of the negative electrode, thereby reducing the stresses to around the yield strength of lithium. This can be seen in Figure 3.23 where the stress has a maximum of 8.6 bar and a minimum of -6.4 bar. In comparison to Figure 3.14 (where the lithium was assumed to be rigid) we can see that, because of plastic and elastic deformation, the peak stresses have been reduced by more than an order of magnitude. Obviously this significantly reduces the effect that the pressure-modified kinetics has on forcing the current density to be more nearly uniform, and in this Subsection we examine the effects of the kinetics on the movement of lithium with plastic deformation and a very stiff separator.

In order to determine directly the effect of the kinetics on the movement of lithium, two simulations were run, each at a C/5 rate to a 10 percent depth of discharge based on the positive electrode and with a polymer separator with a shear modulus of twice that of lithium (the shear modulus of lithium is 3.4 GPa). Plastic and elastic deformation of the lithium at the negative electrode was included for both simulations, and the only difference was the kinetics at the negative electrode.

Figure 3.30 shows the movement of lithium as measured in the number of coulombs of lithium passed through the $x = 0.375$ plane, the same as in Chapter 2. The 'Pressure-Modified Kinetics' line uses the modified Butler-Volmer kinetics as seen in Equation 3.99, and the 'Butler-Volmer Kinetics' line has unmodified Butler-Volmer kinetics at the negative electrode. The 'Pliable Separator, Butler-Volmer Kinetics' line is taken from Chapter 2 and is repeated here as a reference to compare with the plastically deformed lithium due to the 16 GPa separator. From Figure 3.30 below, we see that for both cases the movement seen during a cycle is significantly reduced by the stiff separator, with the pressure-modified kinetics having a slightly more uniform lithium profile.

In Chapter 2, we saw that, for the same rate of discharge and charge and the same depth of discharge, with a pliable separator around -22.5 coulombs moved after discharge. If we compare this to the -1.8 coulombs moved after discharge with a very stiff separator seen in Figure 3.30, the significant reduction in movement is obvious. As was discussed in detail in the previous Subsections, this reduction in movement is due to elastic and plastic deformation of the lithium and not the pressure-modified kinetics. Further evidence of this is seen when comparing the 'Pressure Modified Kinetics' line to the 'Butler-Volmer Kinetics' line in Figure 3.30. From this comparison we see that while the pressure-modified kinetics does reduce the movement of the lithium, this reduction is very small when compared to the decrease in the movement due to the mechanical deformation caused by the separator.

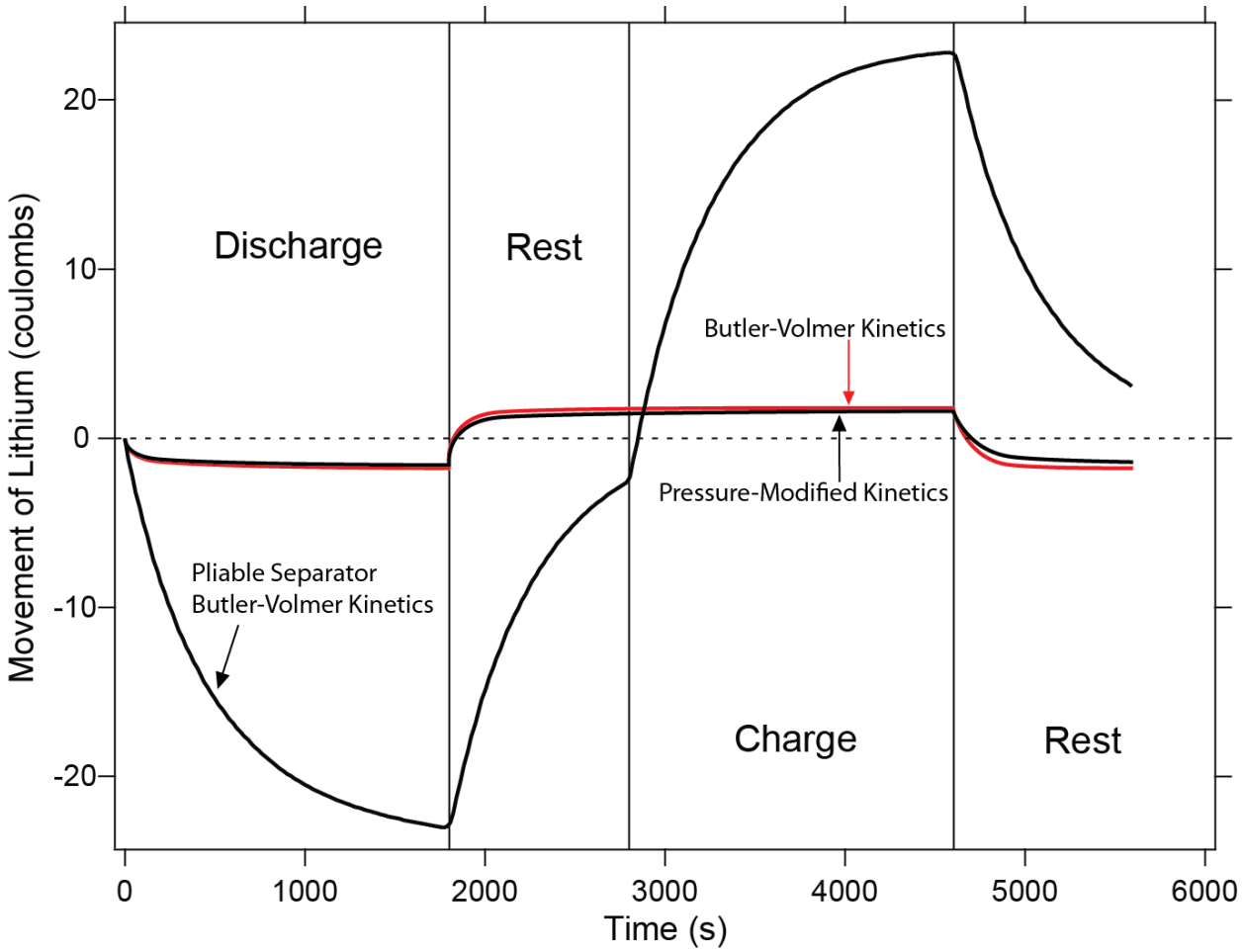

Figure 3.30. Movement of lithium along the lithium/separator interface during one cycle at a rate of C/5 to a 10% depth of discharge based on the positive electrode. Except for the 'Pliable Separator, Butler-Volmer Kinetics' line, the separator is a dendrite-inhibiting separator with a shear modulus twice that of lithium, and elastic and plastic deformation of the lithium was included.

Let us now turn our attention to discussing the reason for the difference in the movement of lithium due to the inclusion of the pressure dependence in the kinetics at the negative electrode. As is seen in Figure 3.30, with the pressure dependence, the movement is slightly less than without. This is due to the pressure forcing the current density to be more nearly uniform, similar to the mechanism seen in the work by Monroe et al.[4] To explain this in a more detailed manner, we look at the movement of lithium after discharge in Figure 3.22. Because of the nonuniform current distribution, the lithium is thinner on the left and thicker on the right, causing the separator to be in tension on the left and compression on the right. This pressure difference forces the current density to be more nearly uniform, thereby stripping the lithium more uniformly than if the kinetics had no pressure dependence. This effect, however, is significantly muted, due to plastic deformation where the stresses in the negative electrode

are limited by the yield strength of the lithium. Because the yield strength is so low, the stresses never reach a value high enough to alter the current density significantly.

3.8 Plastic Deformation as it Applies to the Deformation of a Dendrite

In Section 3.7 we saw that, with a separator with mechanical properties high enough to inhibit dendrite growth (a shear modulus twice that of lithium predicted by Monroe and Newman[4]) significant plastic deformation occurred resulting in a flattening of the lithium. In the work by Monroe and Newman,[4] they assumed that the lithium in a dendrite deforms only elastically. With only elastic deformation of the dendrite, the only mechanism to inhibit the propagation of the dendrite is by forcing the current density to be uniform through the pressure-modified kinetics developed by Monroe and Newman.[39] However, with the inclusion of plastic deformation, there exists a second mechanism to inhibit the propagation of the dendrite. As the dendrite grows, it deforms the separator causing the stress to rise. Once the stress in the lithium reaches the yield stress of the lithium, it can plastically deform thereby halting its growth through the polymer. Therefore, rather than predict the shear modulus requirements (or elastic modulus) of the separator in relation to the shear modulus (or elastic modulus) of the lithium, it should, instead, be related to the yield strength of the lithium which is about three orders of magnitude lower.

While a complete model for the propagation, stresses, and plastic deformation of a lithium dendrite has not been created, in this section we create a very simple model relating the elastic modulus of the separator to the yield stress of the lithium. Through this analysis it is hoped that the reader gain an order-of-magnitude estimate of the mechanical properties necessary for a separator to limit the propagation of a dendrite through plastic deformation of the lithium.

In this analysis several assumptions are made. First, we assume that the plastic deformation of the dendrite is the only mechanism that inhibits its growth through the separator. This means that we assume that the stress at the surface of the negative electrode is insufficient to alter significantly the pressure-modified kinetics. This assumption follows from the findings in Section 3.7b which showed that the pressure-modified kinetics played only a small role (when compared to plastic deformation) in limiting the movement of the lithium during cycling.

The second assumption is that the yield stress of lithium is constant and that yielding begins as soon as the stress reaches the yield stress of lithium. Furthermore, we assume that the lithium behaves as an isotropic crystalline material where the grain size of the lithium metal is much smaller than the length scale of a dendrite. This assumption is not particularly accurate since, in the case of zinc, the dendrites are single crystals.[35] Since the mechanical properties of a single crystal differ with the orientation of the crystal, the mechanical properties used in this

analysis should reflect this. Considering the lack of literature data even for bulk properties of lithium metal, we continue with our assumption that the lithium behaves as an isotropic material.

Next, we assume that the both the lithium and the polymer behave as perfectly elastic materials (a Poisson's ratio of 0) and that the only stress in either the lithium or the polymer is in the y direction, which is through the thickness of the cell. This assumption is purely for the sake of simplicity. We also relax the assumption that the positive electrode is perfectly rigid for the reason that, with a polymer separator, the polymer is typically mixed into the positive electrode as the electrolyte. This means that it is likely that the positive electrode deforms elastically, though not necessarily with the same elastic modulus. We do assume, however, that the separator and the positive electrode have the same elastic properties. Again, this is for the sake of simplicity and differing mechanical properties for the separator and positive electrode can be added to the model later.

Finally, we assume that the dendrite is in the shape of a cosine function, such as in Figure 3.31 below, with an amplitude of 0.1 µm. [4]

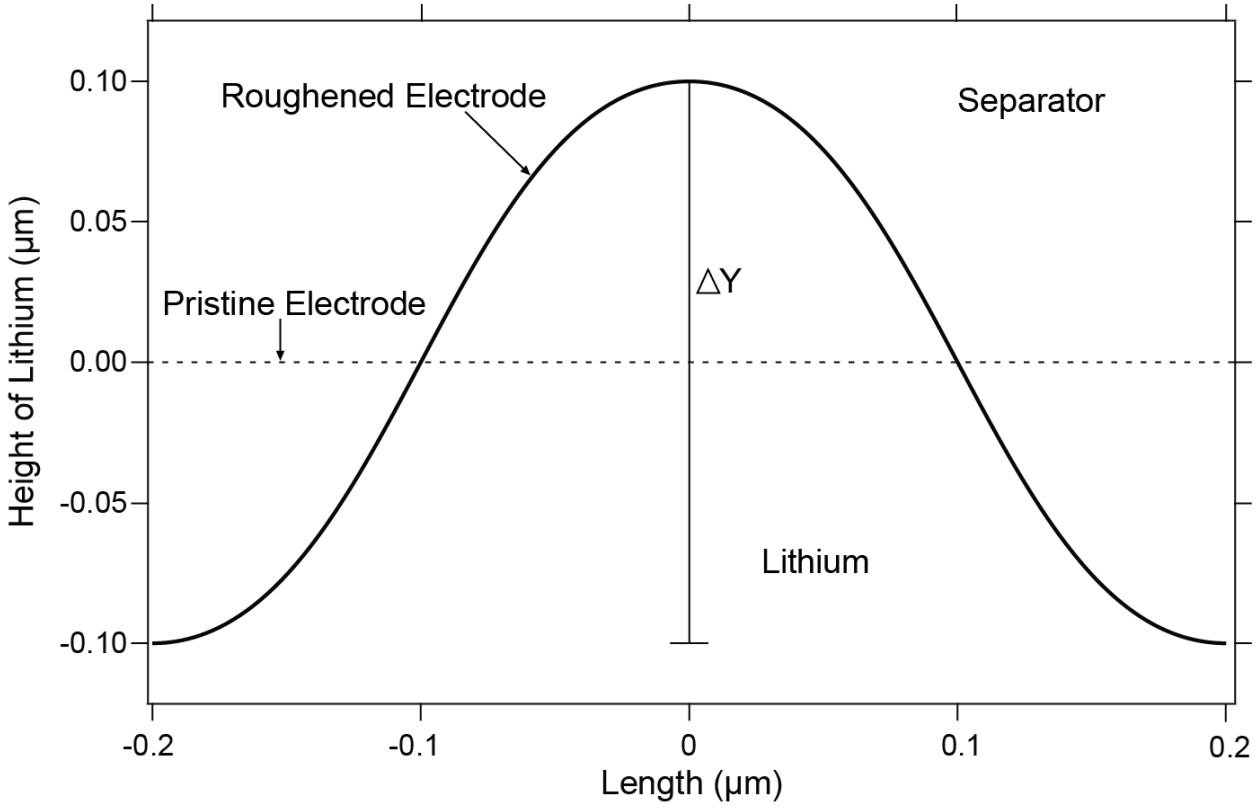

Figure 3.31. Schematic of a pristine electrode (dashed line) and a roughened lithium electrode (solid line). The roughened electrode is assumed to follow a cosine function. The top half of the diagram is a polymer separator and the bottom half lithium metal. ΔY is the peak to peak amplitude of the dendrite or half the amplitude of the cosine curve.

From these assumptions, we can describe the stress in the separator through Hooke's law:

$$\sigma_{y\,Sep} = E_{Sep}\epsilon_{y\,Sep} \tag{3.128}$$

where $\sigma_{y\,Sep}$ is the stress in the separator in the y direction, E_{Sep} is the elastic modulus of the separator, and $\epsilon_{y\,Sep}$ is the strain in the separator in the y direction. Similarly, we can describe the stress in the lithium through

$$\sigma_{y\,Li} = E_{Li}\epsilon_{y\,Li}. \tag{3.129}$$

Since we are interested in when the lithium deforms plastically, we use (again for the sake of simplicity) the Tresca yield criterion which states that yielding occurs when the largest difference in principal stresses equals the yield strength. Because we only consider stress in the y direction, the largest difference in the stress is $\sigma_{y\,Li} - 0$; therefore, plastic deformation occurs when $\sigma_{y\,Li} = \sigma_Y$ where σ_Y is the yield strength of lithium.

In order to relate Equation 3.128 to Equation 3.129, we convert the strains to deformations (assuming the deformations are small) such that Equation 3.128 becomes

$$\sigma_{y\,Sep} = E_{Sep}\frac{\Delta Y_{Sep}}{Y_{Sep}^0} \tag{3.130}$$

where ΔY_{Sep} is the change in the thickness of the separator relative to its initial thickness Y_{Sep}^0. Equation 3.129 is similarly updated to

$$\sigma_Y = E_{Li}\frac{\Delta Y_{Li}^e}{Y_{Li}^0} \tag{3.131}$$

where ΔY_{Li}^e is the change in the thickness of the lithium due to elastic deformation and Y_{Li}^0 is the initial thickness of the lithium. Here we assume that the change in the thickness of the separator and the lithium due to the growth of the dendrite is much smaller than the thickness of either the separator or the lithium. We can now relate the deformation of the separator to the height of the dendrite through

$$\Delta Y_{Sep} = \Delta Y - \Delta Y_{Li}^e \tag{3.132}$$

where ΔY is the peak to peak amplitude of the dendrite, as seen in Figure 3.31. We now combine Equations 3.130, 3.131, and 3.132 and solve for the elastic modulus of the separator to get

$$E_{Sep} = \frac{\sigma_Y Y_{Sep}^0}{\Delta Y - \frac{\sigma_Y}{E_{Li}} Y_{Li}^0}. \quad 3.133$$

As we can see from Equation 3.133, the elastic modulus of the separator is a function of the yield strength of lithium, the elastic modulus of lithium, the height of the dendrite that allow, and the thickness of both the separator and the lithium. Here we are assuming a maximum allowable height of the dendrite before the separator deforms it plastically.

To get an idea of what values of E_{Sep} to expect, let us choose some values for the properties of lithium to use in Equation 3.133. From Section 3.7, we set the yield strength of lithium at 0.655 MPa[31] and the elastic modulus to 4.9 Gpa[29]. Let us now say that the lithium is 50 µm thick and the positive electrode and separator can deform elastically thereby making Y_{Sep}^0 125 µm. We set ΔY to 0.2 µm and use Equation 3.133 to estimate the elastic modulus of the separator to be 0.42 Gpa in order to inhibit dendrite growth. From this analysis, we predict that the elastic modulus of the separator be on the order of 1/10th of the elastic modulus of the lithium. Or, better yet, the elastic modulus of the separator should be about two orders of magnitude higher than the yield strength of lithium.

The properties of the lithium metal used in the previous analysis are fairly variable. This variation in both the elastic modulus and the yield strength can be seen in Table 3.2 below where values for both the elastic modulus and yield strength are taken from three different references at various temperatures.

Table 3.2. Physical properties of lithium metal as found in several references and at several temperatures. The elastic modulus and yield strength for reference 31 were found through a compressive test of lithium metal and the elastic moduli and yield strengths found in reference 32 were obtained using a tensile test. The specifics of the test used to determine the elastic modulus in reference 29 was not specified.

Elastic Modulus (Gpa)	T (˚C)	Yield Strength (Mpa)	Reference
1.90	25	0.655	31
7.80	25	0.76	32
5.00	50	0.42	32
4.00	75	0.41	32
4.90	25	-	29

From Table 3.2, we can see the variation of both the elastic modulus of lithium and yield strength. However, in Equation 3.133, changing the elastic modulus of the lithium only slightly affects the value of E_{Sep}. For example, with E_{Li}= 7.8 GPa we calculate E_{Sep}= 0.418 GPa, whereas with E_{Li}= 1.9 GPa we calculate E_{Sep}= 0.448 GPa. The yield strength of lithium, however, affects E_{Sep} much more strongly since increasing it increases the numerator and decreases the denominator of Equation 3.133. For example, with σ_Y = 0.76 MPa, E_{Sep}= 0.494 GPa, but with σ_Y = 0.41 MPa, E_{Sep}= 0.262 GPa.

It should be noted again that the model developed in this section is a very basic model intended only to give the reader an order-of-magnitude understanding of what mechanical properties should be expected of a dendrite-inhibiting separator. Obviously a much more detailed model needs to be developed to give a more accurate estimate of the mechanical properties necessary. For example, no viscoelastic effects for either the separator or the lithium were included. Polymers often exhibit viscoelastic effects and it is possible that a dendrite could grow slowly enough to allow for the polymer to viscoelastically deform at stresses below the yield strength of lithium metal. This would allow the dendrite to propagate through the separator without deforming plastically. It is in the author's opinion, however, that the model in this section is useful for gaining a quick, order-of-magnitude estimate of the elastic modulus required of a dendrite-inhibiting separator. Furthermore, this model shows us that the elastic modulus of a dendrite-inhibiting separator should be a function of the yield strength of the lithium as well as the thicknesses of the separator and the lithium and the height of the dendrite before plastic deformation takes place.

3.8 Conclusions

In this chapter, the two-dimensional model presented in Chapter 1, which is able to capture the movement of lithium during cycling, was run with separators with a 400 MPa elastic modulus and with a 16 GPa elastic modulus. Both separators resist the movement of lithium seen in Chapters 1 and 2 through the generation of stresses in the cell. As the lithium moves, the separator is either compressed or stretched, translating into stresses in the separator and lithium. These stresses affect the negative electrode through two mechanisms -altering the thermodynamics of the negative electrode and deforming the negative electrode mechanically. Both of these mechanisms were treated in this chapter.

In Section 3.2 the basic definitions of stress and strain were discussed including principal stress and strains, invariants, and the uniaxial tension test. Then, in Section 3.3, the equations for elastic deformation were developed. Section 3.4 lent itself to the discussion of plastic deformation including yield criteria, dislocation theory, and the development and derivation of the equations for plasticity.

The later sections of this chapter dealt with the implementation of the equations developed in the beginning of the chapter. In Section 3.5, we introduced the problem at hand and discussed the model geometry. Then, the effect of the stress on the thermodynamics and its relation to the reaction kinetics at the negative electrode were developed. We saw that it took very high pressures to modify the kinetics enough to have an appreciable effect on the movement of lithium. It was noted that under these pressures, the assumption that the lithium was rigid was invalid; thus the elastic deformation of lithium was included. This again, relaxed the stresses in the negative electrode through the elastic compression of the lithium, However the stresses in the negative electrode were still significantly larger than the yield strength of lithium, and thus it was concluded that plastic deformation of the negative electrode must be included.

In Section 3.6, the limit-analysis theorems, which were developed in Section A.5 of Appendix A, were applied to the deformation of the lithium negative electrode. Through this analysis we found that, under the stresses seen in Section 3.6, plastic deformation could occur and would cause a mechanical deformation of the lithium from the region in compression to the region in tension.

Finally, in Section 3.7, the equations for plastic deformation were incorporated into the model. From this, we saw that a very stiff (16 GPa), dendrite-inhibiting separator can cause plastic and elastic deformation of the lithium at the negative electrode, thereby mechanically resisting the lithium movement seen in Chapters 1 and 2. We found that the plastic deformation plays a much larger role than either the pressure-modified reaction kinetics or elastic deformation and deformed the lithium toward uniformity. Furthermore, the flattening of the negative electrode caused only very slight differences in the local state of charge in the positive electrode. Thus, it can safely be said that including a dendrite-inhibiting separator benefits a lithium-metal battery through forcing the negative electrode to be more uniform without causing negative effects in the positive electrode such as larger swings in the local state of charge.

List of Symbols

A	Area	[m^2]
c_i	Concentration	[mol/m^3]
E	Young's or elastic modulus	[Pa]
F	Force	[N]
F	Faraday's constant, 96,485 (Section 3.6)	[C/mol]
G	Shear modulus	[Pa]
G	Gibb's free energy	[J]
H	Hardening properties of a material	[-]
i_0	Exchange current density	[A/m^2]
i_{loc}	Local current density	[A/m^2]
I	Identity matrix	[-]
I_i	Stress invariants	[Pa^n]
$\bar{I}_i$	Strain invariants	[-]
J_i	Deviatoric stress invariants	[Pa^n]
k_a	Anodic reaction rate constant	[m^3/s]
k_c	Cathodic reaction rate constant	[m^3/s]
K	Bulk modulus	[Pa]
L	Length	[m]
$\underline{N}$	Unit normal vector	[-]
p	Hydrostatic stress	[Pa]
p	Pressure	[Pa]
q_i	Displacement (Section 3.5)	[m]
R	Universal gas constant, 8.314	[J/mol-K]
S_{ij}	Stress deviator	[Pa]
T	Temperature	[K]
u	Deformation in the x-direction	[m]
U_0	Open-circuit potential	[V]
U_p	Open-circuit potential due to pressure	[V]
v	Deformation in the y-direction	[m]
V	Volume	[m^3]
$\overline{V}$	Partial molar volume	[m^3/mol]
w	Deformation in the z-direction	[m]
W	Work	[J]
x_1	x-direction	[m]
x_2	y-direction	[m]
x_3	z-direction	[m]

α_a	Anodic transfer coefficient	[-]
α_c	Cathodic transfer coefficient	[-]
α_m	Transfer coefficient for the metal (assumed to be 1)	[-]
δ_{ij}	Kronecker delta	[-]
ϵ	Strain	[-]
ϵ_{ij}	Strain components	[-]
ϵ_i	Principal strains	[-]
ϵ^p	Plastic strain	[-]
$\bar{\epsilon}^p$	Equivalent plastic strain (see Equation 3.26)	[-]
η_s	Surface overpotential	[V]
κ	Shear yield strength	[Pa]
λ	Hardening parameter	[-]
μ	Chemical potential	[J/mol]
μ^p	Chemical potential due to pressure	[J/mol]
ν	Poisson's ratio	[-]
σ	Stress	[Pa]
σ_{ij}	Stress components	[Pa]
σ_i	Principal stresses	[Pa]
σ_Y	Yield stress	[Pa]
$\bar{\sigma}$	von Mises or equivalent stress	[Pa]
τ	Shear stress (also $\sigma_{i,j \text{ for } i \neq j}$)	[Pa]
τ_Y	Shear yield stress	[Pa]
Φ	Potential across the interface at the negative electrode (Section 3.6)	[V]

References

Chapter 1

1. J. Tarascon and M. Armand. "Issues and Chalanges Facing Rechargeable Lithium Batteries," *Nature*, **414**, 359-367 (2001).
2. S. Sivakkumar, D. MacFarlane, M. Forsyth, and D. Kim. "Ionic Liquid-Based Rechargeable Lithium Metal-Polymer Cells Assembled with Polyaniline/Carbon Nanotube Composite Cathode," *Journal of the Electrochemical Society*, **154**, A834-A838 (2007).
3. J. Xu, J. Yang, Y. NuLi, J. Wang, and Z. Zhang. "Additive-Containing Ionic Liquid Electrolytes for Secondary Lithium Battery," *Journal of Power Sources*, **160**, 621-626 (2006).
4. C. Monroe and J. Newman. “A Propagation Model for Liquid Electrolytes under Galvanostatic Conditions,” *Journal of the Electrochemical Society,* **150**, A1377-A1384 (2003).
5. C. Monroe and J. Newman. “The Impact of Elastic Deformation on Deposition Kinetics at Lithium / Polymer Interfaces,” *Journal of the Electrochemical Society*, **152**, A396-A404 (2005).
6. C. Monroe, *Dendrite Initiation and Growth in Lithium/Polymer Systems*, Dissertation, University of California, Berkeley, (2004).
7. M M. Park and N. Balsara. "Phase Behavior of Symmetric Sulfonated Block Copolymers," *Macromolecules*, **41**, 3678-3687 (2008).
8. M. Singh, O. Odusanya, G. M. Wilmes, H. Eitouni, E. Gomez, A. Patel, V. Chen, M. Park, P. Fragouli, H. Iatrou, N. Hadjichristidis, D. Cookson, and N. Balsara. "Effect of Molecular Weight on the Mechanical and Electrical Properties of Block Copolymer Electrolytes," *Macromolecules*, **40**, 4578-4585 (2007).
9. N. Wanakule, A. Panday, S. Mullin, E. Gann, A. Hexemer, and N. Balsara. "Ionic Conductivity of Block Copolymer Electrolytes in the Vicinity of Order-Disorder and Order-Order Transitions," *Macromolecules*, **42**, 5642-5651 (2009).
10. J. Bates, N. Dudney, B. Neudecker, A. Ueda, and C. Evans. “Thin-film Lithium and Lithium-ion Batteries,” *Solid State Ionics*, **135**, 33-45 (2000).
11. J. Bates, G. Gruzalski, N. Dudney, C. Luck, and X. Yu. “Rechargeable Thin-film Lithium Batteries,” *Solid State Ionics*, **70**, 619-628 (1994).
12. K. Choi, D. Bennion, and J. Newman. “Engineering Analysis of Shape Change in Zinc Secondary Electrodes. I. Theoretical,” *Journal of the Electrochemical Society*, **123**, 1616-1627 (1976).

13. K. Choi, D. Hamby, D. Bennion, and J. Newman. “Engineering Analysis of Shape Change in Zinc Secondary Electrodes. II. Experimental,” *Journal of the Electrochemical Society*, **123**, 1628-1637 (1976).
14. T. Fuller, M. Doyle, and J. Newman. “Simulation and Optimization of the Dual Lithium Ion Insertion Cell,” *Journal of the Electrochemical Society*, **141**, 982-990 (1994).
15. M. Doyle, T. Fuller, and J. Newman. “Modeling the Galvanostatic Charge and Discharge of the Lithium/Polymer/Insertion Cell,” *Journal of the Electrochemical Society*, **140**, 1526-1533 (1993).
16. M. Doyle and J. Newman. “Modeling the Performance of Rechargeable Lithium-based Cells: Design Correlations for Limiting Cases,” *Journal of Power Sources*, **54**, 46-51 (1995).
17. M. Doyle, J. Newman, A. Gozdz, C. Schmutz, and J. M. Tarascon. “Comparison of Modeling Predictions with Experimental Data from Plastic Lithium Ion Cells,” *Journal of the Electrochemical Society*, **143**, 1890-1903 (1996).
18. T. Fuller, M. Doyle, and J. Newman. “Simulation and Optimization of the Dual Lithium Ion Insertion Cell,” *Journal of the Electrochemical Society*, **141**, 1-10 (1994).
19. J. Newman and K. Thomas-Alyea, *Electrochemical Systems 3rd edition*, John Wiley & Sons: Hoboken, NJ (2004).
20. P. Albertus, *Performance and Aging of Batteries for Vehicle Applications*, Dissertation, University of California, Berkeley, (2009).
21. D. A. G. Bruggeman. *Annalen Der Physik* **25**, 0645-0672 (1936).
22. K. Thomas, *Lithium-Ion Batteries: Thermal and Interfacial Phenomena*, Dissertation, University of California, Berkeley, (2002).
23. L. Rao and J. Newman. “Heat-Generation Rate and General Energy Balance for Insertion Battery Systems,” *Journal of the Electrochemical Society* **144**, 2697-2704 (1997).
24. R. Pollard and J. Newman. “Mathematical Modeling of the Lithium-Aluminum, Iron Sulfide Battery. I. Galvanostatic Discharge Behavior,” *Journal of the Electrochemical Society* **128,** 491-502 (1981).
25. S. Kikkawa, S. Miyazaki, and M. Koizumi. “Electrochemical Aspects of the Deintercalation of Layered AMO_2 Compounds,” *Journal of Power Sources* **14**, 231-234 (1985).
26. S. Stewart, *Determination of Transport Properties and Optimization of Lithium-Ion Batteries*, Dissertation, University of California, Berkeley, (2007).

Chapter 2

1. T. Fuller, M. Doyle, and J. Newman. “Simulation and Optimization of the Dual Lithium Ion Insertion Cell,” *Journal of the Electrochemical Society*, **141**, 982-990 (1994).
2. M. Doyle, T. Fuller, and J. Newman. “Modeling the Galvanostatic Charge and Discharge of the Lithium/Polymer/Insertion Cell,” *Journal of the Electrochemical Society*, **140**, 1526-1533 (1993).
3. M. Doyle and J. Newman. “Modeling the Performance of Rechargeable Lithium-based Cells: Design Correlations for Limiting Cases,” *Journal of Power Sources*, **54**, 46-51 (1995).
4. M. Doyle, J. Newman, A. Gozdz, C. Schmutz, and J. M. Tarascon. “Comparison of Modeling Predictions with Experimental Data from Plastic Lithium Ion Cells,” *Journal of the Electrochemical Society*, **143**, 1890-1903 (1996).
5. T. Fuller, M. Doyle, and J. Newman. “Simulation and Optimization of the Dual Lithium Ion Insertion Cell,” *Journal of the Electrochemical Society*, **141**, 1-10 (1994).
6. J. Newman and K. Thomas-Alyea, *Electrochemical Systems 3rd edition*, John Wiley & Sons: Hoboken, NJ (2004).

Chapter 3

1. J. Tarascon and M. Armand. "Issues and Chalanges Facing Rechargeable Lithium Batteries," *Nature*, **414**, 359-367 (2001).
2. S. Sivakkumar, D. MacFarlane, M. Forsyth, and D. Kim. "Ionic Liquid-Based Rechargeable Lithium Metal-Polymer Cells Assembled with Polyaniline/Carbon Nanotube Composite Cathode," *Journal of the Electrochemical Society*, **154**, A834-A838 (2007).
3. J. Xu, J. Yang, Y. NuLi, J. Wang, and Z. Zhang. "Additive-Containing Ionic Liquid Electrolytes for Secondary Lithium Battery," *Journal of Power Sources*, **160**, 621-626 (2006).
4. C. Monroe and J. Newman. "The Impact of Elastic Deformation on Deposition Kinetics at Lithium/Polymer Interfaces," *Journal of the Electrochemical Society*, **152**, A396-A404, (2005).
5. M. Park and N. Balsara. "Phase Behavior of Symmetric Sulfonated Block Copolymers," *Macromolecules*, **41**, 3678-3687 (2008).
6. M. Singh, O. Odusanya, G. M. Wilmes, H. Eitouni, E. Gomez, A. Patel, V. Chen, M. Park, P. Fragouli, H. Iatrou, N. Hadjichristidis, D. Cookson, and N. Balsara. "Effect of Molecular Weight on the Mechanical and Electrical Properties of Block Copolymer Electrolytes," *Macromolecules*, **40**, 4578-4585 (2007).

7. N. Wanakule, A. Panday, S. Mullin, E. Gann, A. Hexemer, and N. Balsara. "Ionic Conductivity of Block Copolymer Electrolytes in the Vicinity of Order-Disorder and Order-Order Transitions," *Macromolecules*, **42**, 5642-5651 (2009).
8. N. Suh and A. Turner. *Elements of the Mechanical Behavior of Solids*, Scripta Book Company: Washington D.C. (1975).
9. F. McClintock and A. Argon. *Mechanical Behavior of Materials*, Addison-Wesley Publishing Company: Reading, MA (1966).
10. S. Bodner. *Mechanical Behavior of Materials Under Dynamic Loads, San Antonio Symposium,* Springer-Verlag: New York, NY (1967).
11. W. Hosford. *Mechanical Behavior of Materials,* 2nd Edition, Cambridge University Press, Cambridge, UK. (2010).
12. A. Boresi, and R. Schmidt. *Advanced Mechanics of Materials,* 6th Edition, John Wiley & Sons: New York, NY (2003).
13. L. Prandtl. "Ein Ein Gedankenmodell zur kinetischen Theorie der festen Körper ," *Zeitschrift für Angewandte Mathematik und Mechanik*, **8**, 85-106 (1928).
14. I. Berman and P. Hodge. "A general theory of piecewise linear plasticity for initially anisotropic materials," *Archiwum Mechaniki Stosowanej*, **11**, 513-540 (1959).
15. G. Taylor. "The Mechanism of Plastic Deformation of Crystals. Part I: Theoretical," *Proceedings of the Royal Society of London A*, **145**, 362-387 (1934).
16. M. Polanyi. "Über eine Art Gitterstörung, die einen Kristall plastisch machen könnte," *Zeitschrift für Physik*, **89**, 660-664 (1934).
17. E. Orowan. "Zur Kristallplastizität," *Zeitschrift für Physik*, **89**, 605-613 (1934).
18. R. von Mises. "Mechnik der plastischen Formanderung von Kristallen," *Zeitschrift für Angewandte Mathematik und Mechanik*, **8**, 161-185 (1928).
19. A. Khan and S. Huang. *Continuum Theory of Plasticity*, John Wiley & Sons: New York, NY (1995).
20. J. Lubliner. *Plasticity Theory*, Macmillan Publishing Company: New York, NY (1990).
21. P. Papadopoulos, *personal correspondence*. Department of Mechanical Engineering, University of California, Berkeley, June 2013.
22. R. Ritchie, *personal correspondence*. Department of Material Science and Engineering, University of California, Berkeley, June 2013.
23. W. Prager. *An Introduction to Plasticity*, Addison-Wesley: Reading, MA (1961).
24. K. Hohenemser and W. Prager. "Über die Ansätze der Mechanik isotroper Kontinua," *Zeitschrift für Angewandte Mathematik und Mechanik*. **12**, 216-226 (1932).
25. J. Newman and K. Thomas-Alyea, *Electrochemical Systems,* 3rd edition, John Wiley & Sons: Hoboken, NJ (2004).
26. A. Sheidaei, X. Xiaoa, X. Huangb, and J. Hitt. "Mechanical Behavior of a Battery Separator in Electrolyte Solutions," *Journal of Power Sources*, **196**, 8728-8734 (2011).

27. G. Day and S. Price. "Properties of crystalline organic molecules," in *Handbook of Elastic Properties of Solids, Liquids, and Gasses,* volume 3 (M. Levy and L. Furr, eds.), p. 65, Academic Press: San Francisco, CA, (2001).
28. L. Nielsen. *Mechanical properties of Polymers*, p. 7, Reinhold: New York, NY, (1967).
29. S. Pugh, "Mechanical properties of the elements," in *Handbook of the Physicochemical Properties of the Elements* (G. V. Samsonov, ed.), New York, New York: IFI Plenum, 1968.
30. G. Kaye and T. Laby. "Bulk moduli of elements," in *Tables of Physical and Chemical Constants,* 16th Edition, Longman: London, (1995).
31. R. Schultz. "Lithium: Measurement of Young's Modulus and Yield Strength," Fermilab TN 2191, 2002.
32. S. Tariq, K. Ammigan, P. Hurh, R. Schultz, P. Liu, and J. Shang. "Li Material Testing - Fermilab Antiproton Source Lithium Collection Lens" *Proceedings of the 2003 Particle Accelerator Conference*
33. J. Newman, and T. Chapman. "Restricted Diffusion in Binary Solutions," *A.I.Ch.E. Journal*, **19**, 343 (1973).
34. J. Barton and J. Bockris. "The Electrolyte Growth of Dendrites from Ionic Solutions," *Proceedings of the Royal Society of London A*, **42**, 7355 (1990).
35. J. W. Diggle, A. R. Despic, and J. O'M Bockris. "The Mechanism of the Dendritic Electrocrystallization of Zinc," *Journal of the Electrochemical Society*, **116**, 1503 (1969).
36. R. Bird, W. Stewart, and E. Lightfoot. *Transport Phenomena*, 1st edition, John Wiley & Sons: New York, NY (1960).
37. L. Landau and E. Lifshitz. *Theory of Elasticity*, translated by J. Sykes and W. Reid, 3rd edition, Elsevier: Burlington, MA (1986).
38. L. Malvern. *Introduction to the Mechanics of a Continuous Medium*, Prentice-Hall: Englewood, NJ (1969).
39. C. Monroe and J. Newman. "The Effect of Interfacial Deformation on Electrodeposition Kinetics," *Journal of the Electrochemical Society*, **151**, A880-A886, (2004).

Appendix A

1. F. McClintock and A. Argon. *Mechanical Behavior of Materials*, Addison-Wesley Publishing Company: Reading, MA (1966).
2. G. Taylor. "The Mechanism of Plastic Deformation of Crystals. Part I: Theoretical," *Proceedings of the Royal Society of London A*, **145**, 362-387 (1934).
3. M. Polanyi. "Über eine Art Gitterstörung, die einen Kristall plastisch machen könnte," *Zeitschrift für Physik*, **89**, 660-664 (1934).
4. E. Orowan. "Zur Kristallplastizität," *Zeitschrift für Physik*, **89**, 605-613 (1934).

5. R. Bird, W. Stewart, and E. Lightfoot. *Transport Phenomena*, 2nd edition, John Wiley & Sons: New York, NY (2002).
6. N. Suh and A. Turner. *Elements of the Mechanical Behavior of Solids*, Scripta Book Company: Washington D.C. (1975).
7. A. Boresi, and R. Schmidt. *Advanced Mechanics of Materials,* 6th Edition, John Wiley & Sons: New York, NY (2003).
8. L. Landau and E. Lifshitz. *Theory of Elasticity*, translated by J. Sykes and W. Reid, 3rd edition, Elsevier: Burlington, MA (1986).

Appendix A

It is the purpose of this appendix to give the reader an extended understanding of several topics discussed in Chapter 3. Therefore, equations that were derived or first stated in Chapter 3 are notated with their original numbering to aid the reader in cross-referencing.

A.1 Dislocation Theory

Let us turn our attention to the nature of how plastic deformation occurs, which is mainly through the generation and motion of dislocations, or imperfections within a crystal. These dislocations can occur within a grain in a metal, but are common between grains where two different crystal structures meet or, where two materials meet. Although primarily considered to be in the field of material science, it is, none the less, of importance and is discussed briefly here in order to gain a basic understanding of the mechanism for plastic deformation. Further information on this subject can be found in most material-science or continuum-theory text books in varying detail. Although I have by no means done an exhaustive search of the literature on dislocation theory, one text on the subject that I found quite useful was that by McClintock and Argon.[1]

Originally the theory for how crystals deformed plastically was through the shearing or slipping of an entire plane of atoms. This theory, however, was discredited in the early twentieth century when the stresses required to cause slip were measured by tension tests of single crystals. These tests found that the stresses required to cause slip were two or more orders of magnitude lower than those predicted if the entire plane were to slip at once. Therefore, and alternate theory of the mechanism for plastic deformation, called *dislocation theory*, was proposed.[2-4]

Dislocation theory states that crystals contain preexisting defects, called dislocations that are boundaries between regions that are already displaced relative to one another by one unit of slip. Movement of a dislocation allows slip to occur and the stress for slip is the stress required to move a dislocation rather than the stress required to move an entire plane.

There are two important unique forms of dislocations that are of note: edge dislocations and screw dislocations. The geometry of an edge dislocation (seen below in Figure A.1) can be visualized by cutting part way into a perfect crystal and then inserting an extra half plane of atoms. The other unique form of a dislocation is the screw dislocation (seen in Figure A.2). This can be visualized by cutting part way into a perfect crystal and then shearing the cut by one atomic distance. Both the case of the edge dislocation and screw dislocation are merely extreme cases; the reality is usually any number of combinations of these dislocations.

In both cases, the dislocation is the boundary between a region that has slipped and one that has not. For the case of the edge dislocation, ⊥, as seen in Figure A.1, the dislocation is the boundary between the region that has slipped (let us say the region to the left of the dislocation, ⊥) and the region that has not slipped (let us say the region to the right of the dislocation, ⊥). The imagined extra half plane is then directly above ⊥. When an edge dislocation moves, the direction of slip is perpendicular to the dislocation. This can be seen by breaking the bonds between atoms A and B and forming bonds between A and D. This has the effect of moving the dislocation one unit to the right.

Somewhat in contrast to an edge dislocation, the movement of a screw dislocation causes slip in the direction parallel to itself. This movement can be seen in Figure A.2 if you imagine that the atom at point A instead bonds with atom at point B, and all the subsequent atoms below A also slip vertically. The screw dislocation will then have shifted one unit to the right.

Instead of considering these defects in terms of the motion of the atoms around them, like we have in the previous paragraphs, it is typical to consider the imperfections as separate entities. Thus, we consider plastic deformation to be due to the motion and mutual interaction of these dislocations in an otherwise ideal crystal.

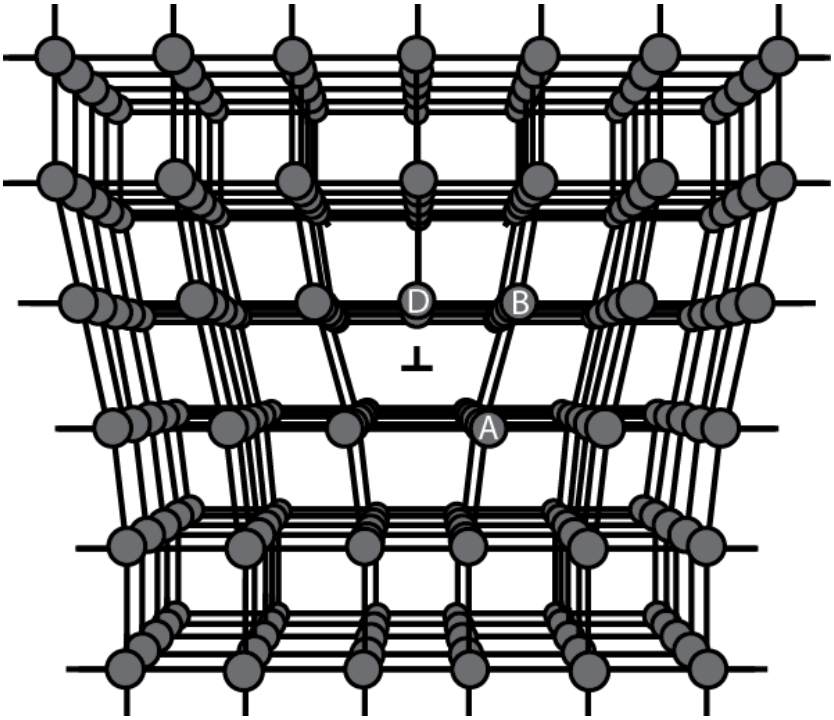

Figure A.1. An edge dislocation in a crystal lattice or the addition of an extra half plane into a perfect crystal.

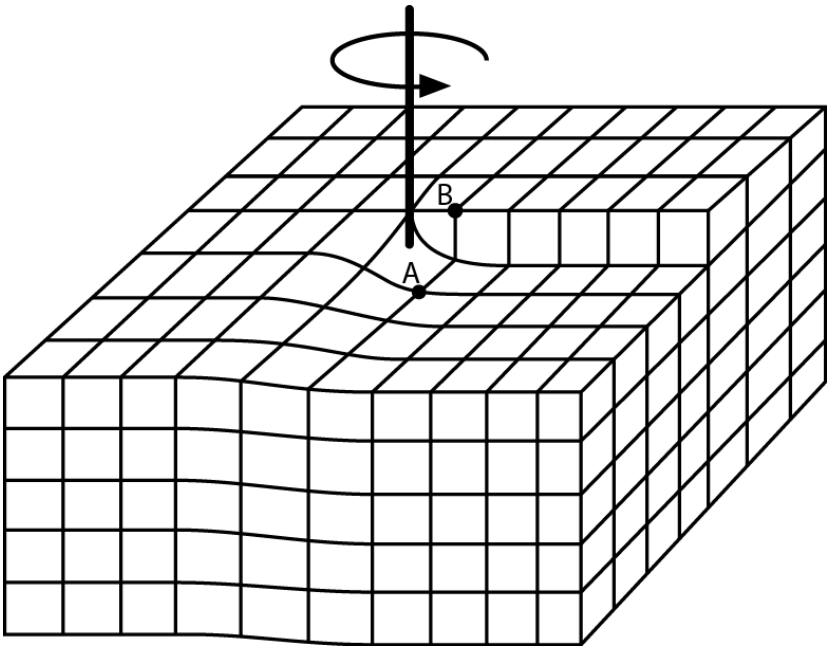

Figure A.2. A screw dislocation around which the crystal lattice forms a helical pattern.

This picture of a dislocation traveling through a frozen lattice, where every atom is at precisely prescribed lattice sites, is correct only at very low temperatures, where the effect of thermal oscillations can be neglected. This picture is not as accurate, however, at higher temperatures where there is an increased level of thermal motion that makes slip possible in most crystal's other directions.

A.2 Derivation of the Hardening Parameter λ from the von Mises Yield Criterion

Let us turn our attention to describing $\dot{\lambda}$ in

$$\underline{\underline{\epsilon}} = \dot{\lambda}\underline{\underline{S}} \quad \text{or} \quad \dot{\epsilon}_{ij}^{p} = \dot{\lambda}S_{ij}, \tag{3.54}$$

which can be found through the use of the von Mises yield criterion. Since the von Mises yield criterion is defined as

$$J_2 = \kappa^2 = \frac{1}{3}\sigma_Y^2, \tag{3.37}$$

and the second deviatoric stress invariant is defined as

$$J_2 = \frac{1}{2}S_{ij}S_{ij}, \tag{3.10}$$

then, through combining Equations 3.37 and 3.10, we get

$$S_{ij}S_{ij} = \frac{2}{3}\sigma_Y^2. \quad \text{A.1}$$

Squaring Equation 3.54 gives us

$$\dot{\epsilon}_{ij}^p \dot{\epsilon}_{ij}^p = \dot{\lambda}^2 S_{ij} S_{ij}, \quad \text{A.2}$$

and, substituting in Equation A.1 into A.2, leads to

$$\dot{\epsilon}_{ij}^p \dot{\epsilon}_{ij}^p = \dot{\lambda}^2 \frac{2}{3}\sigma_Y^2 \quad \text{A.3}$$

or

$$\dot{\lambda}^2 = \frac{3\dot{\epsilon}_{ij}\dot{\epsilon}_{ij}}{2\sigma_Y^2}. \quad \text{A.4}$$

Taking the square root of Equation A.4 gives us

$$\dot{\lambda} = \sqrt{\frac{3\dot{\epsilon}_{ij}^p \dot{\epsilon}_{ij}^p}{2\sigma_Y^2}}, \quad \text{A.5}$$

and, from the definition of incremental strain (assuming plastic incompressibility), we get

$$\dot{\bar{\epsilon}}^p = \frac{2}{3}\left(\frac{3}{2}\dot{\epsilon}_{ij}^p \dot{\epsilon}_{ij}^p\right)^{\frac{1}{2}}. \quad 3.24$$

Substituting Equation 3.24 into Equation A.5 yields

$$\dot{\lambda} = \frac{3}{2}\frac{\dot{\bar{\epsilon}}^p}{\sigma_Y} \quad \text{A.6}$$

A.3 Limit Analysis

Obtaining an exact solution to all but the most simple geometries in continuum mechanics is a daunting task. It is useful, therefore, to be able to get an approximate solution which bounds the problem and gives an estimate of what the numerical solution might look like.

In this section, limit theorems are presented, which provide the basis for determining limiting solutions. These limiting solutions can be classified into upper-bound and lower-bound solutions for the load (defined as $\sqrt{3/2\,\underline{\underline{S}} : \underline{\underline{S}}}$) required to cause plastic deformation. An upper-bound solution overestimates the true load while a lower-bound solution underestimates it. If both the upper and lower bounds can be established, the range of possible values for the true load is determined. When the difference between the upper- and lower-bound solutions is insignificant, the approximations provide answers which are very close to the true solutions. Although it is not always possible to determine both the upper- and lower-bound solutions, any limiting solution can be useful. For example, in the materials-processing field, the upper-bound solution can provide answers for stress (and power) which will be more than sufficient to perform a given task. On the other hand, in structural designs, the lower-bound solutions can provide a conservative estimate of the load-carrying capacity of a structure, and is much more desirable than the overestimated upper bound.

The theorems of limit analysis are developed for incompressible plastic materials (Poisson ratio of 0.5) and thus, assume that only plastic deformation occurs and that volume changes are negligible. The upper- and lower-bound theorems are simply stated in Sections 3.5a and A.3b. Then, in Section A.3c, an example problem is discussed. The full derivation of the upper and lower-bound limit theorems is given in detail by both Suh and Turner[6] and McClintock and Argon.[1]

A.3a Lower-Bound Limit Theorem

The lower-bound limit estimates the lower limit of a load required to cause plastic deformation to occur. The theorem states that:

"-The load corresponding to an assumed stress field which satisfies:

1) the equilibrium condition everywhere in the continuum ($\nabla \cdot \sigma = 0$)
2) the yield criterion (either the Tresca or von Mises)
3) the stress boundary conditions as defined by the specific problem

is always less than that corresponding to the true stress field."[6] Therefore, the lower-bound to the limit load can be obtained by assuming a stress field which satisfies the above three conditions.

A.3b Upper-Bound Limit Theorem

The upper-bound limit estimates the upper limit of a load required to cause plastic deformation to occur. The upper-bound analysis also incorporates slip-line theory, which gives

an estimate for the movement of the material under plastic deformation. The theorem states that:

"-The actual work done in deforming a rigid-plastic continuum is always less than the work done by an assumed displacement which:

1) satisfies the displacement boundary condition
2) yields a strain field which satisfies the incompressibility condition."[6]

Therefore, the upper-bound to the limit load can be obtained by assuming a displacement field which satisfies the above two conditions and by equating the work done by the external agent with that done deforming the material along the assumed displacement field. The equilibrium condition is totally neglected in obtaining the upper-bound solution.

A.3c Hardness Test Example

Both of the theorems described above are somewhat vague. Therefore, in this section, an example (built upon an example found in Section IV-9 of *Elements of the Mechanical Behavior of Solids*[6]) is shown where both the lower and upper-bound solutions are obtained. Through this example, it is hoped that the reader will gain an understanding of the workings of limit analysis.

Hardness Test Example

A semi-infinite solid is indented by a flat punch, as shown in Figure A.3, in a manner similar to a standard hardness test. The material is assumed to be rigid-plastic (Poisson ration of 0.5 or incompressible) with a shear yield stress κ. We will now determine the upper- and lower-bound indentation loads assuming plane strain conditions and that there is no friction between the indenter and the work piece.

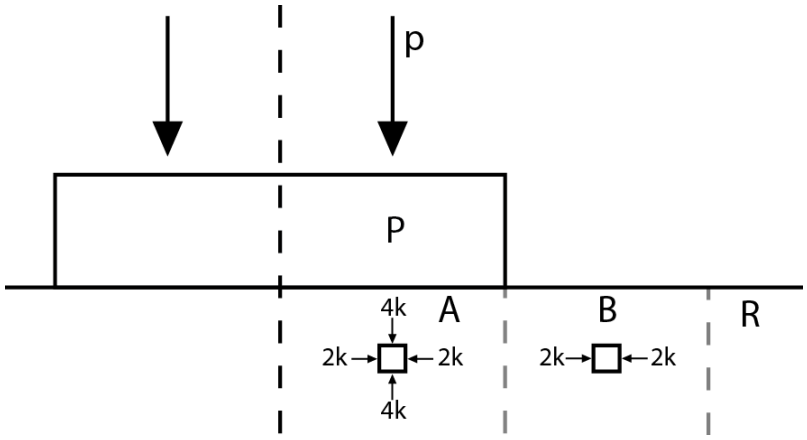

Figure A.3. Lower-bound solution to the stress distribution for the punch-indentation problem where the punch, P, is forced into the material, R, with pressure p. Regions A and B represent the regions where plastic deformation will occur due to the pressure applied to the material through the punch.

A) Lower-Bound Solution

For the punch to be able to indent into the material, the material in region A must yield and be displaced. Due to constraint in the y-direction, the material must be deformed toward region B, thereby requiring the material in region B also to yield and be displaced. Therefore, the state of stress existing in region B must high enough for yielding to occur. For the sake of simplicity we use the Tresca yield criterion which states that $\sigma_1 - \sigma_3 = -\sigma_Y = -2\kappa$ where σ_1 is simply the largest stress in the region, and σ_3 the smallest. (Note that we use the convention of signifying compressive stresses as negative.) In region B, the stress in the vertical direction must be zero to satisfy equilibrium with the air above it. Therefore the horizontal stress may be represented by a compressive stress with a magnitude of $\sigma_{11} = -2\kappa$, which satisfies the Tresca yield condition. In order to satisfy the equilibrium condition in the x-direction, the state of stress in region A must be in equilibrium with the state of stress in region B and also satisfy the yield condition. If this is the case, then the state of stress (as shown in Figure A.3) is $\sigma_{11} = -2\kappa$ and, using the Tresca yield criterion, $\sigma_{22} = -4\kappa$. Therefore, the punch must exert pressure p given by

$$p \geq 4\kappa. \qquad \text{A.7}$$

B) Upper-Bound Solution

For the upper-bound theorem, we assume that the material will shear along the slip-lines shown in Figure A.4 below. The shear stress that needs to be overcome along these slip lines is again the critical shear stress κ. As the punch, P, moves downward, three blocks (A, B, and C) of the work material are displaced. They are always in contact with each other, but are

sliding along the rigid boundaries shown in Figure A.4. Because the blocks are slipping rather than compressing, the assumed displacement field satisfies the condition of incompressibility.

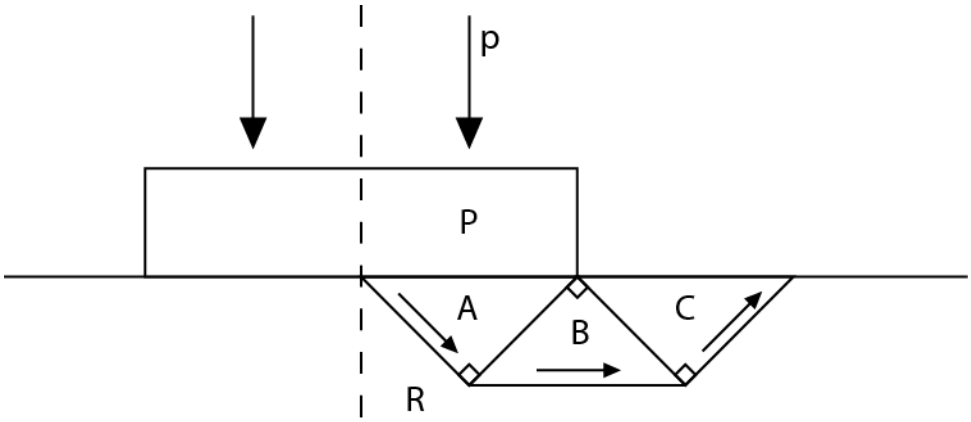

Figure A.4. Displacement field for the upper-bound solution to the punch-indentation problem where the punch, P, is forced into the material, R, with pressure p. Regions A, B, and C represent the constant-volume regions where plastic deformation will occur due to the pressure applied to the material through the punch. The arrows show the direction of movement for each region, and the boundaries represent the slip boundaries.

We now define the relative displacement as q_i, where the subscript denotes the boundary where the slip is occurring. For example, the displacement per unit time for the interface between triangle A and the work material, R is denoted by q_{AR}, the displacement of punch P is denoted by q_P, etc. Furthermore, we can also define the area of the interface as A_i and use the same subscripts as for q_i such that A_{AR} is the area of the interface between triangle A and the work material R. With these definitions, the work done by the punch can be related to the work done in deforming the work material. The work performed by the punch (W_p) is then

$$pq_P a = W_p \qquad \text{A.8}$$

where, because of the symmetry of the system, a is one-half of the cross-sectional area of the punch and p is the pressure applied to the punch. The work done in deforming the material (W_d) is then

$$\kappa(A_{AR}q_{AR} + A_{AB}q_{AB} + A_{BR}q_{BR} + A_{BC}q_{BC} + A_{CR}q_{CR}) = W_d. \qquad \text{A.9}$$

With Equations A.8 and A.9, the pressure, p can be determined. The areas are simply determined from the geometric relations.

The major task now is to determine the relative velocity between the different blocks themselves: between the blocks and the rigid portion R of the work material, and between the blocks and the punch. The velocities, q_i, are shown below in Figure A.5 in the form of a vector diagram commonly known in the field as a hodograph. The velocities must satisfy the requirements of compatibility, and consequently the velocity vectors always form a closed loop.[6] Compatibility requires that rigid blocks adjacent to the rigid region must slide parallel to the slip lines between the blocks and the rigid material. Similarly, the relative velocities between blocks themselves are always parallel to the slip lines between blocks.

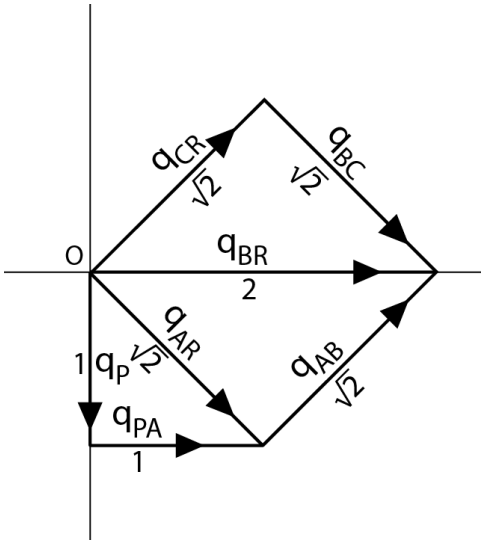

Figure A.5. Hodograph of the displacement field of the punch-indentation problem shown in Figure A.4. Each line represents the vector displacement for each slip boundary normalized to the displacement of the punch.

In the construction of a hodograph, all the absolute velocities are shown to emanate from a single stationary point, point O in Figure A.5, which represents the entire rigid section. Since the punch is moving downward, a vector representing q_P is drawn downward. Recognizing that block A has to move parallel to the slip line between A and R, the absolute velocity of B is drawn from the stationary point O along the direction shown. Similarly, the absolute velocities of blocks B and C are drawn from O. The magnitudes of these velocities are determined by setting the magnitude of q_P arbitrarily to unity. The absolute velocity of block A, q_{AR}, is determined by drawing a horizontal line from the end of the vector q_P until it intersects with q_{AR}, because the relative velocity between the punch and block A has to be horizontal. The magnitude of the absolute velocity q_{BR} is similarly determined by drawing a relative velocity vector q_{AB} parallel to the slip line between blocks A and B.

Substituting these values into Equation A.9 and setting W_d equal to W_p leads to the solution to the upper-bound:

$$p \leq 6\kappa. \quad \text{A.10}$$

Therefore, the true indentation pressure lies between the two limiting values given by Equations A.7 and A.10:

$$4\kappa \leq p \leq 6\kappa. \quad \text{A.11}$$

Indenters used in a standard hardness tests are not flat but are balls, pyramids, or cones. In some tests, including the Rockwell hardness test, the depth rather than the area of indentation is measured. In the Brinell, Vickers, and Knoop hardness tests, the hardness is given in terms of the average load per unit area. While in all of these tests, plane strain conditions do not apply, the indentation loads for the plane strain case are not substantially different, although always less. Experimentally, the indentation hardness in a typical test is found to range from 6.2 to 6.4κ.[1]

A.4 Mathematical Treatment of Strain

In this section we develop the mathematical treatment of strain. The derivation of the equations for strain that follows was taken from Section 2.7 in *Advanced Mechanics of Materials*[7] and from L. Landau and E. Lifshitz.[8]

In continuum mechanics it is useful to describe a change in the shape of a material relative to its initial shape or reference state. This reference state, also called the undeformed state, corresponds to the shape of a stationary material. If a stress is applied to the material it deforms meaning that its shape changes and all the particles within the material move.

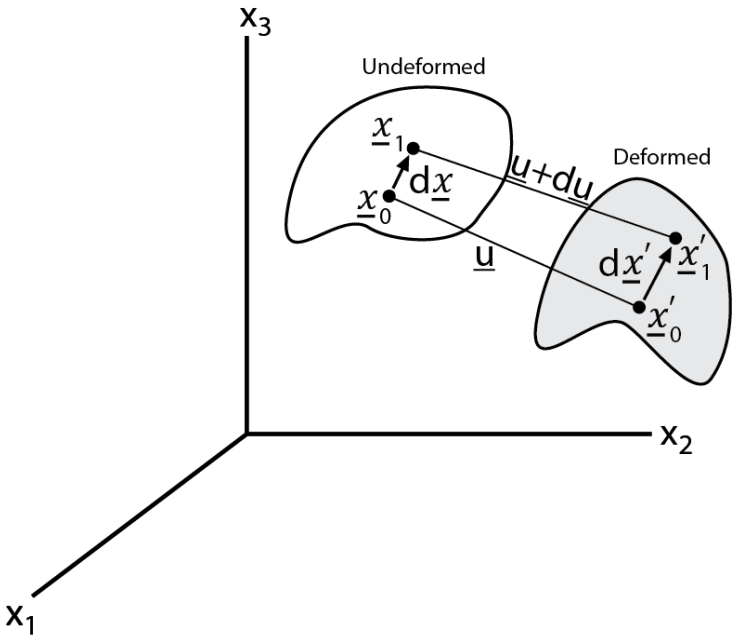

Figure A.6. An undeformed body (white) and the same body after deformation has occurred (grey). $\underline{x}_0$ and $\underline{x}_1$ are two points on the undeformed body where the distance between them is $\mathrm{d}\underline{x}$ and $\underline{x}_0'$ and $\underline{x}_1'$ are the same two points after deformation has occurred with the distance between them being $\mathrm{d}\underline{x}'$. The displacement of point $\underline{x}_0$ due to the deformation is $\underline{\mathrm{u}}$ and the displacement of point $\underline{x}_1$ is $\underline{\mathrm{u}} + \mathrm{d}\underline{\mathrm{u}}$.

Let us first define the position of a particle in the undeformed reference state as $\underline{x}_0$ where $\underline{x}_0(\mathrm{x}_1, \mathrm{x}_2, \mathrm{x}_3)$ (see Figure A.6). If we stress the material, then the particle specified moves to a new position notated as $\underline{x}_0'$ where $\underline{x}_0'(\mathrm{x}_1', \mathrm{x}_2', \mathrm{x}_3')$ (see Figure A.6). The displacement of the point due to the deformation is then given by the vector $\underline{x}_0' - \underline{x}_0$ which we denote as $\underline{\mathrm{u}}$ (the displacement vector)

$$\underline{\mathrm{u}} = \underline{x}_0' - \underline{x}_0. \qquad \text{A.12}$$

When a body is deformed, the distances between its points change. Therefore, let us consider two points very close together, $\underline{x}_0$ and $\underline{x}_1$. The radius vector joining them before deformation is $\mathrm{d}\underline{x}$ and the radius vector joining the same two points after deformation is $\mathrm{d}\underline{x}' = \mathrm{d}\underline{x} + \mathrm{d}\underline{\mathrm{u}}$. The distance between the points is $\mathrm{d}l = \sqrt{\mathrm{dx}_1^2 + \mathrm{dx}_2^2 + \mathrm{dx}_3^2}$ before deformation, and $\mathrm{d}l' = \sqrt{\mathrm{dx}_1'^2 + \mathrm{dx}_2'^2 + \mathrm{dx}_3'^2}$ after deformation. Taking the square of the distances gives us

$$\mathrm{d}l^2 = \mathrm{d}\underline{x} \cdot \mathrm{d}\underline{x} \qquad \text{A.13}$$

and

$$\mathrm{d}l'^2 = \mathrm{d}\underline{x}' \cdot \mathrm{d}\underline{x}'$$

Let us now consider the difference in squared distances between the points in the undeformed and deformed body:

$$\mathrm{d}l'^2 - \mathrm{d}l^2 = \mathrm{d}\underline{x}' \cdot \mathrm{d}\underline{x}' - \mathrm{d}\underline{x} \cdot \mathrm{d}\underline{x}. \qquad \text{A.14}$$

We can employ the chain rule on $\mathrm{d}\underline{x}$ to get

$$\mathrm{d}\underline{x}' = \nabla\underline{x}' \cdot \mathrm{d}\underline{x} \qquad \text{A.15}$$

which, when incorporated into Equation A.14 leads to

$$\begin{aligned} \mathrm{d}\underline{x}' \cdot \mathrm{d}\underline{x}' - \mathrm{d}\underline{x} \cdot \mathrm{d}\underline{x} &= \left(\nabla\underline{x}' \cdot \mathrm{d}\underline{x}\right) \cdot \left(\nabla\underline{x}' \cdot \mathrm{d}\underline{x}\right) - \mathrm{d}\underline{x} \cdot \mathrm{d}\underline{x} \\ &= \mathrm{d}\underline{x}' \cdot \left[\left(\nabla\underline{x}'\right)^{\mathrm{T}} \cdot \nabla\underline{x}' - \underline{\underline{\mathrm{I}}}\right] \cdot \mathrm{d}\underline{x}'. \end{aligned} \qquad \text{A.16}$$

The quantity in the brackets is used to define the Lagrangian description of the strain:

$$\underline{\underline{\mathrm{E}}} = \frac{1}{2}\left[\left(\nabla\underline{x}'\right)^{\mathrm{T}} \cdot \nabla\underline{x}' - \underline{\underline{\mathrm{I}}}\right] \qquad \text{A.17}$$

where the quantity of one-half is arbitrary, and makes the results of this analysis consistent with the well-known linear elastic theory when material displacements are small. If we substitute Equation A.13 into Equation A.17, realizing that $\nabla\underline{x} = \underline{\underline{\mathrm{I}}}$, we get $\underline{\underline{\mathrm{E}}}$ in terms of $\nabla\underline{\mathrm{u}}$, or

$$\begin{aligned} \underline{\underline{\mathrm{E}}} = \frac{1}{2}\left[\left(\nabla\underline{x}'\right)^{\mathrm{T}} \cdot \nabla\underline{x}' - \underline{\underline{\mathrm{I}}}\right] &= \frac{1}{2}\left[\left(\nabla\underline{\mathrm{u}} + \underline{\underline{\mathrm{I}}}\right)^{\mathrm{T}} \cdot \left(\nabla\underline{\mathrm{u}} + \underline{\underline{\mathrm{I}}}\right) - \underline{\underline{\mathrm{I}}}\right] \\ &= \frac{1}{2}\left[\nabla\underline{\mathrm{u}} + \left(\nabla\underline{\mathrm{u}}\right)^{\mathrm{T}} + \nabla\underline{\mathrm{u}} \cdot \left(\nabla\underline{\mathrm{u}}\right)^{\mathrm{T}}\right]. \end{aligned} \qquad \text{A.18}$$

Assuming that $\nabla\underline{\mathrm{u}}$ is small we can drop the higher order term $\nabla_{\mathrm{X}}\underline{\mathrm{u}} \cdot \left(\nabla_{\mathrm{X}}\underline{\mathrm{u}}\right)^{\mathrm{T}}$. Thus, we denote the strain tensor as

$$\underline{\underline{\epsilon}} = \frac{1}{2}\left[\nabla\underline{\mathrm{u}} + \left(\nabla\underline{\mathrm{u}}\right)^{\mathrm{T}}\right]. \qquad \text{A.19}$$

We can also define the deformation-rate tensor $\underline{\underline{\dot{\epsilon}}}$ as simply

$$\underline{\underline{\dot{\epsilon}}} = \frac{1}{2}\left[\nabla \underline{v} + (\nabla \underline{v})^{T}\right]. \qquad \text{A.20}$$

For a more detailed explanation of infinitesimal strain theory, please refer to Sections 2.7 and 2.8 in *Advanced Mechanics of Materials*[7] and Chapter 1 in L. Landau and E. Lifshitz.[8]

A.5 Algebra to get Equation 3.113 from Equation 3.110

From Equation 3.110, we have the relation of the stress to the strain for plastic deformation:

$$\underline{\underline{\dot{\epsilon}}} = \frac{1}{2\eta}\langle 1 - \frac{\kappa}{\sqrt{J_2}}\rangle \underline{\underline{S}}. \qquad \text{3.110}$$

We first assume that we are always in the plastic regime allowing us to remove the brackets. Taking the double dot product of Equation 3.110 yields

$$\underline{\underline{\dot{\epsilon}}} : \underline{\underline{\dot{\epsilon}}} = \left[\frac{1}{2\eta}\left(1 - \frac{\kappa}{\sqrt{J_2}}\right)\right]^2 \underline{\underline{S}} : \underline{\underline{S}}. \qquad \text{A.21}$$

From Equation 3.10, we have $J_2 = 1/2\ (\underline{\underline{S}} : \underline{\underline{S}})$ which gives us

$$\underline{\underline{\dot{\epsilon}}} : \underline{\underline{\dot{\epsilon}}} = 2J_2\left[\frac{1}{2\eta}\left(1 - \frac{\kappa}{\sqrt{J_2}}\right)\right]^2. \qquad \text{A.22}$$

Rearranging Equation A.22 gives us

$$2\eta^2(\underline{\underline{\dot{\epsilon}}} : \underline{\underline{\dot{\epsilon}}}) = J_2\left[\left(\frac{\sqrt{J_2} - \kappa}{\sqrt{J_2}}\right)\right]^2. \qquad \text{A.23}$$

We take the square root of Equation A.23 yielding

$$\eta\sqrt{2(\underline{\underline{\dot{\epsilon}}} : \underline{\underline{\dot{\epsilon}}})} = \sqrt{J_2} - \kappa. \qquad \text{A.24}$$